QUANTITATIVE MAPPING OF LUNG VENTILATION USING HYPERPOLARIZED GAS MAGNETIC RESONANCE IMAGING

KIARASH EMAMI

A Dissertation in

ELECTRICAL AND SYSTEMS ENGINEERING

Presented to the Faculties of the University of Pennsylvania

in Partial Fulfillment of the Requirements for the Degree of Doctor of Philosophy

2011

_____

Dissertation Supervisor
Rahim R. Rizi, Ph.D.
Associate Professor of Radiology

_____

Graduate Group Chairperson
Roch Guerin, Ph.D.
Alfred Fitler Moore Professor of Telecommunication Networks

Dissertation Committee:

Dwight L. Jaggard, Ph.D.
Professor of Electrical and Systems Engineering

Saleem A. Kassam, Ph.D.
Solomon and Sylvia Charp Professor of Electrical Engineering

Mitchell Schnall, M.D., Ph.D.
Matthew J. Wilson Professor of Radiology & Vice Chair for Research

Masaru Ishii, M.D., Ph.D.
Associate Professor of Otolaryngology–Head & Neck Surgery

Quantitative Mapping of Lung Ventilation Using

Hyperpolarized Gas Magnetic Resonance Imaging

Dedicated to my wife

Sharareh R. Nejad

ACKNOWLEDGEMENT

First and foremost, I would like to acknowledge the supervision and support of my advisor and mentor, Dr. Rahim Rizi, who through his continued guidance and encouragement made it possible for me to realize the goals of this research project. He is a constant source of enthusiasm and ambition and without him sharing his wisdom and vision in the area of biomedical imaging, this work would not have been materialized.

I would like to express my deepest gratitude to my wife, Sharareh Nejad. Without her love, support and sacrifice, my endeavors would have been in vain. My gratitude also goes to my parents for their support and kindness through the years, respecting my opinion as a mature member of the family – no matter how young and immature I was, and for providing me with the means to pursue my interests, no matter how unrelated and diverse they may have been.

I am really grateful to all of my colleagues in Functional and Metabolic Imaging Group. But most importantly I am in debt to Dr. Stephen Kadlecek for his unmatched intelligence and willingness to share his knowledge and experience on hyperpolarized gas physics, and everything else. Assistance and participation of gentlemen Yinan Xu, Hooman Hamedani, and Yi Xin cannot go unmentioned, as they were essential in enabling ideas to actions. I would like to also acknowledge the efforts of Ms. Harmony Li in diligent proofreading of the dissertation manuscript.

I would like to thank my thesis committee for their valued time and feedback, especially Dr. Masaru Ishii for his engaging and detailed discussions on the subject matter.

Lastly I would like to sincerely acknowledge the support from National Institutes of Health and their irreplaceable role in the ever-expanding boundaries of biomedical sciences.

ABSTRACT

QUANTITATIVE MAPPING OF LUNG VENTILATION USING HYPERPOLARIZED GAS MAGNETIC RESONANCE IMAGING

Kiarash Emami

Rahim R. Rizi

The main objective of this project was to develop and implement techniques for high-resolution quantitative imaging of ventilation in lungs using hyperpolarized gas magnetic resonance imaging (MRI). Pulmonary ventilation is an important aspect of lung function and is frequently compromised through several different mechanisms and at varying degrees in presence of certain lung conditions, such as chronic obstructive pulmonary diseases. The primary focus of this development is on large mammalian species as a steppingstone towards translation to human subjects. The key deliverables of this project are a device for real-time mixing and delivery of hyperpolarized gases such as ^{3}He and ^{129}Xe in combination with O_2, an MRI acquisition scheme for practical imaging of ventilation signal build-up in the lungs, and a robust mathematical model for estimation of regional fractional ventilation values at a high resolution.

A theoretical framework for fractional gas replacement in the lungs is presented to describe MRI signal dynamics during continuous breathing of a mixture of hyperpolarized gases in presence of several depolarization mechanisms. A hybrid

ventilation and imaging acquisition scheme is proposed to acquire a series of images during short end-inspiratory breath-holds over several breaths. The sensitivity of the estimation algorithm is assessed with respect to noise, model uncertainty and acquisition parameters, and subsequently an optimal set of acquisition parameters is proposed to minimize the fractional ventilation estimation error. This framework is then augmented by an undersampled parallel MRI scheme to accelerate image acquisition to enable fractional ventilation imaging over the entire lung volume in a single pass. The image undersampling was also leveraged to minimize the coupling associated with signal buildup in the airways and the irreversible effect of RF pulses. The proposed technique was successfully implemented in pigs under mechanical ventilation, and preliminary measurements were performed in an adult human subject under voluntary breathing.

TABLE OF CONTENTS

LIST OF TABLES

LIST OF FIGURES

CHAPTER 1: Introduction

1.1. Background and significance

As the core component of the respiratory system in vertebrate animals and humans, the lungs deliver oxygen to depleted venous blood and remove excess carbon dioxide from this blood pool such that a reasonably stable oxygen level is maintained in key organs and extremities. The O_2–CO_2 gas exchange takes place across the alveolar membrane between the gas and blood phases. Efficient delivery of O_2 and removal of CO_2 to and from alveolar airspace, a process known as *pulmonary ventilation*, however is an essential prerequisite to successful gas exchange.

Many obstructive lung diseases, including emphysema, asthma, and cystic fibrosis, impair gas replacement in the lung parenchyma. Asthma, for instance, is characterized by narrowed airways, emphysema causes tissue destruction and an elevated elasticity accompanied by air trapping, whereas fibrosis leads to a hardened, less compliant lung tissue. Even though the mechanism of each disease and the effect on lung tissue are different, they all manifest themselves in compromised gas replacement efficiency and, subsequently, impaired pulmonary ventilation. Additionally, most disease-induced changes in lungs are typically heterogeneous, resulting in non-uniform changes in lung ventilation. Early diagnosis and monitoring the progression of ventilation abnormalities

in the lungs therefore necessitate a non-invasive and quantitative technique sensitive to these localized changes.

Traditional pulmonary function tests (PFT), such as forced expiratory volume in one second (FEV_1), are currently the gold standard for non-invasive assessment of human pulmonary system that provide an inexpensive but insensitive global measure of lung function. The most common clinical ventilation imaging technique available today is radionuclide scintigraphy. Although noninvasive and widely available, these techniques suffer from poor spatial resolution and exposure to radioactive materials. X-ray radiography techniques, most notably high resolution computed tomography (CT), are fundamentally structural imaging modalities capable of providing high fidelity images of lung tissue density. Radio-dense tracer gases (e.g. xenon) have been used for measurement of lung ventilation with CT. This technique, however, requires repeated measurements to yield a plausible signal-to-noise ratio (SNR), resulting in repeated exposure to ionizing radiation.

Hyperpolarized gas magnetic resonance imaging (HP gas MRI), and specifically HP ^{3}He MRI, is an attractive imaging modality for regional assessment of lung function with promising temporal and spatial resolution and an attractive safety profile. This imaging method has opened the possibility for noninvasive visualization of gas atoms in ventilated lung airspaces and has recently been used for investigational assessment of asthma, emphysema, and cystic fibrosis. Despite the significance of quantitative imaging of ventilation and gas replacement, this technique remains as one of the lesser developed

areas of HP gas MRI methodology. This is partly due to the complex gas transport mechanisms in the lungs, and the associated challenges with quantitative interpretation of images of respiratory gas flow through airways. The lung is a deformable object with a complex geometry and a moving boundary in all three dimensions, which makes localized tracking of its regions a difficult task. Additionally the polarization of HP gas decays quickly and irreversibly upon entering the lungs, with a typical *in vivo* decay time constant on the order of 10–20 seconds. This decay is driven by several factors including, primarily, the regional interaction with O_2 molecules as well as the applied radio frequency (RF) pulses, intermolecular collisions, wall relaxation and diffusion effects. Quantitative interpretation of signal dynamics therefore can be irrecoverably affected by the time history of coupled decay mechanisms.

So far, single-breath HP gas static spin density images have been commonly used for qualitative evaluation of gross ventilation defects. More recently dynamic imaging techniques have been developed for and implemented in fast imaging of respiratory gas flow and air trapping in affected patients. True quantitative imaging of pulmonary ventilation, however, still remains an unaddressed area in pulmonary imaging. A robust and objective measure of respiratory gas replacement and distribution is an essential step towards enabling this technology to become a reliable diagnostic and monitoring tool across the affected and at risk individuals. The only successful attempt in quantitative imaging of lung ventilation was reported by Deninger *et al.*, albeit with restrictions that made it only feasible in small species, e.g. rodents.

1.2. Objective and specific aims

The primary goal of this thesis research project is to develop and implement techniques for high resolution and reliable imaging of fractional ventilation in lungs of large species using HP gas MRI as a steppingstone for translation to human use. The key deliverables of this project are: 1) a device for real-time mixing and delivery of hyperpolarized gas and oxygen to large species including human subjects, 2) an MRI acquisition scheme for reliable acquisition of ventilation signal build-up in the lungs, and 3) a mathematical model for robust estimation of fractional ventilation on a regional basis. These goals were pursued through systemically conducting the following aims:

Aim 1. To develop the ventilation imaging technique and signal dynamics model

1.1. Develop a refined fractional ventilation imaging technique to address shortcomings of prior methods with utility in humans;

1.2. Develop a multi-compartment mathematical model of gas replacement in lungs governing the fractional ventilation, dead spaces, and HP gas signal dynamics in presence of RF-induced and O_2-inducded decay mechanisms;

1.3. Perform regional measurements of gas arrival time constant by incorporating the gas mixing transitions in the signal dynamics model;

1.4. Analyze the sensitivity of fractional ventilation estimation model to noise in images, image acquisition parameters, uncertainty in model parameters and gas mixing dynamics;

1.5. Optimize the fractional ventilation imaging and estimation technique for efficient use of the finite HP ^{3}He signal and image acquisition time.

Aim 2. To implement and validate the ventilation imaging technique in small animals and phantoms

2.1. Design and prototype a programmable HP gas delivery and mixing system for synchronized MRI of animal lungs;

2.2. Validate the fractional ventilation imaging and estimation technique in a simple lung phantom;

2.3. Assess the *in vivo* repeatability and measurement uncertainty of fractional ventilation in small animals.

Aim 3. To implement and optimize the whole lung ventilation imaging technique in large animals and humans

3.1. Implement the fractional ventilation imaging technique in large animals synchronized with the programmable HP gas delivery and mixing device;

3.2. Utilize and optimize an accelerated imaging scheme for whole-lung imaging of fractional ventilation in one pass;

3.3. Design and prototype a passive human gas mixing and delivery device with real-time flow measurement capability;

3.4. Implement the whole lung fractional ventilation imaging and estimation technique in human subjects.

1.3. Thesis organization

The remainder of this dissertation is organized as follows:

Chapter 2 provides a brief overview of obstructive lung diseases that compromise pulmonary ventilation and current clinical and imaging techniques available for diagnosis and assessment of lung ventilation. It then provides an overview of the essential components of 2D Cartesian magnetic resonance imaging and closes with a brief description of optical pumping hyperpolarization of noble gases for pulmonary MRI applications.

Chapter 3 provides the theoretical foundations for fractional gas replacement in the lungs along with the magnetization buildup in the airways when breathing HP gases. MR signal buildup dynamics in the airways are derived for the proposed *serial* ventilation sequence using a point object model, in comparison to the *cascade* ventilation sequence developed earlier, and in presence of RF- and oxygen-induced depolarization mechanisms. It then moves on to introducing a three-compartment dead space model in signal buildup equations in order to improve ventilation estimation accuracy. The chapter closes by incorporating a respiratory gas arrival and mixing time constant to elucidate fractional ventilation dynamics during the course of a breath.

Chapter 4 deals with the sensitivity analysis of the ventilation estimation model with respect to various model parameters and noise as well as the number of acquired images

and RF pulses per measurement. This information is then utilized to specify the optimal acquisition parameters in order to maximize the dynamic response and to minimize the measurement uncertainty.

Chapter 5 presents the experimental methodologies and results of technique implementation and assessment in phantoms and small animals (i.e. rats) using an automated gas mixing and delivery device. The serial ventilation imaging technique is then validated in a simple artificial lung model. Reproducibility and tidal volume dependency of ventilation measurements, as well as the estimates of regional ventilation time constant, are demonstrated in rats. The chapter then closes by comparing the results acquired by the two ventilation imaging techniques in rats and their properties.

Chapter 6 describes the methodology and results for implementation of serial ventilation imaging technique in large animals (i.e. pigs). After describing the challenges associated with migrating the serial ventilation imaging technique to large species, it presents the theory and practice of accelerated image acquisition using parallel MRI, and the benefits it presents for enabling ventilation measurements over the entire lungs of large species including humans. Optimality conditions for accelerated ventilation imaging are discussed and finally preliminary results in performing ventilation measurements in healthy human subjects are presented.

Finally, Chapter 7 summarizes key results of this project, outlines the challenges that lie ahead towards standardized measurement in human subjects, and a number of ideas to pursue immediately towards achieving this goal.

CHAPTER 2: Overview of Hyperpolarized Gas Pulmonary MRI

2.1. Introduction

Lung ventilation is the rate at which gas enters or leaves the lungs. More specifically, alveolar ventilation is the volume of gas per unit time that reaches the alveoli (air sacs) – the respiratory portions of the lungs where gas exchange occurs. The function of ventilation is to transport the air between the lungs and the atmosphere so that oxygen can be exchanged for carbon dioxide in the alveoli.

Obstructive lung diseases such as emphysema, asthma, and cystic fibrosis adversely affect gas flow in the lungs, and therefore compromise regional lung ventilation at different levels and times. High-resolution, localized and quantitative imaging of lung ventilation can therefore serve as a valuable tool for diagnosis and management of lung diseases in many different ways. Obtaining regional measurements of lung ventilation defects is a more effective method for evaluating the location and extent of diseases and their distribution in the lungs. Further, it can assist physicians in providing more targeted and personalized therapeutic treatments.

Non-invasive and high-resolution measurements of ventilation can be more sensitive to smaller and localized changes in lung ventilation (compared to other diagnosis methods discussed in the following sections) and can therefore serve as a more accurate marker of

early disease formation. Early detection of lung diseases can in turn trigger a more timely intervention and improve the chances of patient recovery as well as reduce the cost and duration of therapy. On an individual and social scale, this technique could enhance the quality of life and reduce disability-associated overhead imposed upon the general public. Moreover, non-invasive and safe imaging-based methods for evaluating lung function have the potential to become routine screening tools that can identify populations at risk of developing lung diseases.

Finally, a non-invasive and sensitive tool for regional assessment of lung ventilation allows for longitudinal monitoring of disease progression and response to therapy in affected populations. Essentially, it can serve as a valuable tool for developing and evaluating the efficacy of new therapies. Quantitative assessment of diseases, especially through non-invasive imaging methods, also aligns with the overall goal of modern medical diagnosis, which is moving towards a more objective and personalized assessment and treatment of diseases.

2.2. Obstructive lung diseases

2.2.1. Chronic obstructive pulmonary disease

Chronic obstructive pulmonary disease (COPD) is a group of progressive diseases of the lung, including chronic bronchitis and emphysema, characterized by airway obstruction and inflammation. Despite being largely preventable, COPD is a major cause of disability. It is the fourth leading cause of death in the United States and is now the most common form of chronic lung disease. More than 12 million people are currently

diagnosed with COPD. Chronic bronchitis is a condition in which repeated irritation of the airways leads to chronic inflammation and excess mucous production. While bronchitis affects the airways, emphysema is a condition characterized by destruction of the alveolar walls, as shown in Figure 2.1(a). It eventually results in difficulty breathing as surface area for gas exchange decreases and lung elasticity lessens. COPD affects millions of people worldwide and is prevalent among smokers and persons chronically exposed to high levels of dust and toxic chemicals (among other environmental factors).

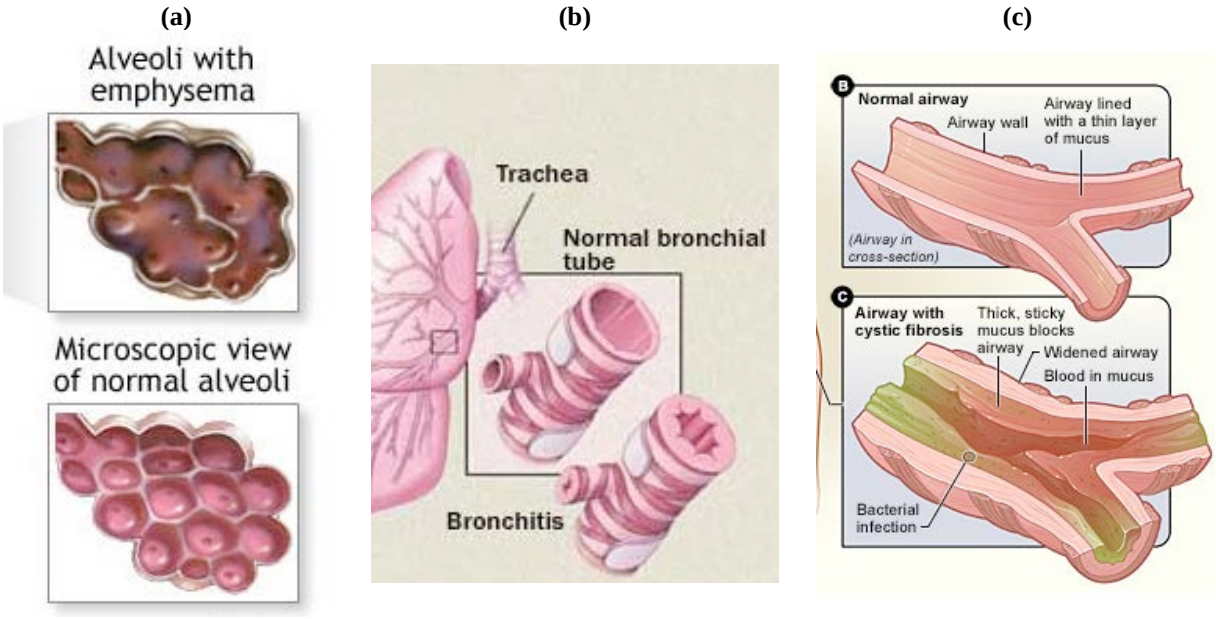

Figure 2.1. Alteration in small airways and alveoli in three primary obstructive pulmonary diseases (courtesy of National Institutes of Health)

2.2.2. Asthma

Asthma is a condition characterized by episodic constriction and inflammation of the airways, as shown in Figure 2.1(b), resulting in reduced lung function, coughing, wheezing and shortness of breath. The disease is estimated to affect 300 million people worldwide and to account for roughly 1 out of every 250 deaths worldwide. The onset of

asthma symptoms is caused by a variety of stimuli including exercise, allergens, or viral infection. Furthermore, asthma is now believed to have a non-reversible degenerative component caused by airway remodeling.

2.2.3. Cystic fibrosis

Cystic fibrosis (CF) is a congenital disease of the exocrine system affecting about 40,000 people in the US. The disease causes a defect in a protein responsible for chloride removal in mucous secretions of the exocrine glands. As a result, the mucous is more viscous than normal and thus is not readily cleared from lung airways by ciliary action, as shown in Figure 2.1(c). This thick mucous can lead to problems such as increased infection, particularly in the lungs, and impairment of digestion. Although the mucous can build up and impair respiratory function, in fact, chronic infection and associated chronic bronchitis is thought to be the most damaging component of the disease.

2.3. Pulmonary function testing

Currently the most common method of measuring lung function is *spirometry*, a technique in which the subject breaths through a tube attached to a pneumotachometer, a device capable of measuring airflow (Figure 2.2). A complete pulmonary function test (PFT) usually involves the use of spirometry before and after the administration of a bronchodilator, measurements of lung volumes, and measurement of diffusion capacity. Two spirometric measurements commonly used to evaluate lung function are the forced vital capacity (FVC) and the forced expiratory volume in one second (FEV_1). FVC is the total volume the patient is able to exhale after full inspiration and FEV_1 is the volume of

air the patient can forcibly exhale in one second. Often, the ratio FEV_1/FVC is used as an indicator of total lung function. While these measurements have been correlated with disease, they can only provide information about the lung as a whole, and not its specific regions. Nevertheless, due to their common utility and significant role in today's clinical practice, key PFT parameters and maneuvers are reviewed in this section.

Figure 2.2. A generic human PFT device.

2.3.1. Static lung volumes and capacities

Static lung volumes reflect the elastic properties of the lungs and the chest wall. Figure 2.3 shows an overview of all the key lung volume quantities. Vital capacity (VC) is the maximum volume of air that can be expired slowly after a full inspiratory effort. Simple to evaluate, it is one of the most valuable measurements of pulmonary function. Since VC decreases as a restrictive lung disorder (e.g., pulmonary edema, interstitial fibrosis) progresses, the course of such a disorder and its response to therapy can be monitored by tracking VC and diffusive capacity.

Forced vital capacity (FVC), similar to VC, is the volume of air expired with maximal force. It is usually measured along with expiratory flow rates using simple spirometry (see below, Dynamic Lung Volumes and Flow Rates). The VC can be considerably greater than the FVC in patients with airway obstruction. During the FVC maneuver, terminal airways affected by the disease close prematurely (i.e., before the true residual volume is reached), trapping gas, and hence affecting the measurement by spirometer.

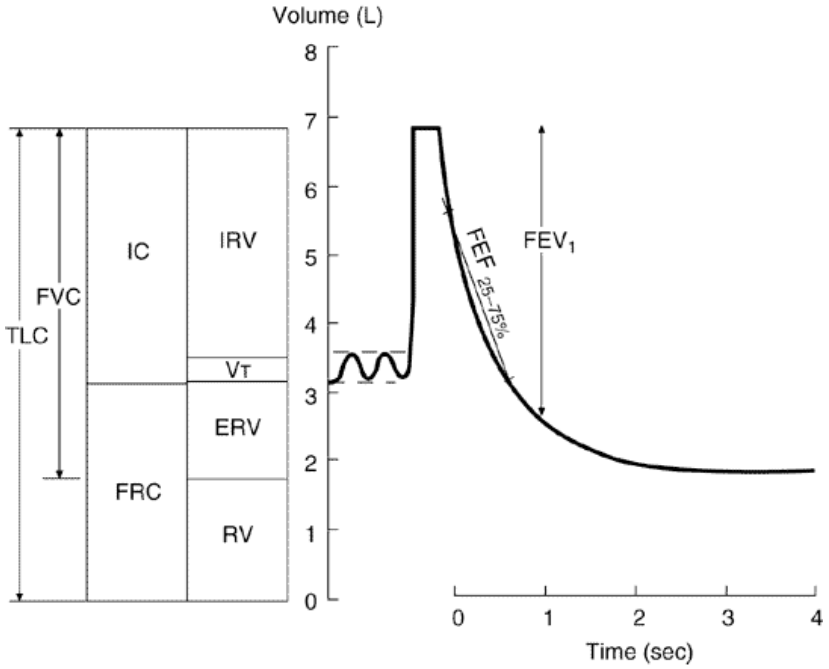

Figure 2.3. Lung volumes, capacities and flow rates.

Total lung capacity (TLC) is the total volume of air within the chest after a maximum inspiration. Functional residual capacity (FRC) is the volume of air in the lungs at the end of a normal expiration when all respiratory muscles are relaxed. Physiologically, FRC is the most important lung volume because it corresponds to the exhalation volume for normal tidal breathing range. Outward elastic recoil forces of the chest wall tend to increase lung volume but are balanced by the inward elastic recoil of the lungs, which tends to reduce it; these forces are normally equal and opposite at about 40% of TLC.

Loss of lung elastic recoil in emphysema increases FRC. On the other hand, the increased lung stiffness in pulmonary edema, interstitial fibrosis, and other restrictive disorders decreases FRC. The inspiratory capacity (IC) is the difference between TLC and FRC.

The FRC has two components: residual volume (RV), the volume of air remaining in the lungs at the end of a maximal expiration, and expiratory reserve volume (ERV); ERV= FRC – RV. The RV normally accounts for about 25% of TLC. Changes in RV are correlated to those in FRC with several exceptions. First, in restrictive lung and chest wall disorders, RV decreases less than FRC and TLC. Second, in small airways disease, premature closure during expiration leads to air trapping, so that the RV is elevated while the FRC remains close to normal. Third, in COPD and asthma, RV increases more than TLC, resulting in some decrease in VC.

Dynamic Lung Volumes and Flow Rates reflect the caliber and integrity of the airways. Spirometry records lung volume versus time during an FVC maneuver. Forced expiratory volume in 1 sec (FEV_1) is the volume of air forcefully expired during the first second after a full breath and normally accounts for more than 75% of the FVC. This value is recorded both as an absolute value and relative to FVC (FEV_1/FVC). The mean forced expiratory flow during the middle half of the FVC ($FEF_{25–75\%}$) is the slope of the line that intersects the spirographic tracing at 25% and 75% of the FVC. The $FEF_{25-75\%}$ is less effort-dependent than the FEV_1 and is a more sensitive indicator of early airway obstruction.

2.3.2. Diffusing capacity

The diffusing capacity for carbon monoxide (DL_{CO}) can be determined from a single breath. The patient inspires a known small amount of carbon monoxide (CO), holds his breath for 10 sec, and then exhales. A sample of alveolar (end-expiratory) gas is analyzed for CO, and the amount absorbed during that breath is then calculated and recorded in mL/min/mm Hg.

A low DL_{CO} more likely reflects abnormal ventilation-to-perfusion ratios ($\dot{V}/\dot{Q}$) in diseased lungs rather than physical thickening of the alveolar-capillary membrane. However, this test relies on the availability of hemoglobin (Hb) for CO and thus is affected by the volume of blood and the quantity of de-saturated Hb in the lungs at the time of testing. The DL_{CO} is low in processes that destroy alveolar-capillary membranes (e.g., emphysema and interstitial inflammatory or fibrotic processes) and in severe anemia, in which less Hb is available to bind the inhaled CO. The DL_{CO} is artificially low if the patient's Hb is already occupied by CO (e.g., if the subject smokes within several minutes of the test).

2.3.3. Small airways studies

In a normal lung, bronchi less than 2 mm in diameter constitute about 10% of the total airway resistance, but their total surface area is large. Diseases affecting primarily the small (peripheral) airways can be extensive, and yet not reflect on airway resistance or any tests dependent on it (e.g., FEV_1). This is true of early obstructive lung disease and interstitial granulomatous, fibrotic, or inflammatory disorders. The status of the small

airways is reflected by the $FEF_{25-75\%}$ and by expiratory flow rates in the last 25–50% of the FVC.

Figure 2.4. A typical chest X-ray radiograph (courtesy of Imperial College, London UK).

2.4. Lung imaging techniques

Lung assessment has been historically performed using chest X-ray radiography since the mid-20^{th} century, which apart from only providing a purely anatomical and gross view of the lungs, is notoriously insensitive to small and localized changes in lungs induced by pulmonary diseases (Figure 2.4). The oldest technique for direct imaging of lung ventilation is based on radionuclide scintigraphy and radioactive elements such as ^{133}Xe, $^{13}N_2$, $^{15}O_2$ and more commonly ^{99m}Tc-DTPA. Although noninvasive and widely available, these techniques suffer from poor spatial resolution and expose the subject to radioactive materials. Despite developments in detector technology, such imaging is rarely performed today. Chest X-ray imaging remains by far the most cost-effective non-invasive way to image the lungs, and is the most popular method in clinical practice. Although many pathological processes in X-ray radiographs can be detected by trained eye, it is a purely qualitative 2D projection image, and incapable of resolving airways and

respiratory gas. More recently, PET, CT, and MRI have been used in clinical research for non-invasive quantitative imaging of the lungs. As discussed below, these methods have different strengths and weaknesses and yield complementary information on pulmonary function and anatomy.

2.4.1. X-ray computed tomography

X-ray Computer Tomography (CT) was demonstrated clinically in 1973 and rapidly adopted into clinical use by 1980. The technology combined the knowledge of X-ray penetration and interaction with living tissue and multi-projection image reconstruction techniques to produce true two-dimensional anatomical images, rather than simple projection radiographs. Modern instruments utilize the same core principles, but greater detector sensitivity and computing power have led to faster imaging at a fraction of the radiation dosage. Single-slice acquisition is restricted to the axial plane, but multi-slice and spiral CT techniques have extended the imaging plane along the orthogonal axis so that sagittal, coronal, and oblique slices can be captured.

CT has two major advantages over other 3D imaging tools: speed and resolution. Current systems employ multiple-detector arrays that offer as many as 64 slices per projection rotation, which can be completed in less than one second. Clinical systems now offer sub-millimeter resolution, making CT by far the best tool for most anatomical imaging applications. The use of high-resolution CT (HRCT) has proven especially effective in diagnosing diffuse lung diseases, bronchiectasis, and small airway diseases such as obliterative bronchiolitis.

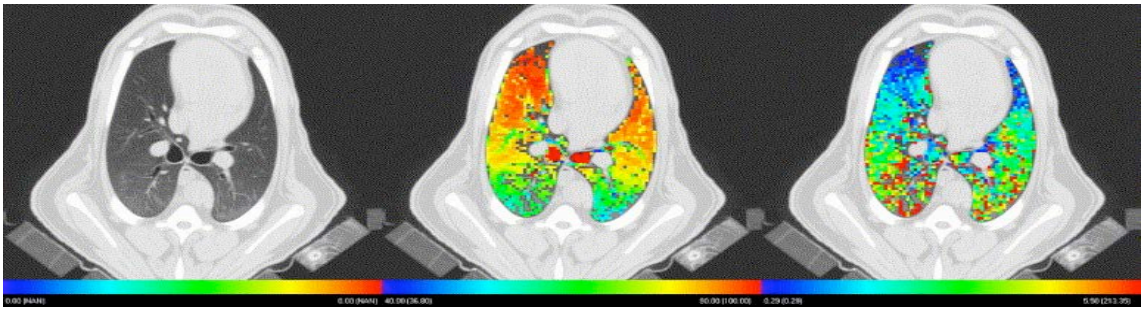

Figure 2.5. Regional Xe-CT analysis (ROI size, 8 × 8 pixels) for a slice of sheep lungs at the level of the carina, showing **(left)** original gray-scale image and color maps of **(middle)** regional air content (% air) and **(right)** specific ventilation (sec^{-1}) [1].

CT has been used to quantitatively measure changes in lung tissue density, but it has largely been used in anatomical imaging. Perfusion studies have been performed with radio-opaque contrast agents, but limited only to studies of embolism or lung nodules. Pulmonary ventilation has been measured from CT images using certain contrast agents, most commonly the radiodense tracer gas xenon. CT techniques provide high spatial resolution and a high degree of anatomic localization of the change of regional lung gas replacement during the wash-in and subsequent wash-out of xenon gas, as shown in Figure 2.5. However, this technique requires repeated measurements, and therefore repeated exposure to ionizing radiation. Additionally, xenon has anesthetic and sedative properties, which limit the concentration, the achievable contrast enhancement, and consequently, the signal-to-noise ratio (SNR). Use of this technology in humans has therefore been limited due to safety issues caused by the ionizing radiation. As a result, these tests cannot be repeated frequently enough for both disease management and the assessment of therapeutic interventions.

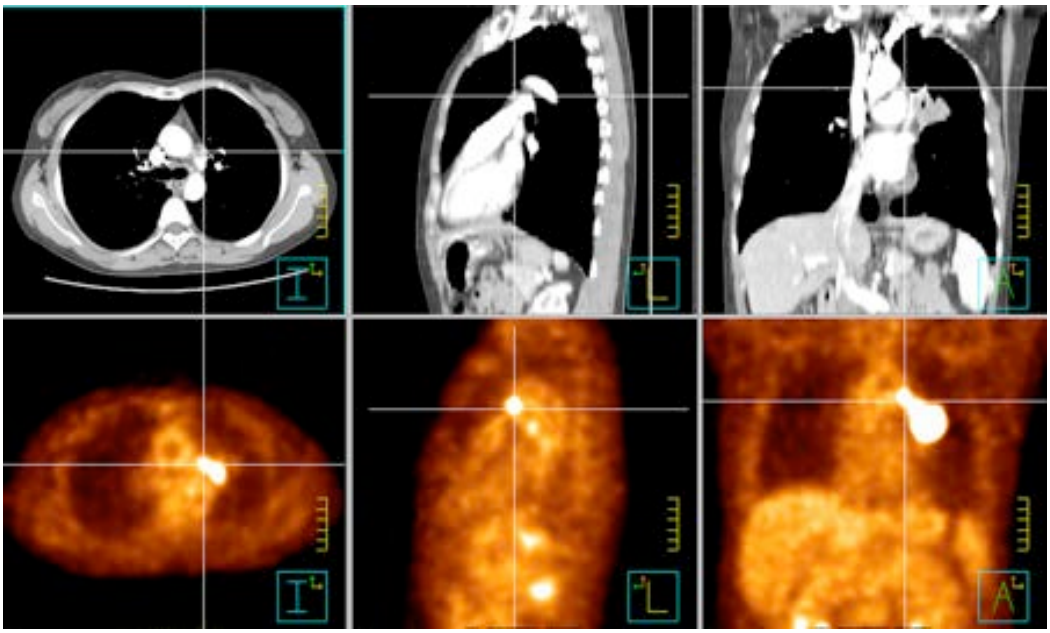

Figure 2.6. Co-registered set of anatomical and metabolic lung images in three primary planes acquired using a hybrid PET-CT scanner. The bright spot in the PET image (bottom row) correspond to a cancerous tumor with high metabolic activity (courtesy of Cedars-Sinai Medical Center, Los Angeles, CA).

2.4.2. Radionuclide imaging

Positron emission tomography (PET) was developed in 1972 and first used clinically in 1975. While CT uses an external X-ray source as the probe, PET utilizes positron-emitting radiotracers that can be incorporated into metabolically-active agents. Positron annihilation produces pairs of photons that are emitted in opposite directions; detectors isolate only these photon pairs, allowing truly quantitative localization of the radiation sources, although resolution is limited to the centimeter scale. Modern PET systems now have integrated CT units so that quantitative data from the former can be co-registered with detailed anatomy offered by the latter, as shown in Figure 2.6.

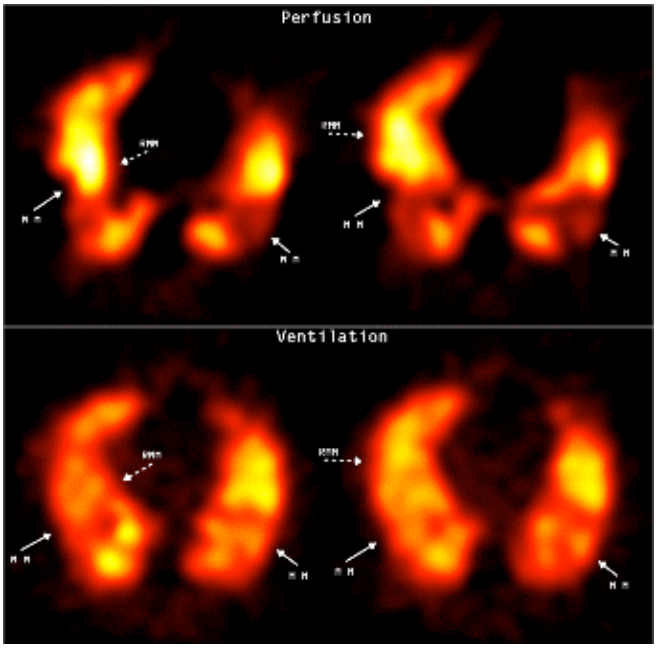

Figure 2.7. Maps of perfusion and ventilation acquired with SPECT showing embolic disease from extensive associated pulmonary disease. "MM" indicates mismatching defects, and "RMM" indicates reverse mismatching defects. Ventilation images are acquired 1.5 hours after perfusion images using ^{99m}Tc DTPA aerosol. Areas of absent perfusion in both lower lobes are well ventilated, constituting mismatching defects. Areas of reverse $\dot{V}_A/\dot{Q}$ indicate venous admixture (courtesy of Saint Agnes Medical Center, Fresno, CA and University of California, San Francisco, CA).

Single-photon emission computed tomography (SPECT), on the other hand uses gamma rays to directly detect gamma-emitting radioisotope contrast agents, administered through injection into blood stream or inhaled in aerosolized form. Both PET and SPECT have the ability to obtain quantitative pulmonary perfusion and ventilation images using a wide array of radioisotope tracers. Figure 2.7 shows an example of ventilation and perfusion maps obtained after administration of Technetium-99m diethylenetriamine penta-acetate (^{99m}Tc-DTPA) depicting ventilation-perfusion mismatch in lung with pulmonary embolism. Quantitative $\dot{V}_A/\dot{Q}$ maps from PET and SPECT have been shown to accurately predict global gas measurements acquired using the multiple inert gas elimination technique (MIGET), the gold standard for measuring pulmonary $\dot{V}_A/\dot{Q}$ distribution [2]. No other imaging modality has been able to show such an agreement in

$\dot{V}_A/\dot{Q}$ data, thereby certifying PET as the current gold standard in regional $\dot{V}_A/\dot{Q}$ *in vivo* mapping of the lung.

Figure 2.8. A representative ^{1}H MR image of lungs and surrounding tissue (courtesy of National Aeronautics and Space Administration)

2.4.3. Conventional MRI

Water proton magnetic resonance imaging (^{1}H MRI) has provided the medical and scientific community with a powerful technique to non-invasively visualize and contrast soft tissue structures *in vivo*. Although the first MR image was demonstrated in 1973, the principles of magnetic resonance were demonstrated experimentally by Bloch and Purcell in 1946 [20,21]. This early technique was rapidly adopted by chemists and named nuclear magnetic resonance (NMR). Imaging was made possible by Lauterbur and Mansfield, who used magnetic field gradients to obtain spatial information [22, 23], described in further detail in the following sections.

MRI has two distinct advantages over PET and CT: it uses no ionizing radiation and provides greatly improved soft-tissue contrast. One major drawback, however, is its relatively poor SNR. In order to boost MR signals, ^{1}H MRI requires very large magnetic fields and relies on the high water-density of the region of interest. The latter restriction has largely prevented MRI from being a popular diagnostic tool in lung imaging because lung tissue is comprised mainly of gas space (Figure 2.8). Lung MRI is made more difficult by local magnetic field gradients across tissue-air boundaries, known as magnetic susceptibility-induced background gradients, which degrade SNR even further. Lastly, like CT, ^{1}H MRI samples from the lung tissue only, not from the gas spaces.

Despite these difficulties, functional lung studies with ^{1}H MRI have been performed using molecular oxygen as a contrast-enhancing agent [24–26]. The ^{1}H source comes from the lung tissue but is affected by the presence of oxygen, which is a paramagnetic substance. The oxygen diffuses readily into lung tissue and shortens the T_1 relaxation properties of the nearby ^{1}H spins, a quantifiable process. The alveolar partial pressure, P_AO_2, can be indirectly calculated from such measurements. This technique, however, does not directly sample from the gas space in the alveoli, and requires accurate respiratory gating and image co-registration techniques.

MR angiography (MRA) is used to acquire images of vasculature and has been adapted for use in visualizing pulmonary vessel disorders [27]. Contrast-enhanced MRA, or cMRA, employs blood-pool agents such as gadolinium-GTPA to highlight MR signals from blood only. This has been exploited to provide qualitative measurements of

pulmonary perfusion [28, 29]. However, quantitative information is difficult to obtain because a highly non-linear relationship exists between contrast agent concentration and MR signal.

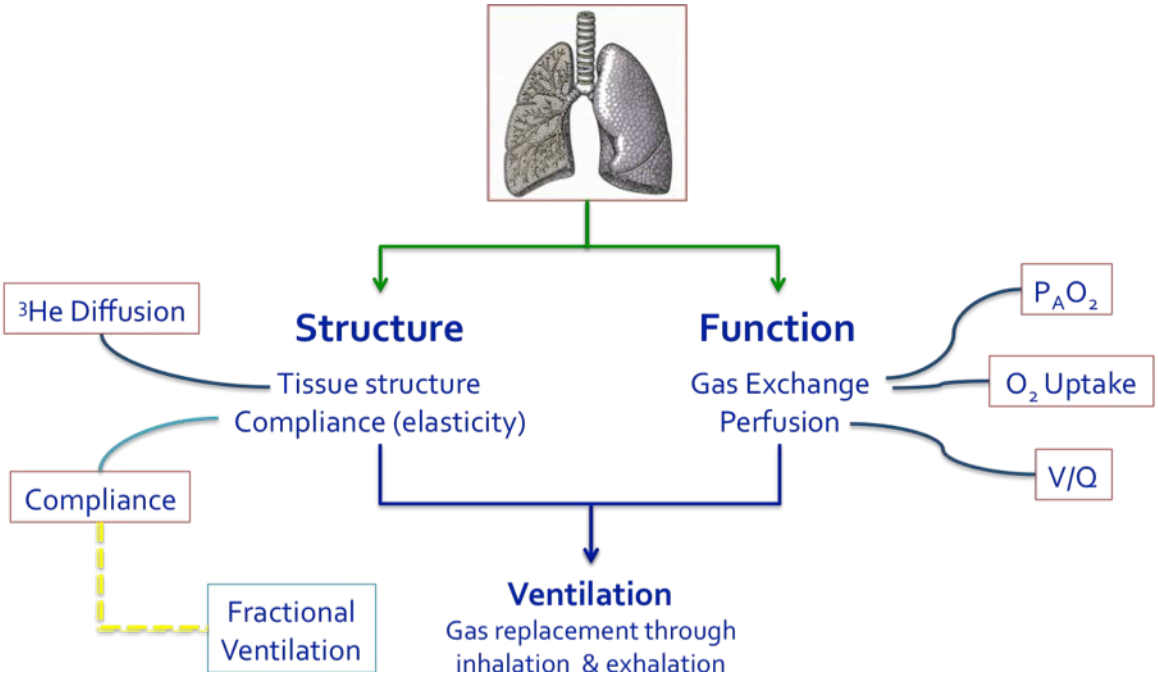

Figure 2.9. The array of structural and functional pulmonary parameters that are in principal measureable by hyperpolarized gas MRI technology.

2.4.4. Hyperpolarized gas MRI

Helium-3 (^{3}He) and Xenon-129 (^{129}Xe) are stable isotopes: two noble gases widely used in lung MRI. Hyperpolarized (HP) ^{3}He was first produced in the early 1960's using optical pumping [3, 4]. For three decades, hyperpolarized ^{3}He was used exclusively in the field of high-energy physics as a target for nuclear scattering experiments. Then in the early 1990's, hyperpolarized ^{129}Xe was used as a gas NMR probe for studies of porous media [5]. Shortly afterwards the first MRI image (a pair of rat lungs inflated with ^{129}Xe) was made in 1994 [6]. Since then, hyperpolarized noble gas MRI has developed into a

distinct field with an emphasis on lung imaging, as shown in Figure 2.9. ^{3}He and ^{129}Xe are currently both used in the pulmonary research community, and each has distinct advantages.

^{3}He is well suited for lung imaging for several reasons. It is an inert gas that can be safely inhaled. Because it is essentially insoluble in blood, the detected MR signals originate exclusively from gas spaces. The gyromagnetic ratio of ^{3}He is high and polarization techniques have steadily improved over the past decade, allowing MRI with high SNR despite the relatively low density of helium at room temperature. ^{3}He has been used to assess ventilation dynamics in healthy and diseased human lungs. Figure 2.10 shows single-breath HP ^{3}He ventilation scans of a healthy human subject compared to that of a mild COPD patient showing areas of ventilation defect. The two are compared to their corresponding ^{1}H MR images. ^{3}He T_1 relaxation is also sensitive to the paramagnetic properties of molecular oxygen [7], a property that has been used to measure regional partial pressure of oxygen (PO_2) [42]. Lastly, the degree of restricted diffusion of ^{3}He inside the alveolar sacs can be measured as the apparent diffusion coefficient (ADC) using MR. This has enabled the detection of disease-driven alterations of alveolar dimensions, e.g. in emphysema [8]. ^{129}Xe on the other hand, is partially soluble in blood and lipids, and as a result, exhibits an anesthetic effect in humans when it reaches brain tissue. ^{129}Xe also exhibits a significant NMR chemical shift when moving from the gas to dissolved phase, a process that can be isolated *in vivo* [9] and exploited for simultaneous regional measurement of pulmonary ventilation and gas exchange [10]. ^{129}Xe has a major

advantage in that it has a natural abundance of 26%. This is in contrast to ^{3}He, which is produced by tritium decay and is extremely rare (~10^{-4} abundance relative to ^{4}He).

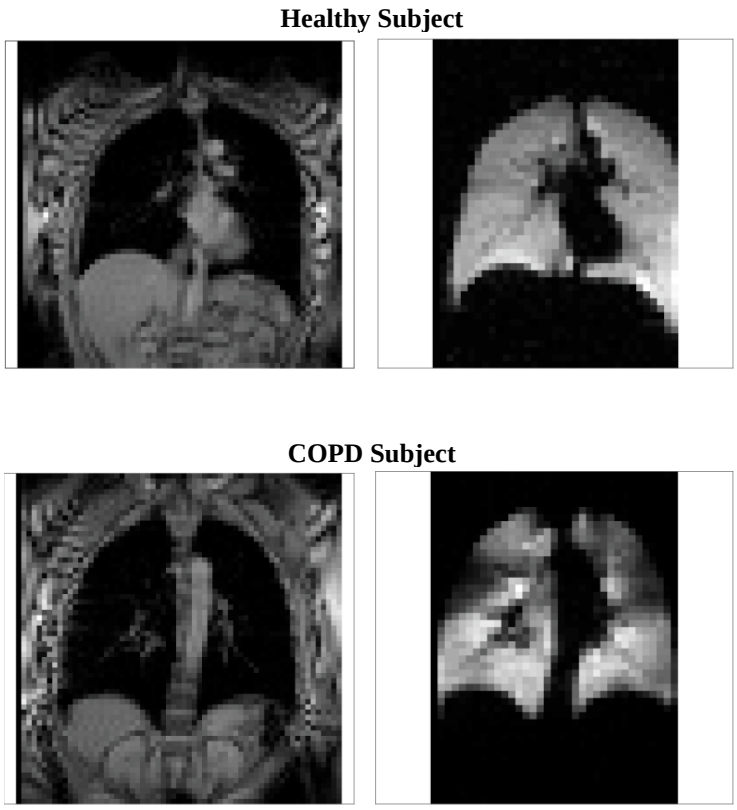

Figure 2.10. Representative ^{1}H and ^{3}He MR images from a healthy volunteer and a COPD patient exhibiting areas of ventilation defect.

2.5. Magnetic Resonance Imaging

2.5.1. Brief history

The nuclear magnetic resonance (NMR) phenomenon was observed independently by two scientists in 1946 [11]. Both scientists, Felix Bloch and Edward M. Purcell, were awarded the Nobel Prize in Physics in 1952. Their success triggered a rapid development of the NMR techniques in the following years. Extensive studies of the relaxation times in solids and even in biological media ensued. But the first results of NMR measurements

in a living animal came from Jackson and Langham in 1968 [12]. In 1971 Raymond Damadian from Downstate Medical Center in Brooklyn showed that the nuclear magnetic relaxation times of normal and tumorous tissues differed [13]. Damadian's discovery encouraged the introduction of NMR into medicine. To complement already existing techniques, new approaches and methods were developed. Erwin L. Hahn in 1950 introduced a method, called *spin echo*, whereby he applied field gradients to study molecular diffusion in liquids [14]. Later in 1954, Carr and Purcell studied the effects of the diffusion on the signal in nuclear magnetic resonance using magnetic field gradients [15].

The 70's witnessed a breakthrough in the technical aspects of the NMR method. All the experiments in the previous decades were one-dimensional, providing no spatial information. This changed in September 1971, when Paul Lauterbur of the State University of New York at Stony Brook applied magnetic field gradients in all 3 dimensions. He used the back-projection technique to create the first NMR images of two water tubes, published in March 1973 [16], followed by images of living animals [17]. The field gradients had been used before in other types of research (e.g. diffusion studies). However, Lauterbur introduced imaging to the NMR field. He was awarded the 2003 Nobel Prize in Medicine or Physiology for his contribution to the invention of magnetic resonance imaging.

In 1974, Richard Ernst realized that Lauterbur's back-projection is not the only method of imaging. Instead, one could use controlled magnetic field gradients in the time domain.

This led to the development in 1975 of the Fourier reconstruction method in imaging, routinely used today [18]. Ernst received the 1991 Nobel Prize in Chemistry for his work in Fourier Transformed NMR and MRI. Several years later, Raymond Damadian produced the first human MRI images when he scanned the whole human body in 1977 [19]. In this same year, Peter Mansfield, leading a group of scientists in Nottingham, England, developed the echo-planar imaging (EPI) technique and presented his first image of the abdomen a year later. The EPI technique would be developed in later years to produce images at real-time video rates (30 ms/frame). Mansfield shared the 2003 Nobel Prize in Medicine or Physiology for the invention of magnetic resonance imaging.

2.5.2. Fundamentals of MRI

Only atoms with an uncoupled non-zero nuclear spin (i.e., having an odd number of protons or neutrons) are capable of producing an NMR signal. Conventional clinical MRI utilizes the uncoupled spin of the highly abundant hydrogen nuclei that are found in water and fat inside the human body. For nuclear spin $-\frac{1}{2}$ systems such as ^{1}H and ^{3}He, the net polarization P of an ensemble of spins can be defined as:

$$P \equiv \frac{N_{+} - N_{-}}{N_{+} + N_{-}} \qquad [2.1]$$

where N_{+} and N_{-} refer to the number of spins in the nuclear spin sublevels $+\frac{1}{2}$ and $-\frac{1}{2}$, respectively. The bulk magnetization M_0 of a collection of spins is:

$$M_0 = \frac{1}{2} N \gamma \hbar P \qquad [2.2]$$

where N is the total number of spins, h is the Planck's constant (6.63×10^{-34} m^2 kg s^{-1}), and γ is their gyromagnetic ratio, a known constant unique to an atom; e.g. $\gamma(^{1}\text{H}) = 42.58$

MHz/T, $\gamma(^{129}\text{Xe})$ = 11.86 MHz/T, $\gamma(^{3}\text{He})$ = 32.44 MHz/T. We note the conventions $\lambda = 2\pi \cdot \lambda\!\!\!^{-}$ and $h = 2\pi \cdot \hbar$. At a given temperature T and an external magnetic field B_0, P follows a thermal equilibrium:

$$P = \tanh\left(\frac{\gamma \hbar B_0}{2kT}\right) \approx \frac{\gamma \hbar B_0}{2kT} \qquad [2.3]$$

where k is the Boltzmann constant (1.38×10^{-23} m^2 kg s^{-2} K^{-1}). The approximation is valid for all practical cases because the magnitude of the nuclear magnetic moment is extremely small. At 300 K and 1 T, P = 3.4 × 10^{-6} for protons in water. This small polarization factor, in combination with the small proton magnetic moment, is the reason why a large B_0 is desirable for conventional ^{1}H NMR and MRI. Therefore at thermal equilibrium, the magnetization per unit volume of a sample of spins is given by:

$$\vec{M} \approx \frac{\gamma^2 h^2 N B_0}{16\pi^2 kT}\hat{z} \qquad [2.4]$$

This magnetization vector is tipped into the transverse plane to give rise to the actual signal that is measured with MR. The time evolution of the magnetization vector $\vec{M}$ can be described by the classical Bloch equation:

$$\frac{d\vec{M}}{dt} = \vec{M} \times \gamma\vec{B} - \frac{M_x\hat{i} + M_y\hat{j}}{T_2} - \frac{(M_z - M_0)\hat{k}}{T_1} \qquad [2.5]$$

Accordingly, the longitudinal magnetization (M_z) is governed by:

$$\frac{dM_z}{dt} = -\frac{M_z - M_0}{T_1} \qquad [2.6]$$

with the following general solution:

$$M_z = M_0 + \left(M_z(0) - M_0\right) \cdot \exp(-t/T_1)\ . \qquad [2.7]$$

The transverse component of magnetization (M_{xy}) behaves according to:

$$\frac{dM_{xy}}{dt} = -\frac{M_{xy}}{T_2} \qquad [2.8]$$

with the following general solution after applying a 90˚ RF excitation, also known as the *free induction decay*, FID:

$$M_{xy} = M_0 \cdot \exp(-t/T_2). \qquad [2.9]$$

In above equations, T_1 is the characteristic decay time of the longitudinal magnetization and T_2 is the intrinsic decay time of the transverse magnetization in a uniform magnetic field. However, any background gradients G due to inhomogeneities of the static holding field B_0 further increase the decay rate of the transverse magnetization due to incoherent dephasing of the spins. In presence of a background gradient G, the signal decay is not simply an exponential. For instance, under the influence of diffusion, the decay term has components proportional to $\exp(-\frac{2}{3}\gamma^2 G^2 D t^3)$, where D represents the diffusion coefficient. In general, however, it is customary to describe the decay of the transverse magnetization as an exponential decay with characteristic decay time T_2^* given by:

$$\frac{1}{T_2^*} = \frac{1}{T_2} + \frac{1}{T_2'} \qquad [2.10]$$

where $1/T_2'$ is the additional decay rate due to the static inhomogeneities in B_0. A reasonable approximation to this additional decay rate is $1/T_2' = \gamma \Delta B_0$, where ΔB_0 is the change in the magnetic field that occurs over the range of the sample. Equation [2.10] implies that $T_2 \geq T_2^*$. Furthermore, after the magnetization has returned to equilibrium, there can be no transverse magnetization left. Therefore, the decay time of the transverse magnetization must be less than or equal to the longitudinal relaxation time $(T_1 \geq T_2)$. Hence, we find in general:

$$T_1 \geq T_2 \geq T_2^* . \qquad [2.11]$$

2.5.3. Effect of RF pulses on signal behavior

The rapid decay of the FID with decay time T_2^* due to field inhomogeneities can represent a great obstacle for MRI measurements. However, since these inhomogeneities are static in nature one can recover part of the signal in a so called *spin echo* [14]. A prototypical spin echo uses a $\theta = 180°$ RF refocusing pulse applied at time τ (refocusing time) after an initial RF excitation pulse. First a 90° pulse flips the longitudinal magnetization into the transverse plane. Then the 180° refocusing pulse, flips the local magnetization vectors about a line in the transverse plane. For instance, if the spins are flipped about the *x*-axis, the individual phases ϕ go to $-\phi$, whereas a spin flip about the *y*-axis transforms ϕ to $180°-\phi$. After the phases are conjugated, the spins whose phases were lagging behind the mean phase (those in a local environment of lower magnetic field) are then ahead, whereas phases that were ahead of the mean phase (those in a local environment of higher magnetic field) are then behind. Therefore, at time 2τ, the spins in a local environment of higher magnetic field will have exactly caught up with the spins in a local environment of lower magnetic field and maximum macroscopic signal coherence is reestablished producing an *echo*.

However, the intrinsic T_2 decay which is due to random fluctuations in the magnetic field on a microscopic level cannot be refocused with such a spin echo, so that the maximum signal that can be recovered at the echo is still attenuated by T_2 decay. If additionally the effect of diffusion of the spins during the time interval 2τ is taken into account, the signal

recovery will be further reduced, since individual spins may have been subject to different local fields during the dephasing (before the 180° pulse) and rephasing (after 180° pulse), and refocusing will be incomplete.

2.5.4. Using gradients to produce MR images

MRI uses the dependence of the Larmor frequency on the local field strength to convert position information into frequency information in the MR signal. By superimposing a linear magnetic field variation, or gradient, on top of the main magnetic field B_0, the resulting MR signal will have different frequency components depending on the position from which the signal emanates. At each location $\vec{r}$, the transverse magnetization will rotate at a frequency given by the Larmor relation:

$$\omega(\vec{r}) = \gamma B(\vec{r}) \qquad [2.12]$$

If a magnetic field gradient of an idealized form $\vec{G} \equiv \frac{\partial B_z}{\partial x}\hat{x} + \frac{\partial B_z}{\partial y}\hat{y} + \frac{\partial B_z}{\partial z}\hat{z}$ is superimposed on the main holding magnetic field B_0, the combined field in the $\hat{z}$ direction is given by:

$$B_z(\vec{r}) = B_0 + \vec{G} \cdot \vec{r} \qquad [2.13]$$

Hence the local *Larmor* frequency becomes:

$$\omega(\vec{r}) = \gamma B_0 + \gamma \vec{G} \cdot \vec{r} \qquad [2.14]$$

The quantity of interest is the difference $\Delta\omega$ between the local Larmor frequency and ω_0:

$$\Delta\omega \equiv \omega(\vec{r}) - \omega_0 = \gamma \vec{G} \cdot \vec{r} \quad (2.39) \qquad [2.15]$$

which linearly maps the spatial variable $\vec{r}$ into frequency space ($\Delta\omega$). This mapping process using a linear field gradient, called *frequency encoding*, is the basis for making

MR images from the basic NMR signal, and was key to the insights for which Paul Lauterbur was awarded the Nobel Prize in 2003. Ignoring for the moment the diffusion, as well as T_2 and T_2^* relaxation effects, the total MR signal $S(t)$ is proportional to the coherent superposition of the magnetization density $M(\vec{r})$ throughout the sample and can be written as:

$$S(t) \equiv \int M(\vec{r}) \cdot \exp\left(-i\Phi(\vec{r},t)\right) \cdot d\vec{r} \qquad [2.16]$$

where $\Phi(\vec{r},t)$ is the relative phase of each magnetic moment in the transverse plane after demodulation and is given by:

$$\Phi(\vec{r},t) = \int_0^t \Delta\omega(\vec{r},t')dt' = \int_0^t \gamma\vec{G}(t') \cdot \vec{r}\,dt' \qquad [2.17]$$

To illustrate the imaging capability of MRI we consider a 1D example with a constant gradient G. In presence of such a gradient along the x-axis, the effective magnetic field becomes:

$$B_x(x) = B_0 + Gx \qquad [2.18]$$

and hence:

$$\Delta\omega(x) = \gamma Gx \qquad [2.19]$$

The time dependent phase is given by:

$$\Phi(x,t) = \int_0^t \gamma\vec{G}x\,dt' = \gamma Gxt \qquad [2.20]$$

The signal therefore becomes:

$$S(t) \equiv \int M(x) \cdot \exp\left(-i\gamma xGt\right) \cdot dx \qquad [2.21]$$

It is convenient at this point to define the quantity:

$$k(t) \equiv \frac{\gamma}{2\pi}\int_0^t G(t')dt' \qquad [2.22]$$

which corresponds to a spatial frequency k describing the magnetization density $M(x)$. For a constant gradient, this reduces to $k(t) \equiv \gamma Gt/2\pi$. Substituting this into Equation [2.21], we can write the signal as a function of k:

$$S(k) \equiv \int M(x) \cdot \exp(-i2\pi xk) \cdot dx \qquad [2.22]$$

Once in this form, we can obtain the magnetization density $M(x)$ by taking the inverse Fourier transform:

$$M(x) \equiv \int S(k) \cdot \exp(i2\pi xk) \cdot dk \qquad [2.23]$$

As can be seen, the signal S when expressed as a function of k, is related to the spin density $M(x)$ through a Fourier transform. In fact k and x couple in a similar fashion as f and t in temporal Fourier transforms. That is why k is referred to as a spatial frequency.

Extension to 2D imaging is straightforward. Next we consider a spin density on a plane given by $M(x,y)$, and assume that we have a gradient G_x that acts for a time t_x and a gradient G_y that acts for a time t_y. The phase at each point will then be given by:

$$\Phi(x,y,t_x,t_y) = x\gamma\int_0^{t_x} G_x(t')dt' + y\gamma\int_0^{t_y} G_y(t')dt' \qquad [2.24]$$

Defining:

$$k_x(t) \equiv \frac{\gamma}{2\pi}\int_0^{t_x} G_x(t')dt' \qquad [2.25.a]$$

$$k_y(t) \equiv \frac{\gamma}{2\pi}\int_0^{t_y} G_y(t')dt' \qquad [2.25.b]$$

the signal equation can be written as:

$$S(k_x,k_y) = \int M(x,y)\cdot\left[-i2\pi(xk_x + yk_y)\right]\cdot dxdy \qquad [2.26]$$

and the spin density $M(x,y)$ follows by taking the inverse Fourier transform:

$$M(x,y) = \hat{f}_{2D}^{-1}\{S(k_x,k_y)\} \qquad [2.27]$$

The process of image acquisition therefore reduces to the task of acquiring enough points (k_x, k_y) in the *k*-space in order to be able to faithfully reconstruct the 2D spin density function using a discrete Fourier transform. In practice, this is accomplished by turning on the magnetic field gradients for specific periods of time, and sampling the MR signal under the influence of these gradients. There are numerous ways for performing this process. A particularly simple example, and the most commonly used method, is described as follows.

Initially G_y is turned on for some period of time t_y, and then turned off. We now have established a value of k_y according to Equation [2.25.b]. In this context, G_y is known as the *phase-encoding* gradient. Next, G_x is turned on for a period of time t_x, during which the signal is continuously acquired. If G_x is constant during this time, k_x is given by $k_x(t) \equiv \gamma G_x t/2\pi$. Thus the value of the signal at different times corresponds simply to the value of the signal for different values of k_x according to Equation [2.25.b]. In this context, G_x is known as the *readout* gradient. Usually, the signal is sampled during the readout gradient by integrating over fixed time intervals Δt. Signal samples are therefore acquired corresponding to discrete points (k_x, k_y) in *k*-space. The signal can also be sampled at negative values of k_x or k_y by simply using negative values for G_x or G_y respectively.

The mathematical description embodied in Equations [2.12]–[2.27] was implicitly developed in terms of a variable k with infinite and continuous extent in k-space. In the example discussed in the previous paragraph, however, k-space is sampled discretely over a finite range of values. In practice, the maximum achievable values of k_x and k_y, are limited by the maximum achievable gradient strength in combination with the finite acquisition time (which determines the extent of k-space sampled). Furthermore, the signal sampling rate $1/\Delta t$ of the data acquisition during the readout gradient, and thus the sampling rate of k_x, is limited by the non-zero sampling time step Δt. Similarly, the sampling rate of k_y is in practice also limited by the discrete nature of the acquisition.

There are two parameters that relate the sampling coverage of k-space to the resulting image quality. The resolution, Δx, of the reconstructed image is inversely related to the maximum k-space value k_{max} acquired. In order to obtain higher resolution, higher spatial frequencies need to be sampled, as follows:

$$\Delta x = \frac{1}{2k_{max}} \qquad [2.28]$$

The other relevant parameter is the maximum field of view (FOV) of the image that can be supported by the reconstruction, and is related to the sampling density of k-space, Δk. In the example for k_x given above, Δk is proportional to the sampling time step Δt. In order to be able to image a larger object, k-space data needs to be more sampled more densely. The relationship between the FOV and k-space sampling density is given by the Nyquist criterion:

$$\text{FOV} \leq \frac{1}{\Delta k} \qquad [2.29]$$

If the imaged sample is larger than the supported FOV, the Nyquist criterion is violated, and any signal outside the supported FOV is *folded back* into the FOV where it overlays and hence interferes with the image, a phenomenon referred to as *aliasing*.

2.5.5. Acquisition methods

A dedicated application of RF pulses, magnetic field gradients, and data acquisition (to collectively allow MR imaging) is called a *pulse sequence*. Since most MRI is done in a 2D plane, the following discussion is restricted to 2D acquisition schemes. In general, the ultimate goal of any 2D pulse sequence reduces to sampling *k*-space, by applying magnetic field gradients in both *x* and *y* directions, to a sufficient extent to allow reconstruction of the image via a Fourier transform. Therefore, the following direct correspondence holds:

$$S(G_x, G_y, t) \xrightarrow{\text{Sample } k\text{-space}} S(k_x, k_y) \xrightarrow{\text{Fourier Transform}} m(x, y)$$

indicating that the time-dependent NMR signal can be manipulated by magnetic field gradients to yield $S(k_x,k_y)$ which in turn can be used to create an MR image via a Fourier transform. There are many different MR methods that can be used to sample *k*-space. The most elementary approach is to fill *k*-space in a rectangular fashion on a Cartesian grid one line at a time, as described in the previous section, and show in Figure 2.11.

The RF pulse tips all or only part of the longitudinal magnetization into the transverse plane. The gradient G_z along the *z*-axis is applied during the RF pulse which has a sinc-like envelope, as opposed to a simple rectangular pulse. This allows for only flipping the

magnetization along a certain interval of *z* into the transverse plane using a process called *slice-selective excitation*. At the simplest level, if a gradient is applied along the *z*-axis, only one value of *z* will be in resonance for a particular RF frequency. This process is slightly more complicated in practice. However it can be shown that the slice profile (the *z*-dependence of the resulting transverse magnetization) is approximately the Fourier transform of the time dependent envelope of the RF pulse. Since the Fourier transform of a sinc function is a rectangle function, the application of a sinc-like envelope to the RF pulse, in the presence of a magnetic-field gradient in the *z* direction, excites a narrow range of frequencies corresponding to a 2D plane (or a *slice*) perpendicular to the *z*-axis.

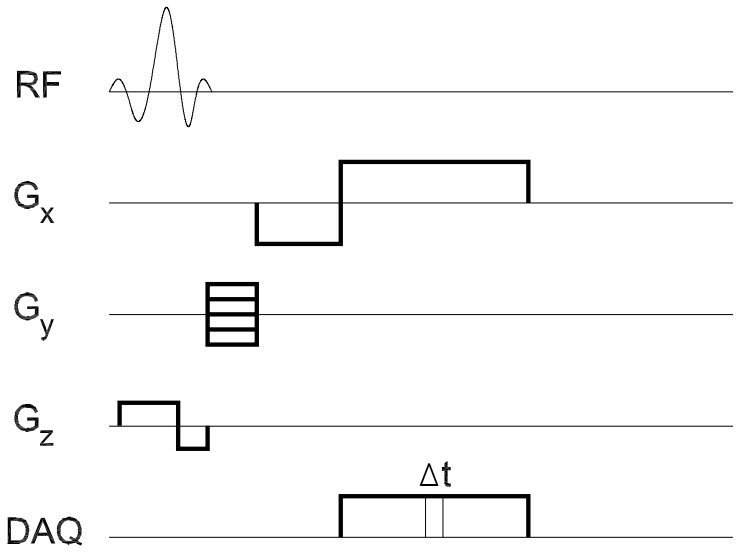

Figure 2.11. General timing diagram for a gradient echo MR imaging pulse sequence.

After applying the RF excitation pulse, which may or may not be slice-selective, the subsequent gradients along the *x* and *y* axis (G_x and G_y) are used to traverse *k*-space along k_x and k_y, respectively. G_y (the phase encoding gradient) moves the *k*-vector along the k_y

axis. Next, the negative lobe of the gradient G_x moves the *k*-vector along the k_x axis in the negative direction. Two examples are shown in Figure 2.12 for a positive and a negative G_y. The positive lobe of the readout gradient G_x is applied at the same time as the data are acquired and moves the *k*-vector horizontally from left to right, forming a so-called *gradient echo* as it passes through $k_x = 0$. During the readout gradient, data is sampled by the data acquisition system (DAQ) at a fixed Δt which determines Δk_x and hence the readout FOV. During the next RF cycle a different value of G_y, is chosen to traverse a different horizontal line in *k*-space, and this procedure is repeated until the desired range of *k*-space has been covered. The Cartesian acquisition is convenient, since the image can be reconstructed from the data sampled in *k*-space using a Fast Fourier Transform (FFT), which requires the data to lie on a uniform grid, and which is much faster than direct computation of the Discrete Fourier Transform (DFT).

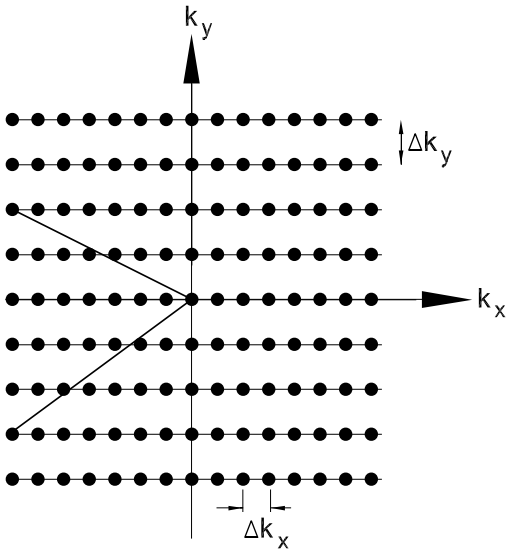

Figure 2.12. Cartesian sampling of *k*-space using G_x and G_y gradients.

2.6. Hyperpolarized gas MRI

The thermal polarization of nuclear spins described by Equation [2.3] is typically on the order of 10^{-6} for customary magnetic fields in the order of a few Tesla. Despite this low polarization, the high abundance of hydrogen inside the human body (about 100 mole/liter) results in a sufficient magnetization to make tissue imaging feasible, as shown in Figure 2.8. It is also evident from this image that the lung does not generate appreciable MR signal. This is due to both the low tissue density in the lung as well as a short T_2^* because of magnetic-field inhomogeneities due to susceptibility mismatch at the large numbers of tissue-gas interfaces. However, as mentioned above, certain gas nuclei (^{3}He, ^{129}Xe) can be polarized well above the Boltzmann thermal equilibrium value. These HP gases can then be inhaled and imaged, as an alternative to conventional MRI of hydrogen nuclei. Despite the inherently low density of the gas species, the significant polarization, on the order of 50% of the spin population results in sufficient magnetization to make lung MRI feasible.

2.6.1. Hyperpolarization

^{3}He placed in a static magnetic field will also achieve a Boltzmann polarization, as in Equation [2.3]. However, for all practical purposes the net magnetization of a 1 L sample of ^{3}He at atmospheric pressure is miniscule in comparison to the equivalent sample volume of water, owing primarily to the smaller density of ^{3}He. The net result is a total ^{3}He magnetization that is 2.3×10^{-4} smaller than water for an equivalent volume at a given B_0. This makes conventional MRI with thermally polarized ^{3}He impractical even with the most sensitive detectors.

Hyperpolarization refers to a process whereby nuclear moments are polarized to a level greater than the Boltzmann level (Figure 2.13). For ^{3}He, P can be increased to 0.1–0.6 by spin exchange optical pumping techniques, described in detail in published literature [4, 20-22]. This ~10^5 improvement over thermal polarization results in a net magnetization that equals or exceeds that of an equivalent volume of water, and thus makes ^{3}He MRI a practical imaging modality.

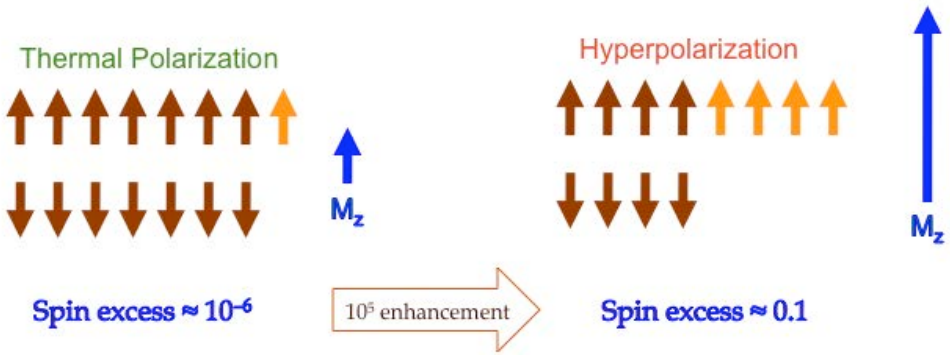

Figure 2.13. Schematic comparison of the thermal polarization versus hyperpolarized spins states.

A typical protocol for the production of HP ^{3}He starts by flowing high purity ^{3}He into a rubidium-containing spherical glass cell at a gauge pressure of about 5–8 atmospheres. The glass cell is then heated up to approximately 150–170 °C, during which some of the rubidium in the glass cell vaporizes. A laser light is emitted on the glass cell for several hours, optically pumping the atoms in the rubidium vapor, which in turn hyperpolarize the ^{3}He through collisional spin-exchange. The ^{3}He polarization grows exponentially with time according to the simplified relation:

$$P(t) = (P_A)\frac{\Gamma_{se}}{\Gamma_{se} + R_1}\left[1 - \exp\left(-(\Gamma_{se} + R_1)t\right)\right] \qquad [2.30]$$

where (P_A) is the rubidium spin polarization, and Γ_{se} the spin-exchange rate, which is directly proportional to the rubidium density [Rb]. At the end of the polarization process, the cell is cooled for the rubidium vapor to condense. The HP ^{3}He can then be transported, usually through a sterile Tedlar bag, to the MRI magnet for use.

2.6.2. T_1 Recovery versus T_1 decay

The thermal polarization levels described by the Boltzmann distribution (Equation [2.3]) apply to a system in equilibrium. In conventional MRI the protons are in equilibrium prior to excitation by an externally applied RF pulse. After this RF pulse is applied the protons begin recovering to their initial polarization level with the time constant T_1. Hyperpolarized agents are by definition not in equilibrium. They are specifically prepared to be polarized far in excess of the Boltzmann polarization and therefore begin to decay back to the thermal equilibrium once they are removed from the special conditions that induced the hyperpolarization. The time constant at which this happens is also T_1, the longitudinal rate of signal recovery and decay described for ensemble spins by the Bloch Equation [2.6]–[2.7]. Therefore once hyperpolarized magnetization of ^{3}He is used, it cannot be regained since the T_1 is too long, ranging from 10 sec to many hours depending on the local environment. Each time an RF pulse is applied the available magnetization is therefore decreased according to:

$$M_n = M_0 \cos^n \alpha \qquad [2.31]$$

where M_n is the magnetization after the n-th applied RF pulse flip angle α and M_0 is the initial longitudinal magnetization.

*T*he T_1 decay reduces the total available magnetization and ultimately the SNR in the acquired data. The principle source of T_1 decay in *in vivo* HP ^{3}He MRI is the interaction of the ^{3}He nucleus with paramagnetic O_2 molecules. For a given partial pressure of oxygen, PO_2, the T_1 is given by [7],

$$T_{1,O_2} = \frac{\xi}{PO_2} \qquad [2.32]$$

where ξ is a constant, 2.61 bar.s at body temperature. For a normoxic mixture (0.2 bar) this gives a T_1 of approximately 13 sec.

2.6.3. Limitation on imaging resolution with HP gas MRI

The HP ^{3}He MR images shown in Figure 2.10 were acquired in human lungs using a standard Cartesian imaging pulse sequence. The typical resolution of such images is on the order of a few millimeters. The achievable resolution of HP noble gas MR images is fundamentally limited by:

1. Signal-to-noise ratio (SNR): A higher resolution requires smaller image pixels. For a given FOV the signal per pixel is inversely proportional to the number of image pixels *N*, while the noise per pixel is inversely proportional to $\sqrt{N}$. Hence, the SNR scales as $1/\sqrt{N}$ which means that a higher resolution (increasing *N*) reduces the SNR per pixel. Hence, there is always a tradeoff between SNR and resolution.

2. Blurring due to T_2 or T_2^* decay during the MR acquisition: When the MR signal $S(t)$ (and thus the *k*-space data $S(k)$) is modulated with an exponentially decaying function

(such as T_2 or T_2^* decay), the Fourier transform of the signal is convolved with a Lorentzian function in the spatial domain, a phenomenon which is called *line broadening* in spectroscopy. This line broadening causes the signal originally contained in one pixel to bleed into adjacent pixels, thereby blurring the image.

3. Blurring due to diffusion of the spins during the MR acquisition: The diffusion resolution limit is a combination of the fact that the spin's Brownian motion tends to smear out their actual location as well as the fact that diffusion during the application of imaging gradients causes signal attenuation and thus line broadening in the spatial domain, identical to the effects of T_2 or T_2^* decay. The resolution limit imposed by diffusion is much more important to noble gas MRI than to conventional MRI due to the much higher diffusion coefficients of gas molecules. These factors make it extremely difficult to obtain hyperpolarized gas lung images with effective resolution less than a millimeter in human subjects using a clinical scanner.

CHAPTER 3: Theory of Fractional Ventilation

3.1. Introduction

A technique for the quantitative measurement of regional pulmonary ventilation was originally developed by Deninger, *et al.* [23]. This method was based on signal build-up in the lung after the subject inhales a sequence of HP gas breaths. In its proposed form, this technique is only suitable for mechanically ventilated small animals, as it requires many HP gas breaths and a relatively long acquisition time. These properties make the implementation of this technique impractical in both large animals and humans. In this chapter an improved technique for imaging quantitative regional lung ventilation is developed and described. The proposed method allows for acquisition of similar regional ventilation information over a much shorter time scale and with substantially fewer HP gas breaths. Furthermore, this work discusses some important issues related to dead space modeling related to regional measurements of lung ventilation.

3.2. Fractional ventilation model

Airway fractional ventilation, r_A, is defined as the ratio of the amount of fresh gas added to a volume element in the lung during inspiration, noted as V_f, to the total gas space of that volume element at the end of inspiration, V_t (comprised of V_f and the residual volume V_r):

$$r_A = \frac{V_f}{V_t} = \frac{V_f}{V_f + V_r} \ . \qquad [3.1]$$

A voxel's gas content at end-inspiration under breath-hold pressure is assumed to be divided between fractions: r_A, consisting of the delivered fresh gas, and $q_A = 1 - r_A$, representing the residual capacity of the volume element. A measurement of $r_A = 0$ indicates no gas replacement (e.g. completely occluded airways), and $r_A = 1$ indicates complete gas replacement with each breath (e.g. conductive airways).

Over a succession of hyperpolarized gas breaths, the net magnetization of ^{3}He in highly-ventilated regions grows at a faster rate than in the poorly-ventilated ones. Theoretically after an infinite number of ^{3}He breaths, the available magnetization in each region of the lung will converge to a steady state value (M_∞) specific to each region, which is proportional to the total airway volume present in the respective region-of-interest (ROI).

In general the resulting ^{3}He magnetization within a given volume element after inhalation a HP gas breath is a function of the magnetization of the fraction r_A of the fresh ^{3}He and magnetization of the fraction q_A of the ^{3}He remaining from previous breaths. During the time interval between the two breaths, the polarization of ^{3}He decays according to the partial pressure of oxygen (PO_2) present in the airways (P_AO_2 in the alveoli). The relaxation time constant is governed by $T_{1,O_2} = \xi / PO_2$, with the proportionality constant $\xi \approx 2.6 \ \text{bar} \cdot \text{s}$ at normal body temperature [7]. Since the partial pressure of oxygen in the airways can vary with time either by oxygen uptake in the alveoli or oxygen

concentration in the delivered gas to the lungs, T_{1,O_2} can in general be a time-varying quantity.

3.3. Point object model

In order to incorporate the effect of flip angle history in the ventilation measurements, a simple model of a point object adopted. For each image the signal distribution will be a function of B_1 field and the resulting RF pulse flip angle, α, and the HP gas spin density distribution. In the simple case of a single voxel object, the resulting signal magnitude is proportional to the available transverse magnetization M_{xy}. When subject to a train of RF pulses with fixed flip angle (e.g. for different phase encoding gradients), due to lack of recovery of longitudinal magnetization, M_{xy} decays with a factor of $\sin\alpha \cdot \cos^i \alpha$, corresponding to the *i*-th pulse:

$$\begin{aligned} &i = 0: \;\; M_{xy} = M_A(0) \cdot \sin\alpha \\ &i = 1: \;\; M_{xy} = M_A(0) \cdot \sin\alpha \cdot \cos\alpha \\ &i = 2: \;\; M_{xy} = M_A(0) \cdot \sin\alpha \cdot \cos^2\alpha \\ &\vdots \\ &i = N_{PE}: \;\; M_{xy} = M_A(0) \cdot \sin\alpha \cdot \cos^{N_{PE}-1}\alpha \end{aligned} \qquad [3.2]$$

Therefore the acquirable signal from an image with N_{PE} phase encode lines can be expressed as a function of all M_{xy} values available in that image. We approximate the signal intensity in each image with an equivalent of a point object, subject to an RF pulse train with fixed α, and N_{PE} phase encode lines, as follows:

$$S_A(j) = \zeta \cdot \left[M_A(j) \cdot \frac{\sin\alpha}{N_{PE}} \sum_{i=0}^{N_{PE}-1} \cos^i \alpha \right], \qquad [3.3]$$

with ξ as a proper scaling factor. In the asymptotic case of small flip angle values, this relationship can be simplified as:

$$\lim_{\alpha \to 0} S_{\mathrm{A}}(j) = \xi \cdot \left[M_{\mathrm{A}}(j) \cdot \frac{\alpha}{N_{\mathrm{PE}}} \right]. \qquad [3.4]$$

Even though the actual observed signal value for a given voxel in a non-point object (e.g. a 2D or 3D object) is a complex function of the geometry and heterogeneity of the imaged object, this description of S_{A} provides a measure of the available transverse magnetization convertible to MR signal during an image acquisition.

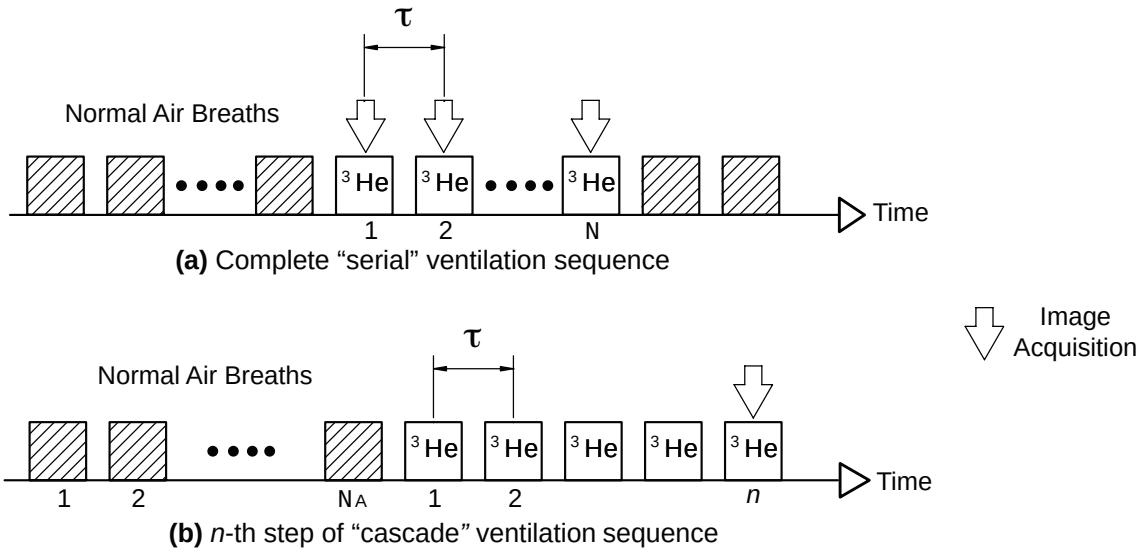

Figure 3.1. Schematic diagram of **(a)** the complete *serial* ventilation sequence, during which one image is acquired after each HP ^{3}He breath (for a total of N images); and **(b)** the n-th step of *cascade* ventilation sequence, during which one image is acquired at the end of the n-th HP ^{3}He breath. Acquiring a complete series of ventilation images requires repeating this sequence N times.

3.4. Signal dynamics of the *cascade* ventilation sequence

In Deninger's model of hyperpolarized gas magnetization buildup in the lung [23] – referred to as the *cascade* method in this manuscript – each ROI is considered a single-compartment inflatable volume element which engages in the inhalation/exhalation process with each breath. Each compartment is assumed to have one port through which

fresh polarized gas enters and leaves the volume at end-inhale and end-exhale respectively. The proposed method for measuring fractional ventilation consists of acquiring an image after ventilating the lung with a given number of HP gas breaths with a short end-inspiratory breath-hold in each respiratory cycle. This procedure repeated several times with an increasing number of polarized gas breaths. Figure 3.1(b) shows the *n*-th step of this ventilation sequence corresponding to *n* HP gas breaths. The time interval between two consecutive breaths is equal to τ. Polarized gas breaths in each step are separated by N_A number of air breaths to wash out the residual HP gas and to oxygenate the lung. This sequence will be repeated as many times as necessary to acquire the desired number of datapoints on the signal buildup curve for each volume element.

The available magnetization in the airways at each step of the cascade ventilation sequence can be recursively expressed for the *j*-th breath as a function of the fresh and residual gas from the previous step:

$$M_A(j) = r_A \cdot M_S \cdot \exp[D_{EXT}] + (1 - r_A) \cdot M_A(j-1) \cdot \exp\left[D_{O_2}\right], \qquad M_A(0) = 0. \qquad [3.5]$$

M_S is the source magnetization of the HP ^{3}He from the reservoir that is available to the volume element of interest. Even though at any given time the source polarization in the reservoir is the same for all regions of the lung, the total magnetization available to an ROI is limited to the airway volume specific to that region, and therefore at steady state: $M_\infty = \lim_{j\to\infty} M(j) = M_S$. This magnetization is subject to external decay of ^{3}He polarization in the reservoir, $D_{EXT} = -t(n)/T_{1,EXT}$, at any given time $t(n)$, in the *n*-th step of the cascade ventilation sequence. The total elapsed time from the beginning of the experiment is a function of the number of delivered ^{3}He breaths, *n*, and the number of air

breaths, N_A, between each ventilation step. The external relaxation time constant $T_{1,EXT}$ is primarily a function of the position of the HP ^{3}He bag in the magnetic field and the wall relaxation of ^{3}He molecules inside the container bag [24], and is experimentally measured for each study. The oxygen-induced depolarization of ^{3}He during each breath is governed by $D_{O_2} = -\tau / T_{1,O_2}$.

In practice N images will be acquired during the cascade ventilation sequence and Equation [3.5] will be fit to the datapoints on a voxel-by-voxel basis to yield M_S and r_A as free parameters for each volume element. Since only one set of images are acquired during the last HP gas breath of each step, and all the residual gas is washed out of the airways using the intermediate air breaths, the signal magnitude at each image is independent of that of the previous steps in regards to the corresponding flip angle history, and therefore it is not necessary to include the RF pulse flip angle effect in this fitting process.

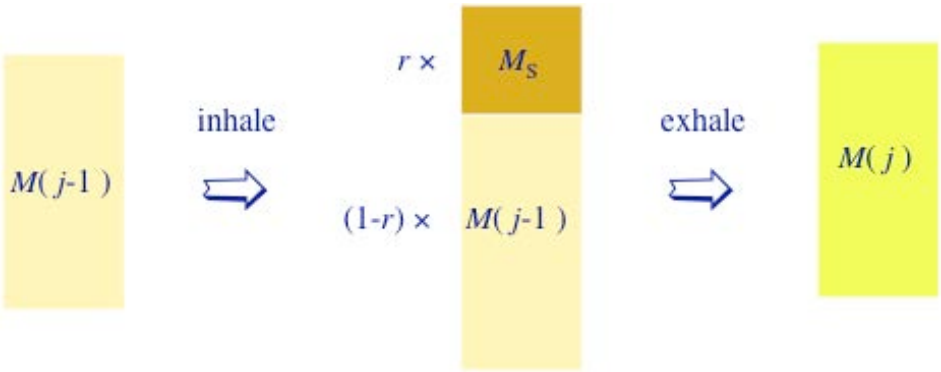

Figure 3.2. Model of fractional replacement of inspiratory gas with residual gas in the airways.

3.5. Signal dynamics of the *serial* ventilation sequence

In contrast to the cascade method, the proposed approach in this manuscript utilizes a series of back-to-back HP gas breaths at the end of which an image is acquired during a

breath-hold. This method is referred to as the *serial* ventilation sequence. In a similar fashion, each ROI is considered a single-compartment inflatable volume element with one port through which fresh polarized gas enters and leaves the volume. Figure 3.1(a) shows the complete serial ventilation sequence to acquire N images to form the signal buildup curve for each volume element.

The available magnetization in the airways at each step of the serial ventilation sequence can be recursively expressed as a function of the freshly arrived and the residual ^{3}He from the previous step, as shown in Figure 3.2:

$$M_A(j) = r_A \cdot M_S + (1 - r_A) \cdot M_A(j-1) \cdot \exp\left[D_{RF} + D_{O_2}\right], \qquad M_A(0) = 0. \qquad [3.6]$$

where similar terms have the same definitions as in Equation [3.5]. The primary difference in signal evolution between the serial and cascade ventilation sequences lies in ^{3}He polarization decay mechanisms. The time scale of the experiment ($N \cdot \tau$) is typically two orders of magnitude smaller than the external depolarization time constant, $\tau << T_{1,EXT}$, and therefore the external decay rate of polarization in the reservoir, D_{EXT}, is negligible in the serial ventilation sequence. The RF depolarization effect $D_{RF} = N_{PE} \cdot \ln(\cos\alpha)$, however, is critically important since the residual fraction of the gas in the airways is repeatedly exposed to RF excitations and therefore the RF-induced decay at each breath affects the available magnetization for the following images. It is therefore necessary to obtain the regional flip angle information for each voxel. The observable signal in each image is approximated in a similar fashion as expressed by Equation [3.3]. In practice N images will be acquired during the serial ventilation

sequence and Equation [3.6] will be fit to the datapoints on a voxel-by-voxel basis to yield M_S and r_A as free parameters for each volume element.

3.6. Evolution of oxygen tension

As described earlier, the oxygen-induced depolarization rate of HP ^{3}He, T_{1,O_2}, is a function of the oxygen tension in the airways. Neglecting the uptake of oxygen into the blood during each breath [23, 25], partial pressure of oxygen in the airways, P_A, at the beginning of each ^{3}He breath can be recursively expressed as a function of the oxygen concentration of the freshly arrived gas, P_S, and that of the residual gas in the airways from the previous breath:

$$P_A(j) = r_A \cdot P_S + (1 - r_A) \cdot P_A(j-1), \qquad P_A(0) = P_A O_2 = 140 \text{ mbar}. \qquad [3.7]$$

3.7. Dead space model

Figure 3.3 shows a typical model of respiratory dead space distribution in human lungs [26], comprising the common dead space (V_{DC}), regional dead space (V_{DR}) and alveolar gas volume (V_A). Following the same approach, the dead space volume in the ventilation system can be divided into two main components, as shown in Figure 3.4(a), illustrating a schematic layout of the ventilation system used to control the respiratory pattern of the lung and to deliver an arbitrary mixture of three different types of gases (^{3}He, O_2 and air) at any desired ratio, volume and rate. The first dead space component, namely *dynamic dead volume*, V_D, contains the major conductive airways (trachea and main bronchi) and the portion of the ventilator system after the respirator valve, including endotracheal tube. V_D experiences a bi-directional flow of gas during respiration.

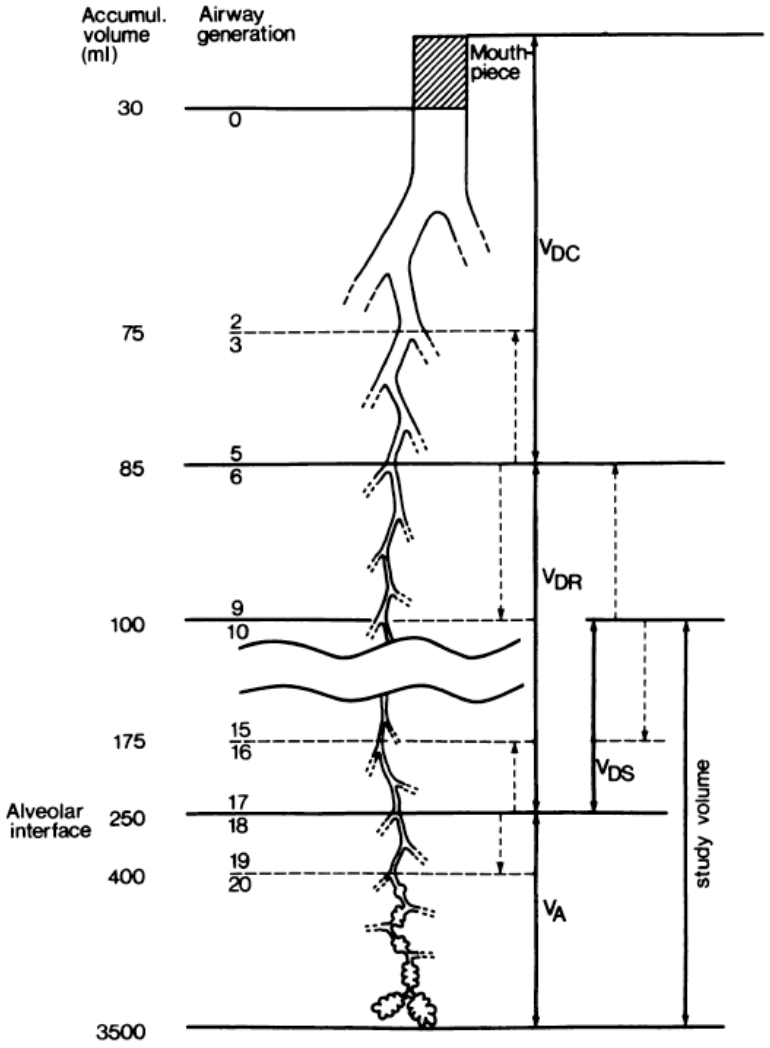

Figure 3.3. Partitioning of the lung in common dead space (V_{DC}), regional dead space (V_{DR}) and alveolar gas volume (V_A). The study volume comprises V_A and part of the regional dead space (V_{DS}) [26].

Respiratory gas travels towards the lung during inspiration through V_D, and away from that during expiration. The second compartment contains part of the ventilator system that only carries the source gas (i.e. ^{3}He) towards the respirator valve's inlet. This volume primarily contains the transmission line between the HP gas chamber and the respirator valve. Unidirectional transport of gas from the source through the transmission line will eventually fill up this dead space. Therefore, it is labeled the *static dead volume*, V_S.

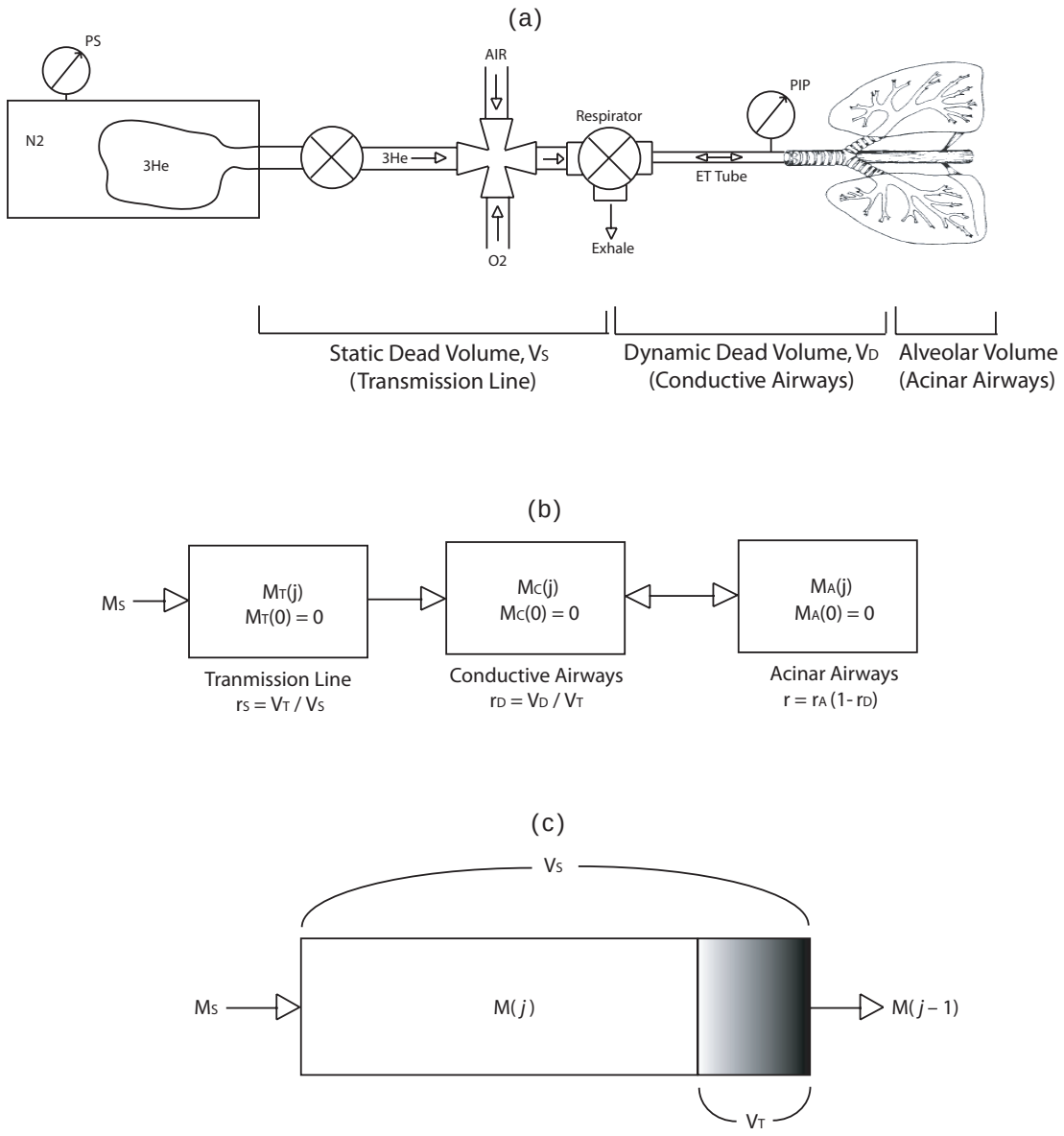

Figure 3.4. (a) Schematic diagram of the MR-compatible ventilator system depicting the static and dynamic dead space volumes; **(b)** three-compartment lumped model of ventilator system dead space volumes; and **(c)** the details of the gas replacement model in the static dead space compartment.

The primary difference between the dynamic and static dead volumes is that the portion of the respiratory gas residing in V_D from the previous breath is re-inhaled with each new breath. Therefore only a fraction of the freshly delivered gas to the lung actually arrives in the alveolar airways – the remaining fraction being made up of the exhaled gas in the previous breath. This phenomenon is known as *rebreathing* [27, 28]. The gas sitting in V_S

however, only travels towards the lung and this mixture becomes identical to the source gas after a finite number of breaths, and therefore is not subject to rebreathing.

A lumped three-compartment model is proposed as illustrated in Figure 3.4(b) to model the system dead volumes. The rightmost compartment comprises the acinar airways, including alveoli and small airways, containing the magnetization M_A. The middle compartment contains the major conductive airways and both the endotracheal tube and the respiratory valve that engage in the tidal respiration, containing the magnetization M_C. Finally the leftmost compartment includes the transmission line that carries the HP gas from the source (M_S) towards the inlet of the respiratory valve. The magnetization of the gas in the transmission line is referred to as M_T, and represents the magnetization of HP gas that enters the respirator valve with each breath.

For the serial ventilation sequence the magnetization buildup in the acinar airways is in principal governed by Equation [3.6], except that the source magnetization, M_S, is now replaced by the magnetization that arrives from the conductive airways at each breath:

$$M_A(j) = r_A \cdot M_C(j) + (1 - r_A) \cdot M_A(j-1) \cdot \exp\left[D_{RF} + D_{O_2}\right], \qquad M_A(0) = 0. \qquad [3.8]$$

At end-exhale the gas leaving the alveoli and small airways fills the conductive airways. Therefore the arriving magnetization from the conductive airways, M_C, at each breath is a combination of the arriving HP ^{3}He from the transmission line and the exhaled gas from the previous breath. The rebreathing fraction is a function of the dynamic dead space to tidal volume ratio, $r_D = V_D/V_T$. To ventilate the acinar airways the condition $r_D < 1$ has to be met, leading to:

$$M_C(j) = (1-r_D)\cdot M_T(j-1) + r_D \cdot M_A(j-1)\cdot \exp\left[D_{RF} + D_{O_2}\right], \qquad M_C(0) = 0. \qquad [3.9]$$

Substituting Equation [3.9] in Equation [3.8], the relation between the magnetization buildup in the acinar airways and the arriving magnetization from the conductive airways can be expressed as:

$$M_A(j) = r\cdot M_T(j-1) + (1-r)\cdot M_A(j-1)\cdot \exp\left[D_{RF} + D_{O_2}\right], \qquad [3.10]$$

where $r = r_A \cdot (1-r_D)$ is the *apparent fractional ventilation*, including the rebreathing effect of conductive airways.

At each breath, a tidal volume V_T of the source gas (with a nominal magnetization of M_S) is driven into the transmission line and mixes with the residual gas M_T, present in the static dead volume, V_S. Since the gas in the transportation line travels only in one direction towards the respiratory valve, it is assumed that the entrance of HP gas from the source pushes the same amount of gas (V_T) out of the static dead volume (Figure 3.4(c)). Defining $r_S = V_T/V_S$, the mixing of the arriving and residual gases in the static dead space can be recursively expressed as follows:

$$\begin{cases} r_S < 1: & M_T(j) = r_S \cdot M_S + (1-r_S)\cdot M_T(j-1), & M_T(0) = 0 \\ r_S > 1: & M_T(j) = M_S, & M_T(0) = (1-r_S^{-1})\cdot M_S \end{cases} \qquad [3.11]$$

Equation [3.11] is based on the assumption that the static dead space initially contains no HP gas, hence the stated initial conditions. This model depicts the relative significance of the static dead volume in lung ventilation. For a relatively small V_T compared to V_S ($r_S < 1$, e.g. in rodents and small animals), the concentration of the gas delivered from the transmission line M_T incrementally increases with each breath. However for large tidal volumes ($r_S > 1$, e.g. in humans and large animals), the entire contents of the static dead

space is purged with the first breath, and the magnetization of the following breaths will be identical to the source magnetization, M_S. It is important to note that no decay mechanisms are assumed to affect the accumulated HP gas in the transmission line since this volume is neither exposed to RF pulses nor the alveolar oxygen gas.

3.8. Closed form model

If the static dead space volume is much smaller than the delivered tidal volume ($r_S >> 1$, e.g. in humans and large animals), the magnetization of the delivered gas from the transmission line will be approximately equal to the source magnetization, $M_T \approx M_S$ at all times. Therefore Equation [3.10] becomes:

$$M_A(j) = r \cdot M_S + (1-r) \cdot M_A(j-1) \cdot \exp\left[D_{RF} + D_{O_2}\right], \qquad [3.12]$$

which after combining the recursive terms can be expressed in closed form as a geometric series:

$$M_A(j) = r \cdot M_S \sum_{i=0}^{j-1} q^i = r \cdot M_S \cdot \frac{1-q^j}{1-q} = M_\infty \cdot (1-q^j), \qquad [3.13]$$

where $q = (1-r) \cdot \eta$, with $\eta = \exp\left[D_{RF} + D_{O_2}\right]$, and $M_\infty = r \cdot M_S / (1-q)$ representing the steady state magnetization in the ROI as defined earlier. It is interesting to note that $M_A(1) = r \cdot M_S$ is the magnetization in the first image and therefore is related to the steady state magnetization as $M_A(1) = M_\infty \cdot (1-q)$. Normalizing Equation [3.13] with respect to $M_A(1)$ (obtained experimentally), the closed form equation can be expressed in terms of the normalized magnetization in the *j*-th image, $\hat{M}_A(j)$, as follows:

$$\hat{M}_A(j) = \frac{M_A(j)}{M_A(1)} = \frac{1-q^j}{1-q}, \qquad [3.14]$$

yielding a one-unknown equation in q with a finite search span of $q \in [0,\eta]$. The reliability of the solution however depends on the SNR in the first image – a function of $M_A(1)$, and the propagated uncertainty in the normalized magnetization sequence. However, the closed form solution provides the ability to perform a straightforward model uncertainty assessment with respect to model parameters.

3.9. Radiofrequency pulse decay model

Regional distribution of RF pulse flip angle, α, is typically measured by acquiring a series of n back-to-back images with imaging parameters identical to the ventilation imaging sequence and with no inter-scan time delay during a breath-hold. The RF-induced polarization decay of HP ^{3}He in this process can be described by:

$$M_A(j) = M_A(N) \cdot \exp\left[j \cdot N_{PE} \cdot \left(\ln(\cos\alpha) - \mathrm{TR}/T_{1,O_2} \right) \right], \qquad [3.15]$$

where $M_A(j)$ is the magnetization in acinar airways after acquiring j images in the final end-inspiratory breath-hold. N indicates the final image acquired in the preceding serial ventilation sequence. This calculation is based on the assumption that RF-induced depolarization is the dominant decay mechanism in the time scale of image acquisition compared to oxygen-induced decay; $T_{1,O_2} \to \infty$.

3.10. Ventilation time constant model

In the three-compartment model presented above, it was assumed that the arriving gas content from the conductive airways, with magnetization M_C, had completely arrived and uniformly mixed with the residual gas content in the acinar airways, leading to the resulting magnetization, M_A, before images are acquired. This assumption is fairly

reasonable if a long enough pre-acquisition time delay (PAD) is incorporated in the ventilation imaging pattern as shown in Figure 3.5. However, the choice of the PAD can have a significant impact on the measured *r* value. A too short time delay can potentially underestimate *r*, due to inadequate arrival and mixing of respiratory gas. A longer time delay provides a cushion against this effect, but promotes a more substantial signal decay in presence of oxygen, and also deviates the ventilatory pattern further away from the normal respiratory rate. The uniform mixing assumption may also be affected by the presence of obstructive lung diseases that cause elevated airway resistance.

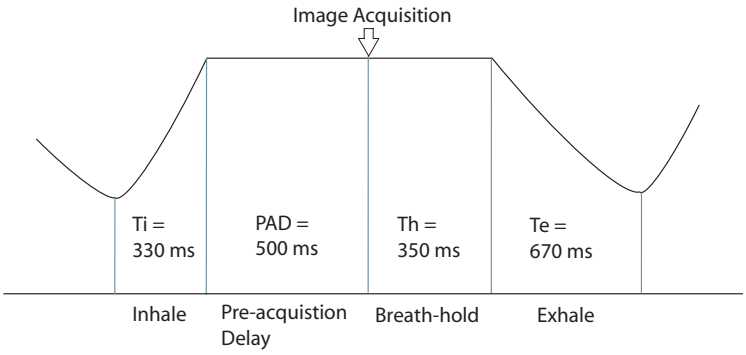

Figure 3.5. Timing diagram for a representative breath cycle with four time intervals. The numerical values are typical for rats.

In order to assess the transitional effect of respiratory gas arrival and mixing on fractional ventilation measurements, *r* can in general be defined as a function of time over the timescale of each breath. The magnetization build-up, described in Equation [3.10], then becomes:

$$M_{\mathrm{A}}(j,t) \;=\; r(t)\cdot M_{\mathrm{T}}(j-1,t) \;+\; [1-r(t)]\cdot M_{\mathrm{A}}(j-1,t)\cdot \exp\left[\mathrm{D}_{\mathrm{RF}} + \mathrm{D}_{\mathrm{O}_2}(t)\right] \quad [3.16]$$

$$r(t) \;=\; r_f\left[1-\exp\left(-t/T_r\right)\right], \qquad r(0)=0. \quad [3.17]$$

where $r(t)$ represents the progressively increasing fraction of fresh gas arriving in the airways with each breath. The fraction of fresh gas approaches the steady state (final) value r_f with the time constant of T_r. When the pre-acquisition delay is larger or of the same order of magnitude of T_r, the assumption of constant fractional ventilation holds:

$$r = \lim_{T_r < \mathrm{PAD}} r(t) = r_f \ . \qquad [3.18]$$

CHAPTER 4: Sensitivity Analysis

4.1. Introduction

Reliable measurement of fractional ventilation, based on dynamic signal models and ventilation imaging acquisition techniques described in Chapter 3, depends on a thorough understanding of sensitivity of the estimation model to the series of assumptions that are embedded in model parameters, measurement noise and choice of acquisition parameters. Subsequently, this information allows for the selection of optimal acquisition parameters to enhance the accuracy and robustness of ventilation estimation in the presence of noise and other experimental deviations.

4.2. Sensitivity to model parameters

The signal build-up in acinar airways was simulated for various model parameters using fixed values shown in Table 4.1 and initial conditions of Equations [3.7], [3.10] and [3.11]. The relative error, $\Delta r_A = \delta r_A / r_A$, was calculated as a measure of sensitivity of r_A estimation to the uncertainty in model parameters, and to the value of r_A itself. The model was constructed using *a priori* values for parameters (r_D, r_S, α, $P_S = P_AO_2$) and their respective variations shown in Table 4.1. An additional analysis was performed to evaluate model sensitivity to ignoring V_S by building the model using $r_S \in [0.1, 10]$ and solving for r_A by setting $r_S \rightarrow \infty$.

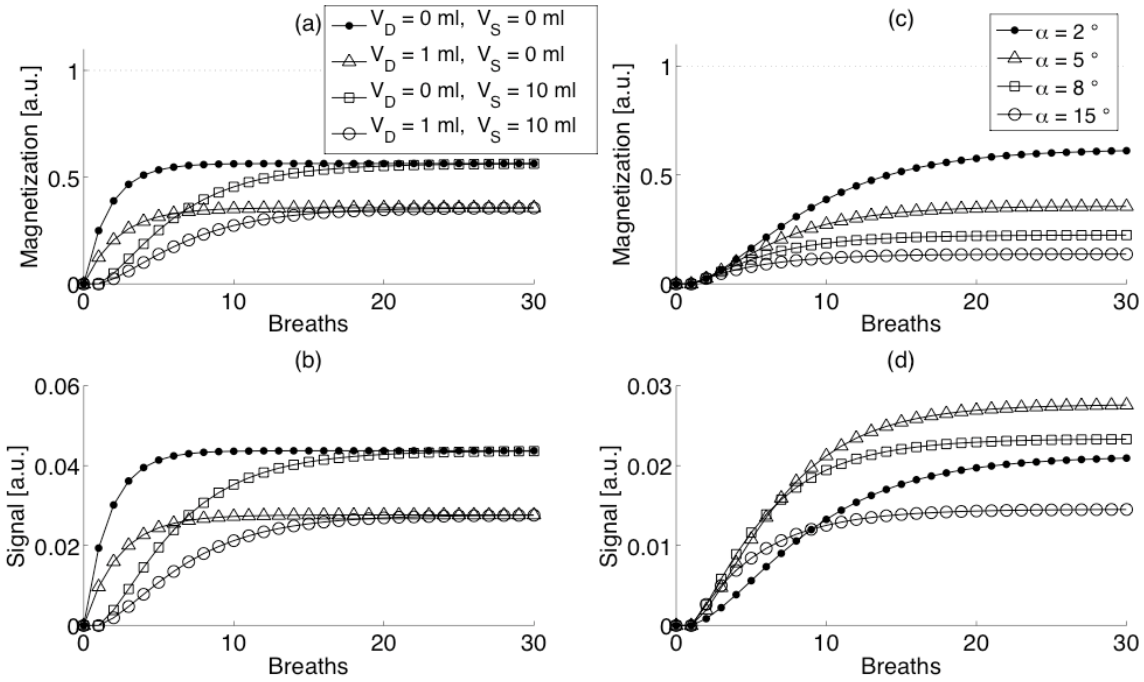

Figure 4.1. Simulation results for magnetization and signal buildup dynamics in the serial ventilation sequence with $\alpha = 5.0°$ in **(a)** and **(b)**, and $r_D = 0.3$ and $r_S = 0.3$ in **(c)** and **(d)**.

Figures 4.1(a) and 4.1(b) illustrate the effect of dead space on magnetization and signal build-up respectively. Introduction of the two types of dead space affects the magnetization and signal build-up characteristics of the ventilation system in very different ways. The addition of V_D to a no-dead-space system ($r_D = 0$ and $r_S = \infty$) is depicted as a lower steady state magnetization, M_∞, and a lower apparent fractional ventilation, $r = r_A \cdot (1 - r_D)$. Introduction of V_S to a no-dead-space system, on the other hand, increases the rise time of magnetization build-up curve. Nonetheless, this curve eventually reaches the same M_∞ as that of the no-dead-space system. Another important outcome of introducing the static dead volume (for $r_S < 1$) is that the magnetization in the first image vanishes as a result of delayed gas delivery through the transmission line. This behavior was embedded in Equation [3.10] through direct dependence of $M_A(j)$ on

$M_T(j-1)$. MR signal buildup behaves in a similar fashion to magnetization buildup for all these conditions (Figure 4.1(b)).

Table 4.1. Model parameters for simulation of sensitivity of fractional ventilation to model uncertainty, noise and number of images for the small animal model.

Fixed Model Parameters

Quantity	*Value*	*Units*
M_S	1	a.u.
N	30	breaths
τ	1.0	sec
N_{PE}	64	lines
P_S	140	mbar
V_T	2.0	mL
V_R	6.0	mL

Effect of Dead Space Volume

Quantity	*Value*	*Units*
V_D	0.0 or 1.0	mL
r_D	0.0 or 0.5	-
V_S	0.0 or 10.0	mL
r_S	∞ or 0.2	-

Dynamic Range

Quantity	*Value*	*Units*
α	0.0 – 90.0	deg
r_A	0 – 1	-

Nominal Model Parameters

Quantity	*Value*	*Units*
r_D	0.3	-
r_S	0.3	-
α	5.0	deg
$P_S = P_AO_2$	140	mbar
r_A	0.15 – 0.55	-

Sensitivity to Model Parameters

Quantity	*Value*	*Units*
r_D	0.0 – 0.9	-
r_S	0.0 – 0.9	-
α	3.0 – 7.0	deg
P_AO_2	0 – 200	mbar

Sensitivity to Noise and Number of Images

Quantity	*Value*	*Units*
SNR	5 – 60	-
N	3 – 10	images

Figures 4.1(c) and 4.1(d) demonstrate the effect of flip angle on magnetization and signal build-up respectively. Since a larger α implies a higher RF-induced depolarization of residual HP ^{3}He in the airways, the steady state magnetization in the airways, M_∞, is smaller compared to that of a smaller α. A larger flip angle however results in a greater MR signal for a given concentration of HP ^{3}He. Therefore the rise time of signal build-up and the steady state signal, S_∞, will be a nonlinear function of α history. For instance, α =

2° results in a larger steady state magnetization, due to accumulation of HP ^{3}He in the residual volume, compared to that of α = 5° (Figure 4.1(c)). The resulting steady state signal however will be larger for α = 5°, whereas α = 8° results in a faster rising airway signal than either of the former two cases, with a plateau signal falling between the two.

The relative error in r_A as a function of uncertainty in r_D is governed by $\Delta r_A = \delta r_A / r_A = \delta r_D$. Figure 4.2(a) illustrates a monotonic dependence of Δr_A on r_S variation. It is also evident that the relative error is larger for smaller r_A values. For instance an error of +0.05 in r_S results in 80% overestimation of r_A = 0.15, whereas it only affects r_A = 0.45 by 45%. The net result of entirely ignoring V_S is underestimation of the r_A value, again with a larger relative error for smaller fractional ventilation values. However as the actual r_S value grows beyond ~ 6 (e.g. in large species) the model quickly becomes less sensitive, as shown in Figure 4.2(b).

The sensitivity of the model to variations in the two primary decay mechanisms, α and P_AO_2, were assessed in a similar fashion. As shown in Figure 4.2(c) over/under-estimating the α value results in a monotonic over/under-estimation of r_A. Small r_A values are affected, to a larger extent, by α assumption. Using the same above example, overestimating α by one degree results in more than 80% overestimation of r_A = 0.15, whereas it only affects r_A = 0.45 by 20%. The effect of P_AO_2 value assumption is illustrated in Figure 4.2(d), showing a much smaller effect on relative error compared to α. For the same example, overestimating P_AO_2 at 200 mbar, results in about 4% underestimation of r_A = 0.15, whereas the effect on r_A = 0.45 is almost negligible.

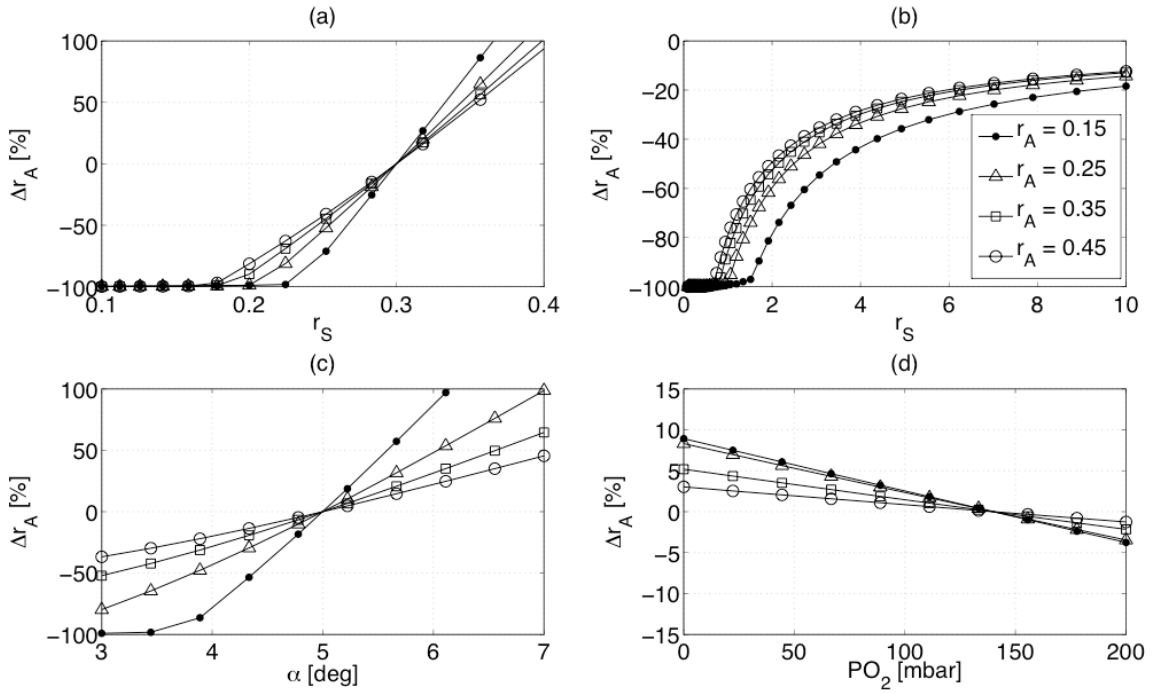

Figure 4.2. The sensitivity of the serial ventilation sequence in predicting airway fractional ventilation value (r_A) to model parameters, including **(a)** incorrect assumption of static dead space value; **(b)** ignoring static dead space; **(c)** incorrect assumption of flip angle value; and **(d)** incorrect assumption of oxygen tension.

Simulation and experimental results both indicate that inclusion of dead space volume in the ventilation model allows for a better fit to the data by providing additional degrees of freedom to the signal buildup model. As shown in simulations (Figure 4.1), in presence of static dead volume, the signal buildup curve starts resembling an *S*-shaped curve. In the absence of the static dead space model the signal buildup curve is mathematically incapable of exhibiting such a behavior and therefore adversely affects the estimation of r_A value. This model has a greater significance in small animals and rodents where the tidal volume is of the same order of magnitude as dynamic and static dead space volumes. On the other hand, it is important to note that inaccurate estimation of system dead volumes can lead to error in r_A calculation (Figure 4.2), and therefore it is necessary

to balance the tradeoff between the two factors through accurate measurement of system dead spaces.

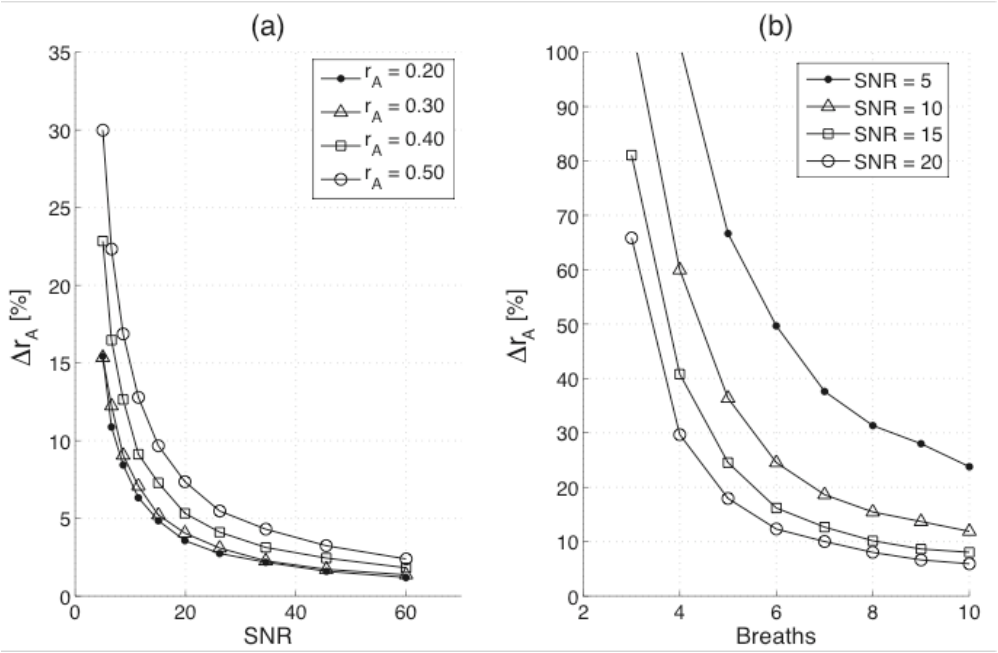

Figure 4.3. The sensitivity of the serial ventilation sequence in predicting airway fractional ventilation value (r_A) to **(a)** SNR in the first image, and **(b)** number of images included in the analysis.

4.3. Noise analysis and number of images

The accuracy of r_A estimation was also evaluated with respect to SNR of the second image with magnetization $M_A(2) = r \cdot r_S \cdot M_S$ ($r_S < 1$, given that $M_A(1) = 0$ for $M_T(0) = 0$) for the range of SNR values shown in Table 4.1. We note that a smaller quantity of HP gas arrives with one breath in poorly ventilated regions compared to normal regions. Therefore the reported SNR value reflects both the available polarization level and ventilation deficiency. Consequently, these regions are more "signal-demanding" than normal regions in regards to measurement accuracy. In consideration of the effects of ventilation deficiency, this measure of SNR provides a conservative assessment of sensitivity to noise. Noise was introduced in the noise-free simulated model by adding a normally distributed noise [29] to the second image with zero mean and a proper variance

to yield the desired SNR value. The same noise variance was then randomly added to all images in the sequence. Each noise level was simulated 1000 times to yield a statistically plausible result. Finally, a similar analysis was performed using a partial number of ventilation images to assess the robustness of the model to the number of included images in the presence of noise.

Figure 4.3(a) shows the evolution of Δr_A as a function of the SNR in the second image for different r_A values over 20 breaths. An SNR > 20 limits the relative error to 10% for all the selected r_A values between 0.15 and 0.55. However smaller r_A values, in general, show better robustness against added noise. For SNR < 10 the significance of Δr_A becomes large and undermines the reliability of measurements. In general including a larger number of images by using a larger quantity of gas (achieved for example by diluting the HP ^{3}He mixture with N_2 gas) can offset the SNR impact. Figure 4.3(b) shows the variation of Δr_A (for $r_A = 0.3$) with respect to the number of included images in the curve fit procedure for a given SNR < 20. Relative error in r_A drops exponentially with increasing number of images in the analysis, and shows a very similar performance for SNR ≥10. Similar characteristic curves can serve as a guide in designing the experiment in terms of available HP ^{3}He and polarization level. For instance the same level of Δr_A can be retained as SNR = 20 with 5 images, when acquiring 8 images at an SNR = 10.

The determining factor in the number of images acquirable in one session is the HP ^{3}He production capacity (1 L per day in authors' lab). This volume can provide several tens to hundreds of HP ^{3}He breaths in rodents and small animals but can be a limiting factor in

large animals and humans. Nevertheless, the gas mixture for large species can be diluted with ultra-high-purity N_2 gas to achieve larger quantities of imaging gas, provided that the polarization level of ^{3}He is adequate to meet the final magnetization necessary to perform the study as determined by the SNR requirements (Figure 4.3(b)).

4.4. Dynamic range of signal buildup

Regardless of the actual magnetization buildup in the airways, the apparent MRI signal observed at the end of each breath is a function of the applied flip angle α to acquire the image. As it was demonstrated by simulation in Figures 4.1(c) and 4.1(d), the flip angle value has a significant nonlinear effect on the rate of HP gas signal buildup in the airways. As evident by Equation [3.3], using a relatively small value for α (e.g. less than 1°) results in a diminished MR signal which in turn adversely affects the reliability of parameter estimation from the model. A relatively large value for α (e.g. larger than 10°) causes an excessive RF signal decay of the residual magnetization at each step (i.e. the $M_A(j\text{-}1)$ term in Equation [3.10]). This results in a significant decrease of signal buildup and makes it impractical to extract the fractional ventilation information from the sequence of images. Therefore α value needs to be selected such that both criteria are satisfied.

Signal buildup on the other hand is tightly related to r_A. Since r_A varies in different regions of the lung, and possibly among different subjects, it is fundamentally impossible to find a globally optimal α value to meet the SNR and signal buildup requirements for all conditions. In order to assess the effect of α on the dynamic range of signal buildup,

we define a simple cost function of the form $f = \max_{\alpha} \left[S_A(p) - S_A(1) \right]$ as a function of the number of breaths included in the analysis. In this function $S_A(p)$ represents the signal corresponding to 80% of steady state signal S_∞ in a given ROI, and p is the (nearest) breath number at which this 80% S_∞ signal is achieved. The underlying idea is to find the α value that maximizes the change in signal amplitude for a given number of images. Therefore, the α value that maximizes this cost function provides a conservative balance between the achievable SNR and the signal buildup dynamic range. Assuming that all system parameters are fixed, the p-th breath (corresponding to 80% S_∞ signal) can hold a different value for any given r_A, and therefore the corresponding flip angle value will be a function of r_A as discussed earlier. Simulations were performed using parameters in Table 4.1 to find the range of α values that maximize the signal dynamic range for a given number of breaths.

The combined effect of flip angle and number of images on maximizing the signal buildup range was assessed according to the proposed cost function f. Figure 4.4 shows the range of the estimated α values over a range of r_A as a function of the minimum number of breaths, p corresponding to 80% S_∞. The individual curves are slightly offset vertically to avoid masking each other. For any given number of breaths p, a range of α is returned which maximizes the cost function. This is due to the discrete nature of number of breaths, and therefore the largest α in each range can be selected as the candidate α for a given p. Note that this maximization criterion is inclusive in the sense that for any given r_A, the candidate α meets the requirement as well as for any larger r_A values. For

example, if the target number of breaths is 10, then $\alpha \approx 5°$ maximizes the dynamic range for $r_A > 0.1$, whereas an $\alpha_{opt} \approx 4°$ only meets the requirement for $r_A > 0.2$.

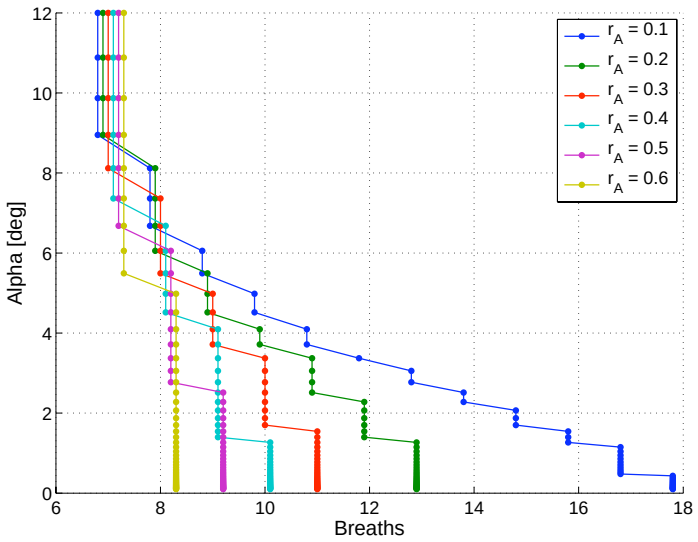

Figure 4.4. The estimation of flip angle value for serial ventilation imaging sequence to maximize the dynamic range of 80% of steady-state signal.

4.5. Comparison to large species

The signal build-up in acinar airways was simulated using Equations [3.7], [3.10] and [3.11] for a point object. The standard deviation of the estimated parameters (α and r) over many iterations was calculated as a measure of sensitivity of the respective parameter with to noise or other measurement uncertainties, i.e. $\Delta r = \sigma(r)$ and $\Delta\alpha = \sigma(\alpha)$. The model was constructed using *a priori* values for parameters, such as r_D, r_S, α, and $P_S = P_AO_2$ among others, shown in Table 4.2 over a range of Δr and α values. Analysis was performed to evaluate model sensitivity to noise, oxygen, number of RF pulses (N_{PE}), number of flip angle images (n). The effect of noise and oxygen were compared between pigs (3 slices per breath) and rats (1 slice per breath). Since any error in α propagates to r estimation process, all sensitivity analyses combined the two effects

in order to provide a more realistic measure of the coupled nature of this problem. If, at any given trial, the α estimation failed to converge, a random value was selected in the range of nominal flip angle ($\alpha_{\text{nominal}} \pm 2°$) and r was computed accordingly.

Table 4.2. Model parameters for comparing the sensitivity of r estimation model between small and large animals.

	Parameter	*Description*	*Units*	*Rat*	*Pig*
Species Comparison	NS	Number of slice	–	1	3
	MS	Matrix Size	–	64	48
	TR	Repetition time	ms	7	7
	PAD	Pre-acquisition delay	ms	500	500
	N	Ventilation image	–	10	7
	BR	Breathing rate	breaths/min	60	16
	FRC	Functional residual capacity	mL	4	800
	V_D	Dynamic dead space	mL	0.5	15
	V_S	Static dead space	mL	3.5	15
	I:E	Inhale-to-exhale ratio	–	1:2	
	V_T	Tidal volume	mL	FRC $\cdot$ r/(1−r)	
	P_S	Source oxygen concentration	mbar	140	

The effect of oxygen was assessed by assuming a nominal P_AO_2 value to hold in the airways. Signal buildup was then computed accordingly, and the noise-free model was used to estimate α and r values with the two common assumptions used in practice: P_AO_2 = 0 mbar for α estimation, and P_AO_2 = 140 mbar for r estimation, respectively. This procedure was performed over a range of N_{PE} values as an independent variable directly affecting the timing of ventilation sequence. For noise analysis, the estimation accuracy was evaluated with respect to SNR of the second image in the series with magnetization $M_A(2) = r \cdot r_S \cdot M_S$ ($r_S < 1$, given that $M_A(1) = 0$ for $M_T(0) = 0$). We note that in poorly ventilated regions a smaller quantity of HP gas arrives with one breath when compared to normal regions. Therefore, the reported SNR value reflects both the available polarization

level and ventilation deficiency. Consequently, these regions are more signal-demanding than normal areas in regards to measurement accuracy. In consideration of the effects of ventilation deficiency, this measure of SNR therefore provides a conservative assessment. Normally distributed noise [29] with zero mean and a proper variance was added to the second image to yield the desired SNR value. The same noise variance was then randomly added to all images in the sequence. Each noise level was simulated 1000 times to yield statistically plausible results. The standard deviation of successful trials corrected for sample size was then reported as the estimation error for the parameter of interest (i.e. α or r).

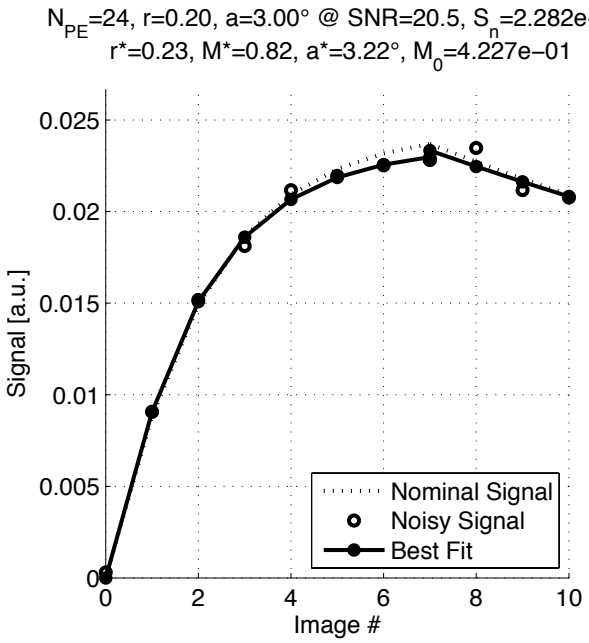

Figure 4.5. Simulated signal buildup for a representative voxel with nominal r = 0.2 and α = 3°. Image numbers 1 through 7 represent the signal buildup during the serial breathing of HP gas breaths, whereas image numbers during the sequential acquisition during the final breath-hold. The noisy datapoints are generated with a normal noise distribution corresponding to SNR = 20.5, and 24 RF pulses are assumed to be applied per image. Estimations for r and α (indicated with an asterisk) are shown on top of the panel.

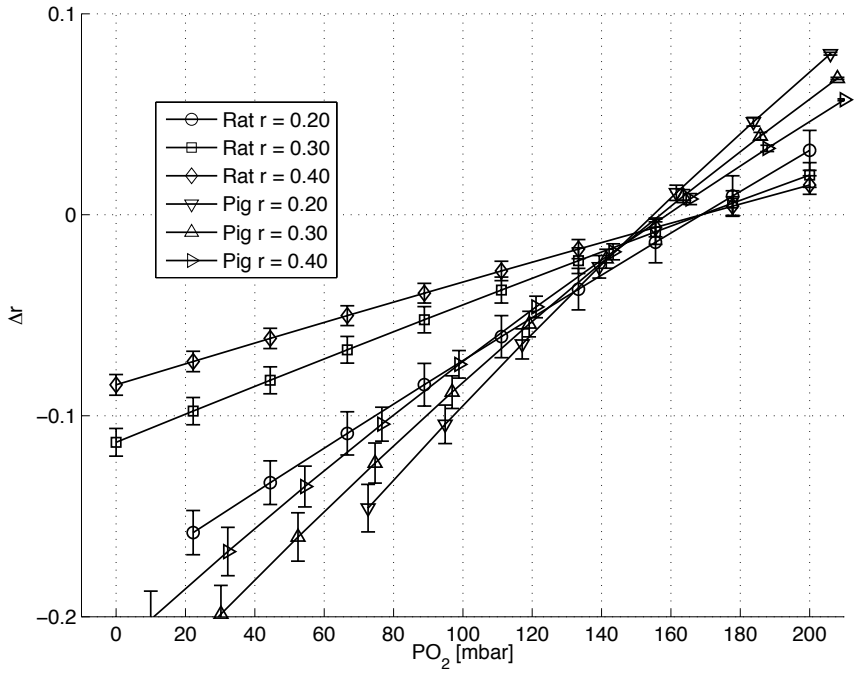

Figure 4.6. The systematic error in *r* estimation as a function of oxygen concentration misassumption in the airways in the absence of noise. A nominal PAO_2 = 140 mbar is assumed everywhere. The abscissa reflects the actual P_AO_2 which may be different from the nominal value. The error bars represent the error variation as a function of N_{PE} = 24–64 (practically invisible in rats). Other simulation parameters are shown in Table 1.

Figure 4.5 shows a representative combined *r* and α measurement experiment with noise added to the nominal signal with parameters typical to a pig study (Table 4.2). The best fit to the noisy data is also shown. The plateau signal of the ventilation sequence (N = 7) serves as the initial signal for the flip angle measurement sequence. In the absence of noise, the systematic error in *r* estimation as a function of oxygen concentration misassumption in the airways is shown in Figure 4.6. The actual P_AO_2 value is shown on the abscissa versus the nominal 140 mbar assumed everywhere, typical for acinar airways in healthy lungs. Data points corresponding to the same P_AO_2 values are slightly offset horizontally for better visibility. As shown, overestimating the P_AO_2 leads to an underestimated *r* value. The PO_2–induced error in pigs (with 16 BPM and NS = 3 per breath) is substantially larger than in rats (with 60 BPM and NS = 1 per breath), over *r* =

0.2–0.4. The error bars represent the Δr variation as a function of N_{PE} = 24–64. The effect of number of RF pulses on P_AO_2–induced error in rats is approximately half of the same quantity in pigs, for this particular set of parameters. Assuming a perfect knowledge of α, the error in r as a function of SNR in the second image of the ventilation sequence is shown in Figure 4.7, using N = 10 breaths. The r estimation accuracy in pigs is up to three times more sensitive to noise compared to rats. The error bars represent the Δr variation as a function of r = 0.1–0.5.

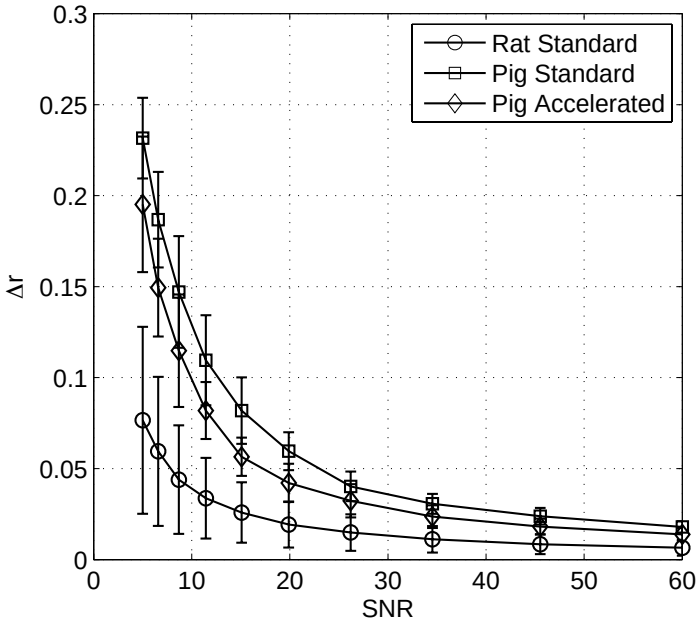

Figure 4.7. The relative error in r estimation as a function of SNR in the second image of the ventilation sequence, assuming a perfect knowledge of α.

The increased sensitivity to P_AO_2 misassumption largely stems from the 3–4 times slower breathing rate in pigs, which induces a larger oxygen-induced signal decay resulting in an overestimated α and an underestimated r value. The error was twice as large in pigs than in rats for a 50 mbar overestimation of P_AO_2 value. The mismatch between the actual P_AO_2 and the nominal 140 mbar value in the airways can be due to regional or time-

dependent variations of oxygen concentration, or lung diseases such as air trapping or gas exchange deficiencies, which affect the oxygen uptake rate and its, steady state value.

In addition to the systematic error associated with P_AO_2 misassumption, the larger effect of oxygen–induced signal decay, adversely affects the *r* estimation accuracy in presence of noise up to three times in pigs compared to rats, as shown in Figure 4.7. Reducing the RF pulses, N_{PE}, from 48 to 24 (i.e. through undersampling) however reduces this error by approximately 30%, limiting the average error to less than 0.05 with SNR > 20. For SNR < 10, *r* error (even with undersampling) approaches 0.1 which can severely undermine the reliability of measurements. As shown earlier [30], the relative error in *r* drops almost exponentially with an increased number of ventilation images, *N*. Including a larger number of images (achieved for instance by diluting the HP ^{3}He mixture with N_2 gas) can therefore offset the SNR impact, and can be used as a guideline for designing experiments depending on the total available quantity of HP gas and the polarization level.

Table 4.3. Model parameters for simultaneous sensitivity assessment of *r* and α estimation models and optimizing the α value.

	Parameter	*Description*	*Units*	*Value*
Sensitivity Analysis	*r*	Fractional ventilation	–	0.1 – 0.5
	P_AO_2	Alveolar partial pressure of oxygen	mbar	0 – 200
	N_{PE}	Number of phase encoding RF pulses	–	16 – 64
	α	Flip angle	deg	3 – 8
	SNR	Signal-to-noise ratio in image #2	–	5 – 60
	n	Number of flip angle images	–	2 – 10

4.6. Number of RF pulses

In addition to the noise effect, the coupled sensitivity of r and α was simultaneously assessed as a function of N_{PE}, the number of RF pulses per image, and n, the number of images acquired during the breath-hold at the tail end of the ventilation sequence, both in presence of noise. The optimal α value was then determined based on minimizing the uncertainty of r with N_{PE} and n as independent variables over the range of parameters listed in Table 4.3. Since the acquired signal intensity is in general a function of the number of applied RF pulses and magnitude of the flip angle, it was necessary to normalize the comparisons by determining the SNR value as a function of α and N_{PE} values. The available polarization in the airways was determined by fractional ventilation magnetization buildup. An arbitrary SNR value was then assigned to a nominal set of parameters (α, r, n and N_{PE}), from which the corresponding noise variance was derived and added to the signal amplitude for all other cases as determined by Equation [3.3] for a point object.

A representative set of α sensitivity assessment as a function of number of images, n (acquired during the final breath-hold in the ventilation sequence) and RF pulses, N_{PE}, is shown in Figure 4.8 for a single voxel with SNR = 22. For small flip angles ($\alpha \sim 3^{o}$), the estimation accuracy improves almost uniformly with larger N_{PE} and n values. Larger flip angles ($\alpha \sim 6^{o}$), however, exhibit a different behavior. Increasing number of RF pulses ($N_{PE} > 40$ in this case) leads to a local minimum in estimation error as a function of number of images, beyond which acquiring more images adversely affects the α accuracy. For smaller number of images ($n \leq 5$), α accuracy is always better for larger α

values. Acquiring more than 6 images however only marginally improves α estimation accuracy.

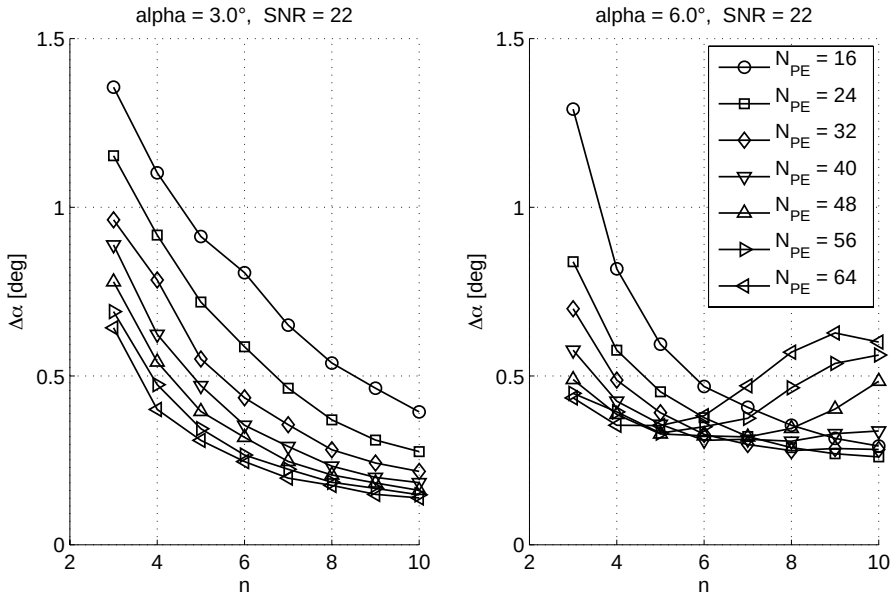

Figure 4.8. The relative error in α estimation as a function number of sequential images, *n*, acquired during an end-inspiratory breath-hold in the ventilation sequence, for a typical voxel with an initial SNR = 22. The line segments are drawn between datapoints to aid visualizing the trends.

The significance of α error is more objectively assessed in the context of its net effect on *r* estimation accuracy – the primary objective of the outlined measurements. Figure 4.9 demonstrates the tradeoff between α and *r* estimation error as a function of N_{PE} for a point object (for the specific case of $r = 0.2$ and $n = 4$), over the nominal range of $\alpha = 3$–8°. The SNR effect is implicitly incorporated in this analysis as a function of the applied α and polarization buildup driven by fractional ventilation. It is noted that, even though undersampling results in a less accurate estimation of α, it simultaneously reduces the contribution of flip angle to fractional signal buildup in the airways, mainly due to a decreased interaction of RF pulses with the HP gas in the respiratory gas. The accuracy of α estimation uniformly improves with increasing number of RF pulses, albeit at a smaller rate for higher flip angles. The α error becomes independent of N_{PE} for $\alpha > 6^{o}$ (settling

around 0.4º in this particular system). The overall estimation accuracy of *r*, on the other hand, improves approximately 1% per RF pulse (ranging over N_{PE} = 24–64) monotonically and independent of α value. The rate of change in *r* estimation error as a function of N_{PE} is fairly linear (R = 0.92–0.99), as shown in Figure 4.10.

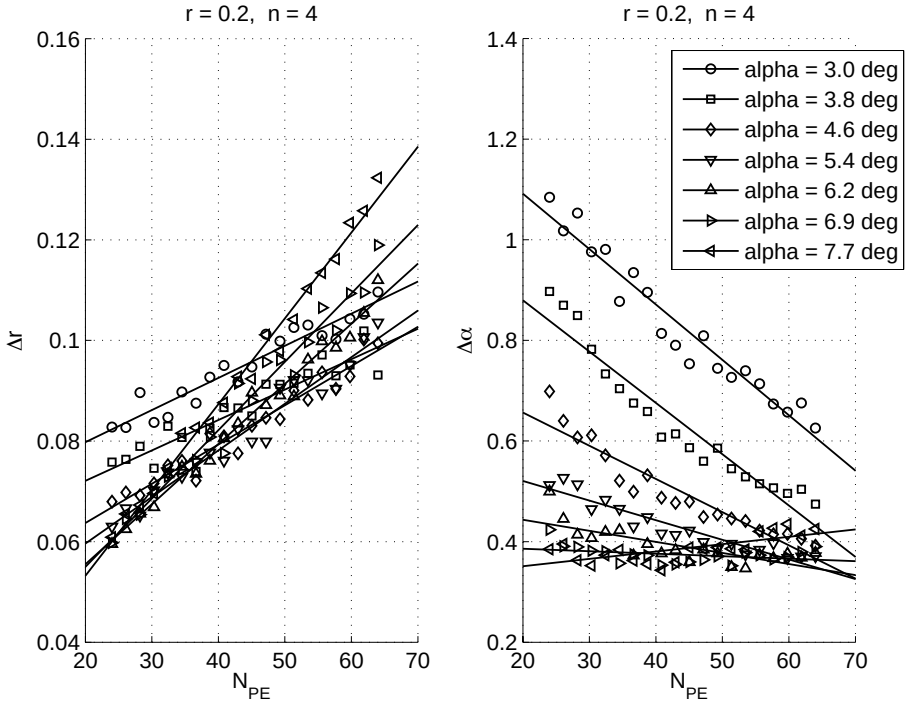

Figure 4.9. The relative error in *r* and α estimation as a function of number of RF pulses, N_{PE}. The SNR effect is implicitly incorporated in this analysis as a function of the applied α and polarization buildup as a result of the fractional ventilation (*r* = 0.2 in this case).

When performing measurements of α using a series of *n* back-to-back images during a single breath-hold, the accuracy uniformly improves for small flip angles ($\alpha \leq$ 3~4º) with larger N_{PE} and *n*. This error for large flip angles ($\alpha \geq$ 6 ~ 7º) however with increasing number of RF pulses (N_{PE} > 40 as shown in Figure 4.8) leads to a local minimum as a function of number of images, beyond which acquiring more images adversely affects the α accuracy. This effect is primarily because the larger flip angle depolarizes the available

magnetization at a faster rate and therefore adding more data points only deteriorates the fit quality. α accuracy is always better for larger α values when using a small number of images ($n \leq 5$) due to a more pronounced decay for the same number of RF pulses. Apart from this observation, lower SNR can in general be compensated by a larger N_{PE} or n (not shown for brevity), or any combination of the two parameters depending on the time requirements of the study. Acquiring more than 6 images however only marginally improves α estimation accuracy. Therefore, the final breath-hold need not be more than what is typically used in other breath-hold imaging techniques, e.g. 10–12 sec for P_AO_2 imaging [31, 32], and is expected to be tolerable by most individuals with severe lung diseases.

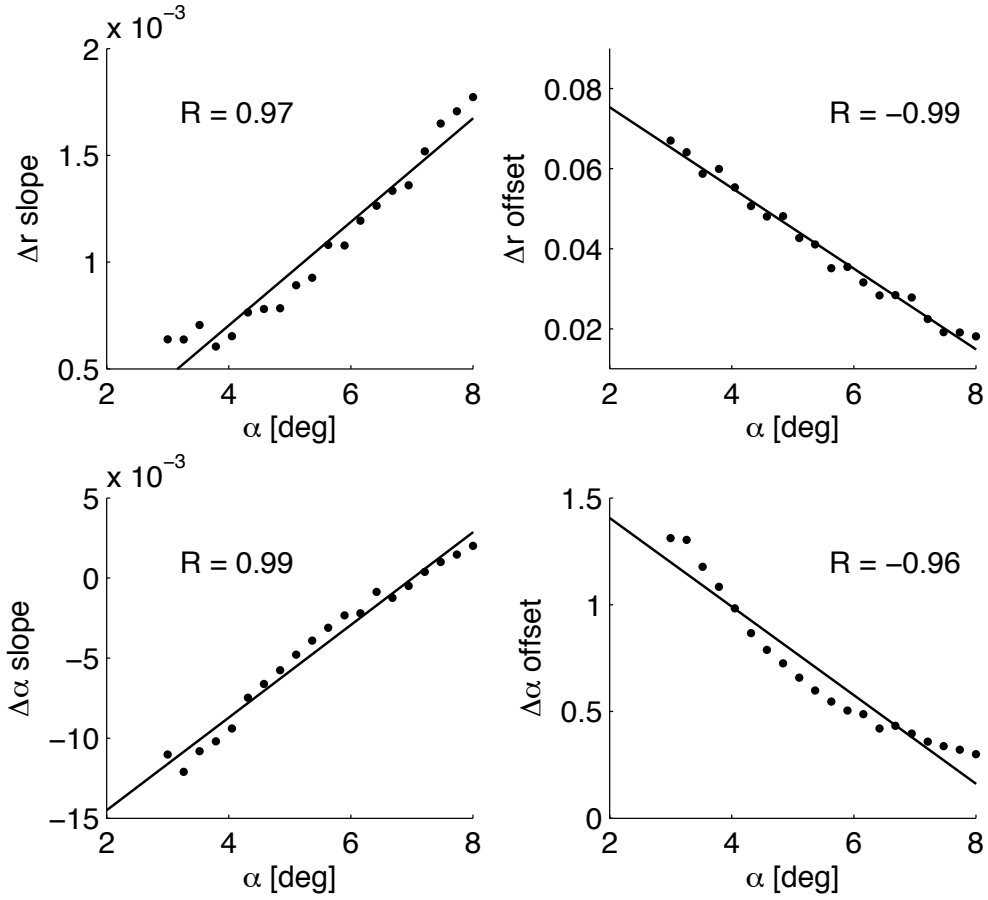

Figure 4.10. The rate of change in r and α estimation error as a function of N_{PE} over a range of flip angle values. The straight lines show the best linear fits for each α value.

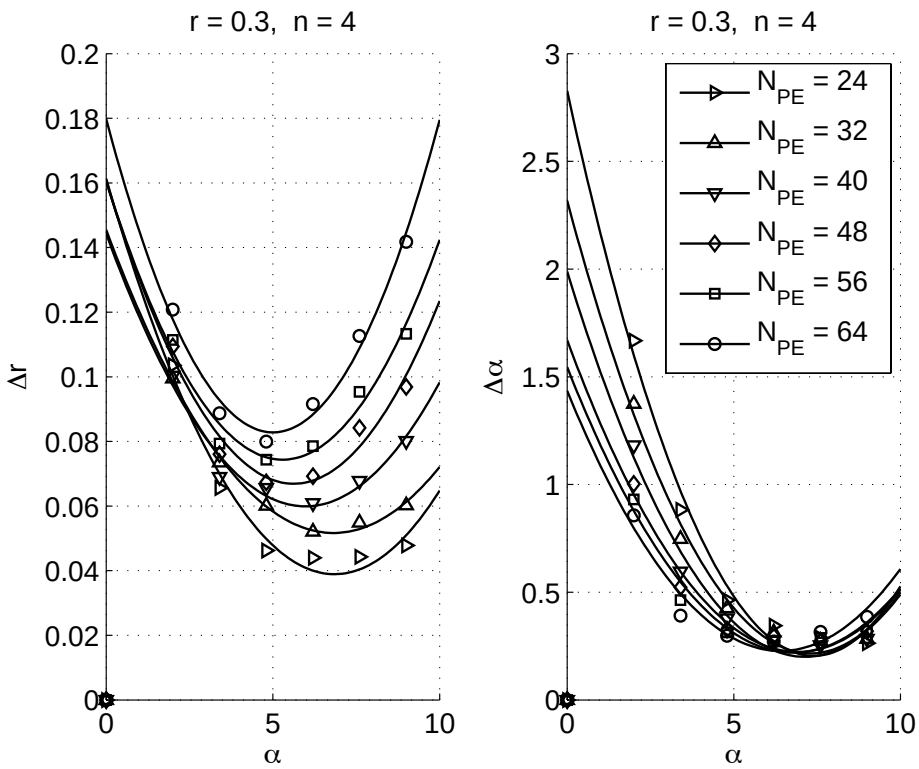

Figure 4.11. The relative error in r and α estimation as a function of the applied α value for a range of RF pulses to a point object. The SNR effect is implicitly incorporated in this analysis as a function of the applied α and polarization buildup as a result of the fractional ventilation (r = 0.3 in this case).

4.7. Optimality and tradeoffs

Finally, the estimation error in r as a function of the applied α value was used to determine the optimal flip angle over a range of N_{PE} = 24–64 for the same point object, as shown in Figure 4.11 (for the representative case of r = 0.3 and n = 4). For any given N_{PE}, there exists a finite neighborhood of α which leads to the best r estimation accuracy. This interval gets smaller for larger N_{PE} values as a result of a more pronounced effect of RF-induced depolarization. Variation of Δr versus α was fit to a second order function in order to assist in estimating the optimal flip angle, α_{opt}. Optimal flip angle shows a highly linear behavior with respect to N_{PE} (R = 0.98–0.99 for r = 0.1–0.3) as shown in Figure 4.12, and is confined to the range α_{opt} = 5–7° for N_{PE} = 24–64.

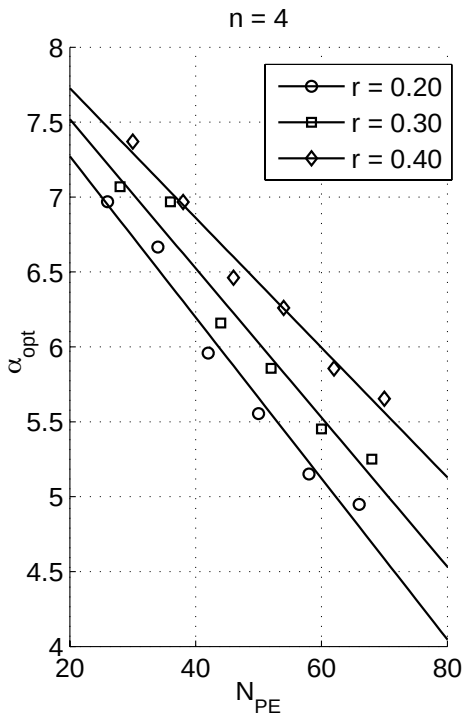

Figure 4.12. The optimal flip angle for *r* estimation shows a linear behavior as a function of N_{PE}.

Regardless of the actual magnetization buildup in the airways, the apparent MRI signal observed at the end of each breath is a function of the applied flip angle α used to acquire the images. As indicated by Equation [3.3], the flip angle value has a significant nonlinear effect on the rate of HP gas signal buildup in the airways. Using a too small flip angle (e.g. $\alpha \leq 1^{o}$) results in a diminished MR signal, which in turn adversely affects the reliability of parameter estimation from the model. A too large flip angle (e.g. $\alpha \geq 8^{o}$) causes an excessive RF signal decay of the residual magnetization at each step, $M_A(j\text{-}1)$ term in Equation [3.10]. This results in a significant decrease of signal buildup and makes it impractical to extract the fractional ventilation information from the sequence of images. Therefore, the α value has to be selected to balance the effect of these two processes and minimize the effective uncertainty in *r* estimation. Signal buildup, on the other hand, is tightly related to *r*, which in turn affects the choice of α. Since *r* varies in

different regions of the lung, and possibly among different subjects (due to ventilation defects and other pulmonary diseases), it is fundamentally impossible to find a globally optimal α value to meet the SNR and signal buildup requirements for all conditions. However, investigating the variation of optimal α can provide insight into its behavior as a function of various acquisition parameters and may serve as a guideline for proper selection of this acquisition parameter for a range of operating conditions.

Combined error analysis of r and α shows that in general the smaller number of RF pulses adversely affects the α estimation accuracy, but overall reduces the r estimation error, as shown in Figure 4.9, due to less contribution of RF pulse depolarization effect to ventilatory signal buildup and the associated α estimation error. The rate of change in r estimation error is fairly linear as a function of N_{PE}, as shown in Figure 4.10, and grows with larger flip angles due to the more substantial contribution of RF pulse decay per acquired image. The optimal flip angle value (α_{opt}) to minimize the r estimation error, is also a fairly linear function of N_{PE} trend, as shown in Figure 4.12, with no significant dependency on the r value. The analysis for the point object shows that α_{opt} is confined within ±0.5º of the optimal value over r = 0.2–0.4. This range of fractional ventilation is wide enough to cover the majority of a healthy lung parenchyma including acinar airways. In contrast to the single point object (lacking any particular geometry), it is evident that undersampling cannot indefinitely improve the r estimation accuracy. It is expected that there exists a limit beyond which the information loss due to undersampling (manifested in image reconstruction infidelity and associated artifacts) outweighs the gain

in reducing RF pulse effect and image acquisition time. This issue is discussed in the Chapter 6.

CHAPTER 5: Implementation in Phantom and Small Animals

5.1. Introduction

Before attempting to implement the proposed serial fractional ventilation imaging technique in large species, and especially humans, it is necessary to be evaluate its performance on phantoms and small animals. For this purpose an artificial lung phantom was used to validate the measurement accuracy. Moreover, measurement repeatability and its dependence on tidal volume were assessed in rat lungs. The consistency of fractional ventilation measurements using both cascade and serial techniques was also compared in lungs of healthy rats.

5.2. Mechanical ventilation

A high accuracy MRI-compatible mechanical ventilator (described in the Appendix) was utilized to perform the imaging experiments. This programmable ventilator is capable of mixing up to three different types of gases (e.g. ^{3}He, O_2, N_2 and air) at different ratios. The ventilator gas-handling unit is composed entirely of pneumatic and nonmagnetic delivery valves, placed in the proximity of the RF imaging coil as close as possible to the animal in order to minimize the dead spaces. A different valve setup – suitable for the desired flow rate – is used for each range of species. For the rat setup $V_D \approx 0.2$ ml (excluding the endotracheal tube), and $V_S \approx 3.2$ ml (between the ^{3}He chamber and the respirator valve), as illustrated in Figure 3.4(a). Placement of the HP ^{3}He chamber inside

the magnet bore near the RF imaging coil results in prolonged polarization relaxation times (45~60 min).

5.3. Animal preparation

All animal experiments were conducted in accordance with protocols approved by the Institutional Animal Care and Use Committee (IACUC) of the University of Pennsylvania. The proposed serial ventilation imaging sequence was prototyped in a healthy male Sprague-Dawley rats (300±50 g body weight). The rat was sedated with a 0.1 g/kg intraperitoneal ketamine and 10 mg/kg xylazine. The dose was repeated every 90 minutes or as necessary. Rat was then intubated with a 2-inch long, 14-gauge angiocatheter (BD, Franklin Lakes, NJ) modified with a sealant (UHU Tac adhesive putty; Saunders Mfg. Co., Readfield, ME) to create a tight seal around the entrance to the trachea, and was tested by ensuring a breath-hold of 25 cm H_2O for 5 seconds. Spontaneous respiration was then temporarily suppressed using 1 mg/kg intravenous administration of pancuronium bromide (Abbott Labs, North Chicago, IL) while under mechanical ventilation. Ventilation with air was maintained at V_T = 1 ml/100g body weight for the rat at 60 BPM. Heart rate and blood oxygen saturation level were monitored using a portable veterinary pulse-oximeter (Nonin Medical, Inc. Plymouth, MN) with the optical probe attached to the rat's paw. Temperature was monitored using a rectal probe (SA Instruments, Stony Brook, NY), and maintained at 37°C using a flow of warm air through the magnet bore.

5.4. Imaging techniques

The imaging helium gas (Spectra Gases, Branchburg, NJ) has a nominal concentration of 99.19% ^{3}He and 0.81% N_2. This mixture was hyperpolarized through spin exchange collisions with optically pumped rubidium (Rb) atoms, using a commercial polarizer (IGI.9600.He, GE Healthcare, Durham, NC), to a level of 30~35% over approximately 14~16 hours.

Imaging of the bag phantom was performed in a whole body 1.5-T MRI system (MAGNETOM Sonata, Siemens Medical Solutions USA, Malvern, PA) using a flexible 8-channel (2 × 4 phased array) chest coil (Stark Contrast, Erlangen, Germany) tuned to the nominal ^{3}He resonance frequency of 48.48 MHz, with an approximate imaging volume of 35 cm long and 27 cm ID. One coronal projection image was acquired using a 2D multi-slice gradient echo pulse sequence at a planar resolution of 3.75 × 3.75 mm^2 using the following parameters: FOV = 24 × 18 cm^2, α = 1.5~2°, matrix size (MS) = 64 × 48 pixels, TR = 7.0 ms, and TR = 3.3 ms. Accelerated imaging was achieved using standard GRAPPA with ACL = 16 and AR = 4, resulting in an effective acceleration factor of 2 (24 versus 48 phase encoding lines in the non-accelerated acquisition).

Imaging of the syringe phantom and the rat were performed on a 50-cm 4.7-T MRI scanner (Varian Inc., Palo Alto, CA) equipped with 12-cm 25 G/cm gradients and a quadrature 8-leg birdcage body coil with ID = 7 cm (Stark Contrast, Erlangen, Germany) tuned to the ^{3}He resonance frequency of 152.95 MHz. The animal was placed supine in the RF coil. All imaging was performed using a fast gradient echo pulse sequence with:

field of view (FOV) = 6 × 6 cm^2, slice thickness (ST) = 4 mm (projection for the syringe phantom), α = 4~5°, matrix size (MS) = 64 × 64 pixels, T_R = 6.6 ms, and T_E = 3.3 ms. The middle coronal slice was selected by performing preliminary scout ^{3}He images to determine position in the three major planes, assuring that the trachea was included in the middle slice. Pulse width calibration was performed on the loaded RF coil to estimate the applied flip angle.

Ventilation images were acquired using the serial ventilation sequence (Figure 3.1(a)) using N = 10 HP ^{3}He breaths during a 350-ms breath-hold at end-inhale of HP ^{3}He breaths. The concentration of the administered HP gas was controlled with the ventilator at ^{3}He:O_2 ≈ 4:1. Reproducibility studies in rat were performed using V_T = 3 ml, whereas for volume-dependency studies four different V_T values were used: 2, 3, 4 and 5 ml. For comparison one extra set of ventilation measurements were performed in the rat using the cascade ventilation sequence (Figure 3.1(b)) with the same number of HP ^{3}He and 30 normal air breaths before each cycle of HP gas breaths, in order to wash out the residual ^{3}He gas from the lung parenchyma and adequately oxygenate the animal. Both measurements were performed using pure ^{3}He.

Regional distribution of flip angle, α, was measured by acquiring a series of back-to-back images with identical imaging parameters to the ventilation imaging sequence and with no inter-scan time delay. In order to minimize coregistration errors between α and r maps in the rats, flip angle images were acquired at the tail end of the ventilation sequence while holding the last HP gas breath for approximately 5 sec, ensuring identical lung

position and inflation level with ventilation images. The RF-induced polarization decay of HP ^{3}He was then calculated by fitting the images to Equation [3.15]. Calculations were based on the assumption that RF-induced depolarization is the dominant decay mechanism in the time scale of image acquisition compared to oxygen-induced decay; $T_{1,O_2} \to \infty$. A total of n = 20 images were acquired in the bag phantom.

5.5. Data analysis

Data analysis was performed using custom MATLAB (Mathworks, Natick, MA) programs. Analysis was performed on a voxel-by-voxel basis at a planar isometric resolution of ~940 μm in rats. The signal in the acquired images was bias-corrected for the background noise [33] according to: $\hat{S} = \sqrt{S^2 - \sigma^2}$, with σ being the inherent noise in the MR image, calculated from: $\sigma = \overline{B}\sqrt{2/\pi}$, where $\overline{B}$ is the average background signal intensity corresponding to a 10×10-pixel region far away from the lungs in the acquired image. Bins with an SNR below a certain threshold (varying between 3:1 and 7:1) were excluded from analysis. Time evolution of signal intensity of valid voxels were then fit simultaneously to Equations [3.3], [3.7], [3.10], and [3.11], yielding M_S and r_A as free parameters for each voxel. In reporting the mean fractional ventilation value, voxels with a near unity r_A value were excluded from the analysis, since they represent major conductive airways. The intrasubject reproducibility of fractional ventilation measurement was assessed by calculating intravoxel variation of the calculated r_A value across three consecutive measurements. The mean coefficient of variation $\hat{r}_A = \sigma(r_A)/\mu(r_A)$ was then calculated as a measure of reproducibility over the entire lung.

Pairwise comparison between different conditions was performed using a voxel-by-voxel linear regression analysis between the two r_A maps.

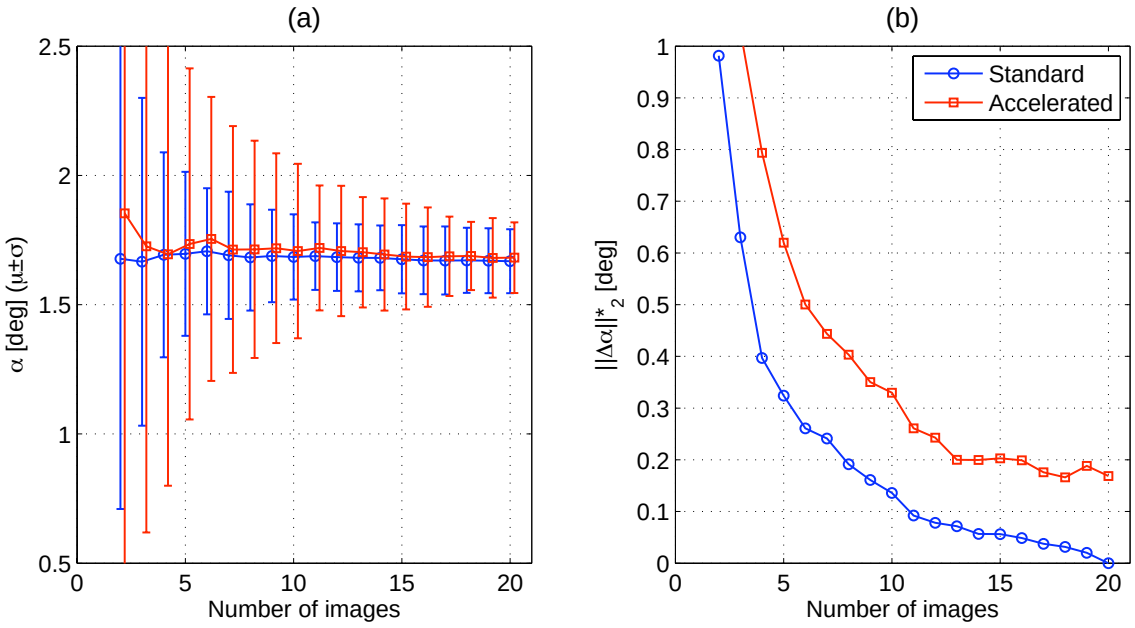

Figure 5.1. Demonstration of α estimation accuracy in a bag phantom using the fully sampled (standard) and undersampled (accelerated) acquisition schemes, as function of number of images, *n*. **(a)** Distribution of α in the bag phantom as a function of number of images included in the analysis becomes more homogenous and approaches a limiting mean and standard deviation value. **(b)** Variation of RMS error of α estimation over the entire phantom volume.

The distribution of flip angle in the phantom, $\mu(\alpha) \pm \sigma(\alpha)$, was calculated as a function of number of images used to solve for α. The α map corresponding to the maximum number of images (n = 20) was expected to have the highest estimation accuracy and therefore was used as the basis for comparison (α_{ref}) to other cases. For any given number of images used to calculate the flip angle map, the RMS error of α was calculated as $\hat{\alpha} = \|\Delta\alpha\|_2 = \|\alpha - \alpha_{\text{ref}}\|_2$, evaluated over all the valid voxels in the difference map. The coefficient of variation of flip angle was calculated on a voxel-by-voxel basis according to $c_v(x,y) = \sigma[\alpha(x,y)] / |\mu[\alpha(x,y)]|$, where $\mu(\cdot)$ and $\sigma(\cdot)$ represent the mean and standard

ventilation of α for (x,y) voxel over the n = 2 ~ 20 images, depicting the spatial sensitivity of α estimation to the number of utilized images.

5.6. Flip angle distribution in bag phantom

The flip angle phantom consisted of a 200-mL Tedlar plastic bag (Jensen Inert Products, Coral Springs, FL) filled with a HP gas mixture of ^{3}He:N_2 ≈ 1:4. Flip angle maps were measured in the phantom using both standard and accelerated acquisition schemes (described in 6.6) by acquiring a series of 20 back-to-back projection images. The size of the phantom was substantially smaller than the coil effective volume and was subsequently placed in the proximity of the coil isocenter. The B_1 field was therefore expected to be fairly homogeneous over the volume containing the phantom.

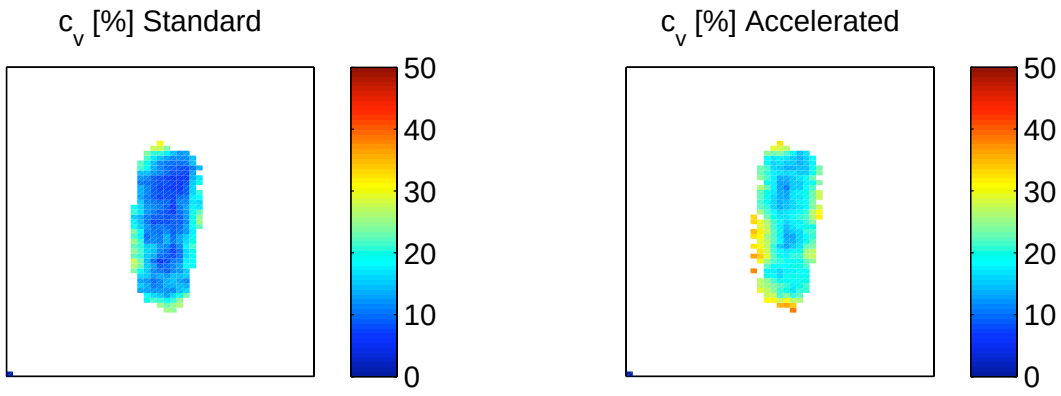

Figure 5.2. Coefficient of variation of α distribution in the imaged phantom using both acquisition techniques. The flip angle map corresponding to n = 20 using the standard method is used as the true distribution for error analysis.

Figure 5.1(a) shows the evolution of flip angle distribution in the bag phantom as a function of number of utilized images, n. The initial SNR in both standard and accelerated measurements exceeded 100:1. The standard acquisition technique converged

to an asymptotic mean α value (~1.7°) with as few as four images, whereas the accelerated technique required a minimum number of seven images to converge to the same quantity. The standard deviation of α measured by the standard method reached a steady state value of ~0.14° with no significant change for $n > 10$. The same quantity in the undersampled images remained twice as large for up to $n = 15$, beyond which no significant change in α dispersion was observed in the phantom. The RMS error of α declined monotonically as a function of n as shown in Figure 5.1(b), with the undersampled acquisitions exhibiting approximately a 90% larger error for $n = 5$, where the standard technique showed an RMS error of $\|\Delta\alpha\|_2 < 0.3^{o}$. The same error threshold was only reached by the undersampled acquisition with $n = 10$ images, in good agreement with simulation results in Figure 4.8. Maps of coefficient of variation of α for the standard and undersampled acquisitions are shown in Figures 5.2. Compatible with above observations, $c_v(\alpha)$ for fully sampled α map shows an overall lower value of ~12% compared to ~20% in the accelerated map. Spatially, the regions near the edge of the bag showed a larger $c_v(\alpha)$ compared to the interior points in both cases.

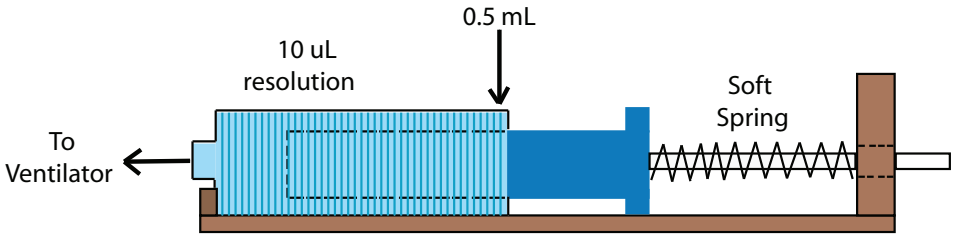

Figure 5.3. The artificial lung: spring-loaded glass syringe.

5.7. Ventilation validation in syringe phantom

The artificial lung phantom is comprised of a 10-ml Luer glass syringe (BD Yale, Franklin Lakes, NJ) with ID = 1.46 cm, loaded with a nonmagnetic beryllium-copper silver-coated compression spring (Small Parts, Miramar, FL) with a 3.24-in free length and a nominal spring rate of 0.145 lb/in (Figure 5.3). A stopper was mounted on the syringe holder base to block the plunger motion beyond a certain point, enforcing a residual volume of V_R = 4 ml during mechanical ventilation. For phantom validation studies the syringe-spring assembly was ventilated with three different tidal volumes; V_T = 1.1, 2.5 and 4.5 ml corresponding to $r_A = V_T/(V_T+V_R)$ = 0.22, 0.38 and 0.53 respectively. Dead space was directly measured as $V_D \approx 0.5$ ml and $V_S \approx 3.2$ ml.

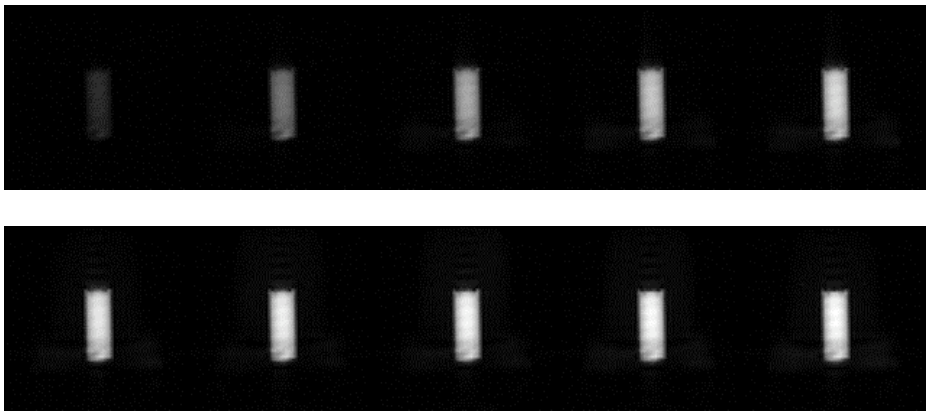

Figure 5.4. Representative serial fractional ventilation signal build-up images from the spring-loaded glass syringe.

Fractional ventilation was measured in the spring-syringe setup with three tidal volumes, V_T = 1.1, 2.5 and 4.5 ml (corresponding to r_A = 0.22, 0.38 and 0.53). A representative data set is shown in Figure 5.4. Each measurement was repeated three times. Since ^{3}He molecules can freely diffuse inside the syringe volume (D ≈ 2.0 cm^2/s), the region in the

image containing the syringe body was manually segmented and the sum of signal intensity for all the enclosed voxels were used as the representative signal value corresponding to each breath in the sequence. A typical SNR of 30~40 in the second image was achieved in the phantom. Figure 5.5 shows example MR images of the syringe displaced with the respective tidal volume, along with experimental datapoints and fit results. The individual points on each curve represent the average summed signal value for the three runs, and the error bars represent the standard deviation of this quantity. The results (reported on top of Figures 5.5(a) through 5.5(c)) show good agreement with *a priori* r_A values. In addition r_A value for each individual run was calculated and compared to the corresponding nominal r_A value. As shown in Figure 5.5(d), the measurements for each tidal volume also agree with the corresponding nominal r_A values.

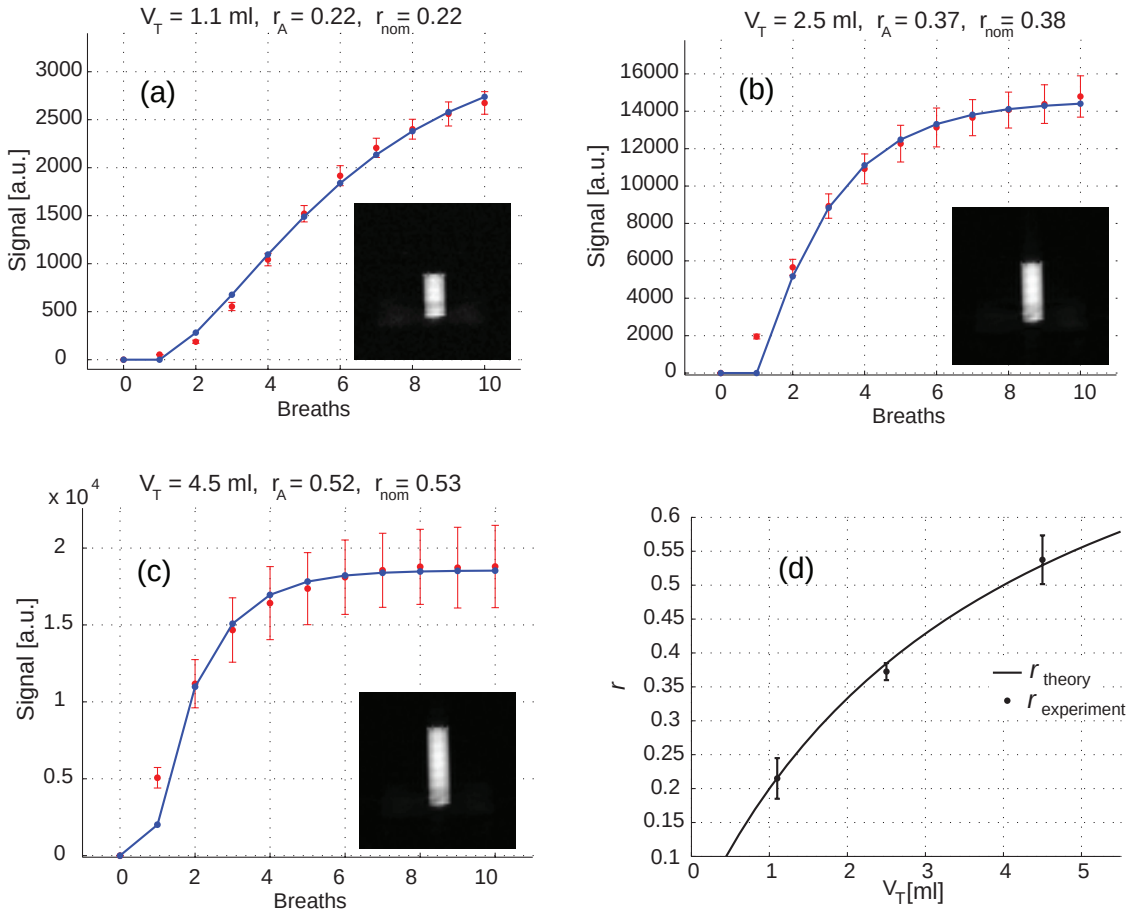

Figure 5.5. Signal buildup curves for the spring-syringe phantom for three different tidal volumes, along with the respective predicted fractional ventilation values. The error bars in **(a)** through **(c)** represent the standard deviation of signal for three sequential runs in each condition. Also shown are example MR images of the syringe at each tidal volume. Shown in **(d)** is the comparison of nominal values (solid line) to the estimated fractional ventilation values for each tidal volume. The error bars represent the standard deviation of the predicted fractional ventilation for the three trials.

5.8. Reproducibility and volume-dependency in rats

A representative set of ventilation images in the rat model is shown in Figure 5.6, depicting the signal buildup sequentially with increasing number of HP gas breaths. Note the large contrast between the conductive airways and lung parenchyma in the beginning of the sequence, indicating the high *r* value in the former compartment. Figure 5.7(a) shows the voxel-by-voxel $\hat{r}_{\mathrm{A},i} = \sigma(r_{\mathrm{A},i})/\mu(r_{\mathrm{A},i})$ across the three measurements, with an

average $\hat{r}_A$ = 8.9±8.0%. In addition the pairwise spatial correlation of each two sets of measurements were evaluated. Shown in Figure 5.7(b) is the voxel-by-voxel correlation assessment of the first and second measurements with a relatively linear regression coefficient of R^2 = 0.94. As evident from the scatter plot, the dispersion of datapoints becomes larger for higher r_A values.

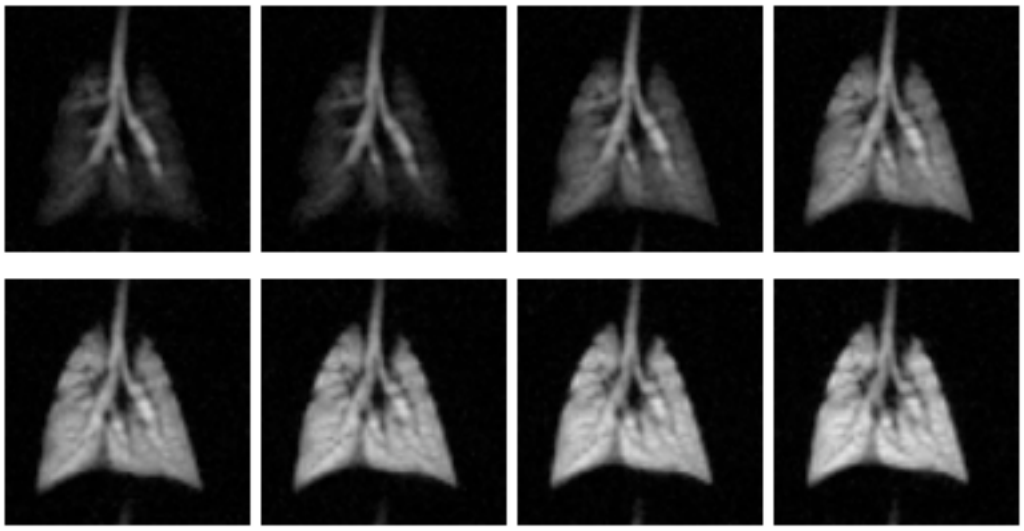

Figure 5.6. Representative serial fractional ventilation images from a healthy rat lung corresponding to 1 through 8 breaths of HP gas.

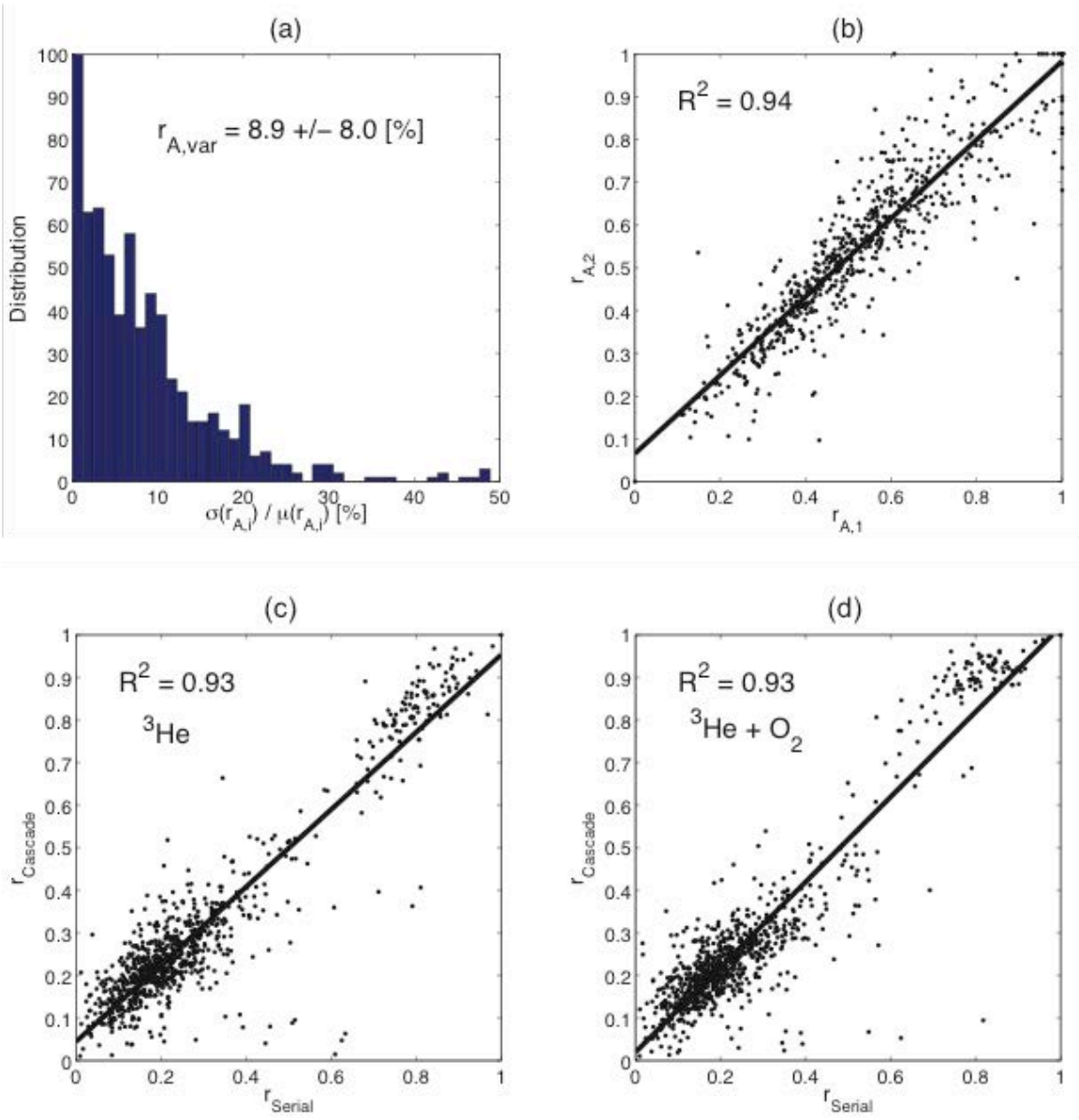

Figure 5.7. Assessment of regional reproducibility of measurements of fractional ventilation in a healthy rat lung. Shown are **(a)** the pixel-by-pixel variation of the estimated r_A values over three consecutive measurements, and **(b)** correlation analysis for two separate measurements. Comparison of the serial and cascade ventilation sequences for measuring r_A in a healthy rat lung are shown as a pixel-by-pixel correlation analysis for the two separate measurements **(c)** with and **(d)** without oxygen.

A larger tidal volume yields a distribution with an elevated mean r_A value. Figure 5.8 shows example MR images of the rat lung along with the corresponding r_A map and the distribution histogram. SNR values in the second images in the sequence varied between 15 and 25. For comparing r_A mean and standard deviation values in each measurement,

voxels with a near unity r_A value (corresponding to conductive airways) were excluded from the distribution and calculated as follows: 0.42±0.21, 0.49±0.16, 0.63±0.16, and 0.69±0.15 for the listed V_T values respectively. Histograms also move to the right with increasing tidal volumes. Fractional ventilation in regions closer to major bronchi increase to a larger degree with increased tidal volume, compared to distal regional of lung parenchyma.

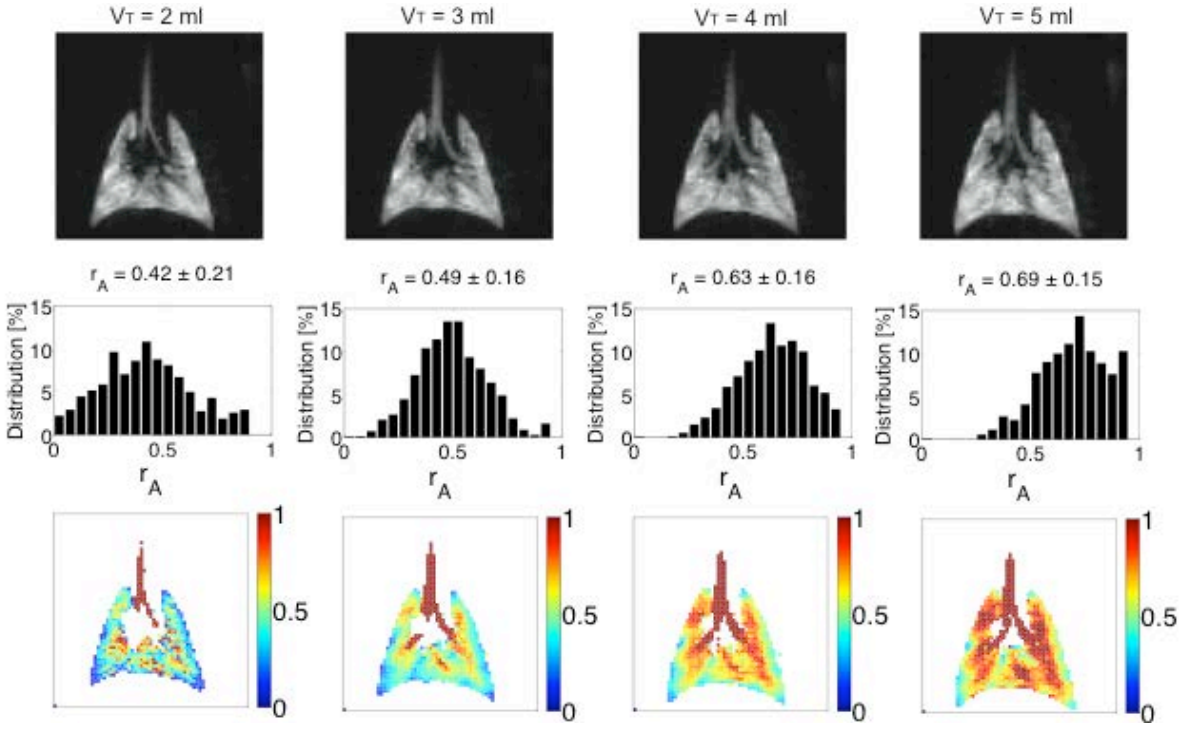

Figure 5.8. Volume-dependency of regional fractional ventilation in a healthy rat lung, for four different tidal volumes as shown on top of each map. The corresponding frequency distribution histograms are also shown.

The repeatability of *in vivo* measurements was assessed in a healthy rat lung with a voxel-by-voxel variation of less than 10%. In addition results were shown to tightly correlate (R^2 = 0.94) across different measurements. This level of precision is a function of highly reproducible tidal volume as controlled by the mechanical ventilator. In fact as

shown in Figure 5.8, the actual V_T value can have a drastic effect on the measured r_A value. This observation signifies the importance of normalizing and accurately titrating tidal volumes, especially when using this technique to compare different subjects and to noninvasively assess lung ventilation abnormalities.

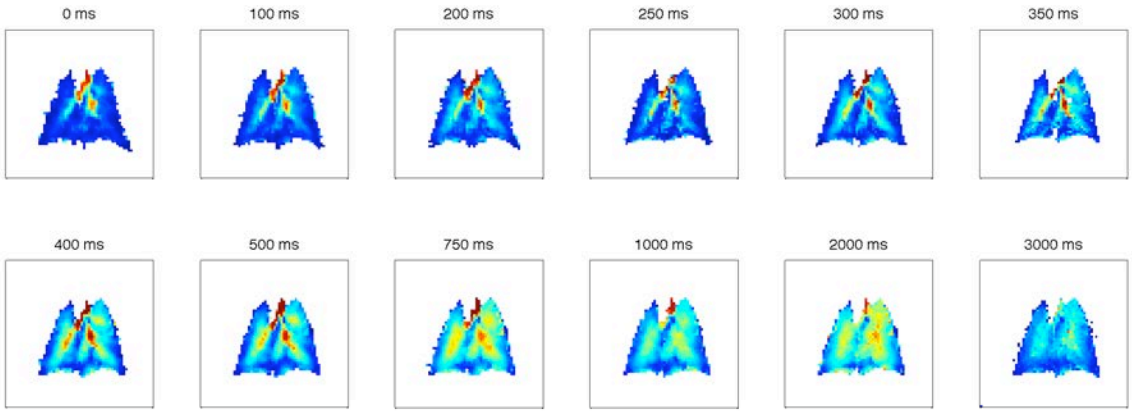

Figure 5.9. Maps of fractional ventilation in a rat lung acquired with varying pre-acquisition time delays. Each map is averaged over three staggered repeats.

5.9. Measurements of ventilation time constant

In order to assess the regional distribution of the fractional ventilation time constant T_r, r measurements were performed in the similar fashion described in 5.4 in rat lungs, with the only difference that PAD was varied in 12 unequal steps from 0 to 3 seconds, according to: PAD = 0, 100, 200, 250, 300, 350, 400, 500, 750, 1000, 2000 and 3000 msec. Measurements were performed in two rats (440 g body weight, V_T = 10 mL/kg), and repeated three times in each animal with staggered ordering in order to distribute the effect of $T_{1,EXT}$ across multiple measurements. Figure 5.9 shows the averaged r maps in one of the rats as a function of PAD value. The r maps from different time points were co-registered using a standard affine transformation by using the r map corresponding to PAD = 3000 sec as the reference image. This step was performed in order to correct for

any spatial mismatch caused by different inflation level corresponding to varying respiratory time points.

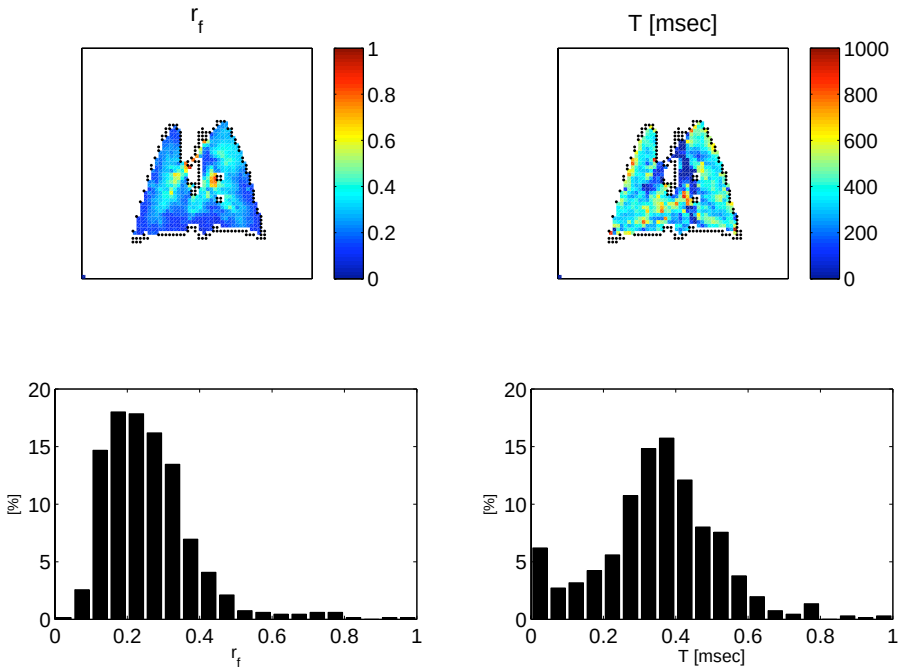

Figure 5.10. Measurements of regional fractional ventilation time constant in rat #1: $r_f = 0.26 \pm 0.13$, $T_r = 352 \pm 166$ msec

A the resulting maps of r_f (steady state r) and the corresponding ventilation time constant are shown in Figures 5.10 and 5.11 for each of the two rats, respectively. The corresponding values were as follows: $r_f = 0.26 \pm 0.13$, $T_r = 352 \pm 166$ msec in the first rat, and $r_f = 0.36 \pm 0.14$, $T_r = 416 \pm 191$ msec in the second rat. The black dots on these two diagrams represent the voxels that were enclosed in the lung but did not fit properly to the fractional ventilation time constant model, Equation [3.17]. Voxels enclosed in within conductive airways (including trachea and major bronchi) almost unanimously exhibit a near zero time constant which supports the relatively immediate gas transport process in these major airways. In contrast the majority of the voxels enclosed within the

lung parenchyma of both rats show a time constant around T_r = 400 msec, which is smaller than PAD = 500 msec time delay used in all described animal experiments above.

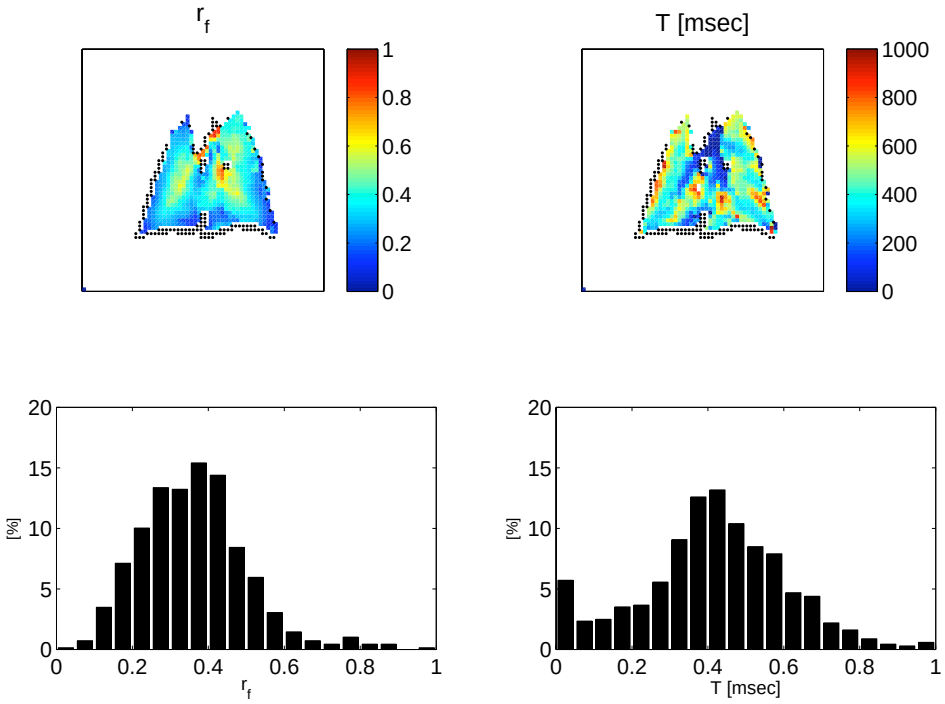

Figure 5.11. Measurements of regional fractional ventilation time constant in rat #2: r_f = 0.36 ± 0.14, T_r = 416 ± 191 msec

5.10. Technique comparison – pros and cons

Fractional ventilation measurement was also performed in the same rat using the cascade ventilation sequence at V_T = 3 ml. The required amount of time and HP ^{3}He gas to perform this measurement was 405 sec and 180 ml respectively (using a ^{3}He:O_2 = 4:1, 30 air breaths between each ^{3}He step, and two 10-breath normalization images at the beginning and at the end of the ventilation sequence), compared to 13 sec and 24 ml respectively, for the same measurement performed using serial ventilation sequence. Measurements were also performed using pure ^{3}He gas as proposed in the original work by Deninger *et al.* [23]. In accordance with this work, no dead space effects were considered in the analysis. Figures 5.7(c) and 5.7(d) show the voxel-by-voxel correlation

analysis of the two techniques. Results of the two methods are virtually identical as evident by linear regression coefficient $R^2 = 0.93$, and were the same for both gas mixtures. The scatter plots comprise two clusters, one grouped around $r_A = 0.8$ (corresponding to conductive airways) and a larger group spanning $0.0 < r_A < 0.4$ corresponding to acinar airways. We note that the lower r_A values in acinar airways compared to Figure 5.7(b) is primarily due to the underestimation of this quantity as a result of ignoring the dead space volumes.

In the cascade ventilation sequence, each point on the signal buildup curve for a given ROI is acquired separately. The *j*-th point is acquired during a breath-hold after inhaling *j* HP ^{3}He breaths, therefore requiring $\sum_{1}^{N} j$ HP ^{3}He breaths for *N* datapoints. In contrast, the serial ventilation sequence acquires an image at the end of each inhaled breath and therefore only requires *N* HP ^{3}He breaths for the same number of datapoints. The acquisition time of *N* images in the serial technique is approximately $N.\tau$; which is roughly a factor of *N* shorter than the cascade technique. These features are specifically desirable for performing the measurements on large species and humans where the total quantity of available HP ^{3}He per imaging session is typically a limiting factor. Even in rodents this benefit can be utilized for performing a higher number of acquisitions under different conditions, more slices, and a larger number of animals per imaging session. In addition the shorter acquisition time can benefit the physiological stability of the animal during the imaging session.

From a technical standpoint, due to its short acquisition time, the serial ventilation imaging sequence is practically independent of the external relaxation of HP ^{3}He in the reservoir. The external relaxation time constant, $T_{1,EXT}$, was shown [23] to have a profound effect on the cascade ventilation sequence signal buildup. On the other hand since images in the cascade ventilation sequence are acquired at separate breath-holds, the signal buildup model is independent of the regional α value, and therefore a larger α can be used to benefit from a higher SNR. In addition to the inherent cap on the maximum α value in the serial ventilation sequence, the inaccuracy in estimating α can adversely affect the r_A measurements, rendering the homogeneity of B_1 field an important factor. Utilization of a homogeneous RF coil (e.g. a volume birdcage coil versus a jacket coil) not only reduces the B_1 heterogeneity, but also allows for subject-independent mapping of the B_1 field, which can then be scaled for each specific loading condition using an overall RF pulse power calibration [34].

In serial ventilation sequence the lung oxygenation and image acquisition takes place simultaneously, and it is desirable to minimize the deviation from normal ventilation pattern. This is a less important concern in the cascade ventilation technique where the breath-hold occurs only once per each cycle of the ventilation sequence. Serial ventilation sequence adds a short breath-hold at the end of each HP ^{3}He breath (~350 ms in rats) for image acquisition. In practice it would be desirable to acquire multiple slices from the entire lung, especially in presence of a heterogeneous diseases such as emphysema. It will therefore be necessary to prolong the breath-hold to accommodate the additional number of slices. This change is most tolerable by large species with a relatively slower

breathing rate compared to image acquisition times. However in rodents and other small animals it may be necessary to acquire each slice in a different ventilation sequence or alternatively use fast acquisition schemes currently under development [35, 36].

CHAPTER 6: Implementation in Large Species and Humans

6.1. Introduction

Large animals provide a suitable platform for development, troubleshooting and optimization of the proposed fractional ventilation imaging technique with the eventual goal of translation to human subjects. This goal was achieved by implementing the methodology in pigs through the use of a dedicated HP gas mixing and delivery device and an accelerated MRI acquisition scheme. Imaging acceleration through undersampled reconstruction allows for the acquisition of a larger number of slices per breath without substantially deviating from a normal breathing pattern. Shorter breath-holds also diminish the oxygen-induced signal attenuation over the course of the study. The smaller number of RF pulses applied to acquire the same number of images reduces the irreversible effect of applied flip angle on respiratory gas signal buildup in the airways. The combination of these effects, in turn, can improve the estimation accuracy of regional fractional ventilation through better decoupling of the two signal components.

6.2. Rationale for acceleration

Large species, including human subjects, breathe over a respiratory time scale of a few seconds (the breathing cycle is approximately 4–8 sec while at rest). This is in contrast to rodents and other small animals that have a respiratory rate of up to 10 times faster than the larger mammals. The slower respiratory rate of these larger species means that certain

signal decay mechanisms are no longer negligible in ventilatory signal buildup. Most notably, the oxygen depolarization effect – with an *in vivo* relaxation time constant of around 18 sec – induces more prominent signal attenuation over experimental time scales of a few tens of seconds. This accelerated acquisition increases the sensitivity of *r* estimation to regional variations of P_AO_2, as shown in Figure 4.6. Accelerated acquisition shortens the breath-hold time necessary to acquire the images from the entire lung, thereby reducing the overall experimental time and the associated O2-inducde signal decay. Accelerated acquisition becomes more important when lengthier acquisitions are necessary to acquire a larger number of slices (with thinner slice thickness for instance) or when 3D acquisitions are desired in order to obtain higher resolution maps of ventilation abnormalities along the direction normal to slices.

The Generalized Auto-calibrating Partially Parallel Acquisition (GRAPPA) acceleration represents a fairly established undersampling and imaging reconstruction methodology through the use of phased array parallel MRI technology. Other fast acquisition schemes based on radial or spiral *k*-space scans have the potential be used for an even more effective acceleration, with or without parallel imaging capability. These methodologies have matured over the past few years and present great potential for fast respiratory gas imaging over the entire lung volume [36]. Reduced image acquisition time shortens the intermediate HP gas breath-hold time, thereby maintaining respiratory rate closer to normal breathing conditions. In addition to providing a more physiologically relevant ventilatory measurement, a more normal respiratory pattern can also assist in identifying

ventilation defects that may otherwise be masked by a slower breathing rate and longer breath-holds.

6.3. Animal preparation and mechanical ventilation

The multi-slice serial ventilation imaging technique was implemented on five healthy Yorkshire pigs (n = 5, 20–26 kg body weight). All animal experiments were conducted in accordance with protocols approved by the Institutional Animal Care and Use Committee (IACUC) of the University of Pennsylvania. Pigs were anesthetized with intravenous administration of 20–25 mg/kg ketamine and 4 mg/kg xylazine, intubated with a 6.5-mm cuffed endotracheal tube (Teleflex Medical - Rusch, Research Triangle Park, NC), and place inside the MRI scanner in supine position. A high accuracy MRI-compatible mechanical ventilator, prototyped in the authors' laboratory and capable of mixing up to three different types of gases (e.g. ^{3}He, O_2, N_2 and air) at different ratios, was used to perform the imaging experiments. The ventilator gas-handling unit (described in the Appendix) is composed entirely of pneumatic and nonmagnetic delivery valves placed in proximity to the RF imaging coil and as close as possible to the animal to minimize ventilatory dead spaces. For the pig valve setup: $V_D \approx 15$ mL (excluding the endotracheal tube), and $V_S \approx 15$ mL (between the ^{3}He chamber and the respirator valve). For normal breathing, animals were ventilated with air at V_T = 7–9 mL/kg, 14–18 breaths per minute (BPM), and inspiratory-to-expiratory ratio (I:E) = 1:2. Details of variation in ventilatory parameters are provided in Table 6.2. Since the anesthesia protocol was effective enough to suppress the spontaneous respiratory effort, use of a paralysis agent was not necessary. Heart rate and blood oxygen saturation level were monitored using a portable veterinary

pulse-oximeter (Nonin Medical, Inc. Plymouth, MN) with the optical probe attached to the pig's tongue. Body temperature was monitored using a hand-held rectal probe, and maintained at around 37°C using a hot water heating pad placed under the animal.

6.4. Imaging techniques

All imaging experiments were performed in a whole body 1.5-T MRI system (MAGNETOM Sonata, Siemens Medical Solutions USA, Malvern, PA) using a flexible 8-channel (2 × 4 phased array) chest coil (Stark Contrast, Erlangen, Germany) tuned to the nominal ^{3}He resonance frequency (48.48 MHz), with an approximate imaging volume of 35 cm long and 27 cm ID. Three ^{3}He coronal images (NS = 3) were acquired using a 2D multi-slice gradient echo pulse sequence at a planar resolution of 3.75 × 3.75 mm^2 using the following parameters: FOV = 24 × 18 cm^2, slice thickness (ST) = 30 mm, slice spacing = 6 mm, α = 3~4°, matrix size (MS) = 64 × 48 pixels, TR = 7.0 ms, and TE = 3.3 ms. The middle coronal slice was selected by performing preliminary scout ^{3}He images to determine position in the three major planes, assuring that the trachea was included in the middle slice. Proton images were acquired in an identical manner with the exception of: α = 20°, TR = 20.0 ms, and TE = 3.4 ms. Accelerated imaging was achieved using standard GRAPPA with ACL = 16 and AR = 4, resulting in an effective acceleration factor of 2 (24 versus 48 phase encoding lines in the non-accelerated acquisition).

Ventilation images were acquired using the multi-slice serial ventilation sequence, as shown in Figure 6.1, during an approximately 1.5-sec end-inspiratory breath-hold following each HP ^{3}He breath (N = 6). A 500-msec pre-acquisition delay was

incorporated before each image acquisition to allow for partial mixing of inhaled and residual gas compartments in the lungs. Breath hold was shortened to 1 sec (including the pre-acquisition delay) for the accelerated image acquisitions. For imaging, the concentration of the administered HP gas was controlled with the mechanical ventilator at $^3He:N_2:O_2 \approx 2:2:1$. A total amount of 2.0 L of HP gas mixture was prepared for each study by mixing 500 mL of ^3He, 400–500 mL of N_2 in one bag, and 240 mL of O_2 in a different bag and stored in custom-made gas delivery chambers inside the bore of the MRI scanner. The mixture was then delivered using the MR-compatible ventilator to the intubated animal. Placement of the HP ^3He chamber inside the magnet bore near the RF imaging coil resulted in prolonged polarization relaxation times $T_{1,EXT} \sim 25$ min. Each measurement of fractional ventilation was completed in approximately 1.5–2.0 min.

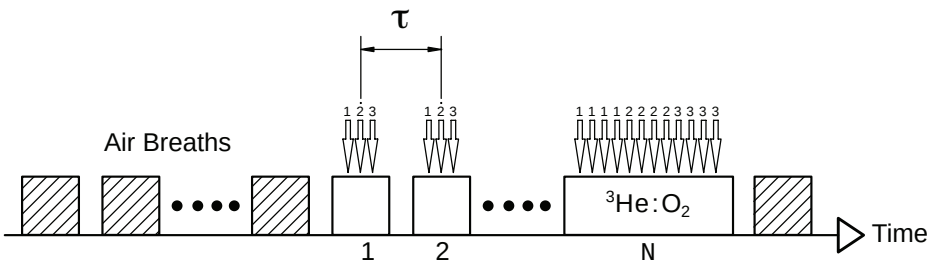

Figure 6.1 Multi-slice fractional ventilation imaging sequence. NS images are acquired during each end-inspiratory HP gas breath-hold covering the entire lung volume. A long breath-hold is performed after inhaling the last HP gas breath, during which the flip angle mapping imaging sequence is performed. Arrows indicate image acquisition. The dashed and blank boxes represent air and hyperpolarized gas breaths respectively.

6.5. Data analysis

Data analysis was performed using custom MATLAB (Mathworks, Natick, MA) programs developed in authors' laboratory. Analysis was performed on a voxel-by-voxel basis at a planar isometric resolution of 3.75 mm. The signal in the acquired images was bias-corrected for the background noise [33] according to: $\hat{S} = \sqrt{S^2 - \sigma^2}$, with σ being

the inherent noise in the MR image, calculated from: $\sigma = \overline{B}\sqrt{2/\pi}$, where $\overline{B}$ is the average background signal intensity corresponding to a 10×10-pixel region far away from the lungs in the acquired image. Voxels with an SNR below a certain threshold (varying between 3:1 and 5:1) were excluded from the analysis. The last image in the ventilation sequence ($j = N$, equivalent to the first image in the flip angle sequence) is typically expected to have the highest signal intensity and was therefore used as the basis for SNR threshold. In order to ensure a continuous B_1 map over the length scale of imaging voxels, the resulting α map was smoothed using a moving average filter by replacing each valid voxel's α value with the average α value among valid voxels in the surrounding 3×3 grid within each slice. This smoothed α map was then used to simultaneously fit Equations [3.3], [3.7], [3.10], and [3.11], yielding M_S and r as free parameters for each voxel. In reporting the mean fractional ventilation value, voxels with a near unity r value were excluded from the analysis, since they represent major conductive airways.

The intrasubject comparison of flip angle and fractional ventilation measurements in pig lungs using standard and accelerated acquisition techniques were performed through voxel-by-voxel linear regression analysis. The correlation coefficient of α and r maps for the two measurements were calculated in each animal. The flip angle maps acquired at tail end of the experiment were compared to the separately acquired α maps in a similar fashion.

6.6. GRAPPA image reconstruction

The Generalized Auto-calibrating Partially Parallel Acquisition (GRAPPA) is a fairly established and commonly available parallel image acquisition and reconstruction technique. Details of this technique are extensively described in published literature [37].

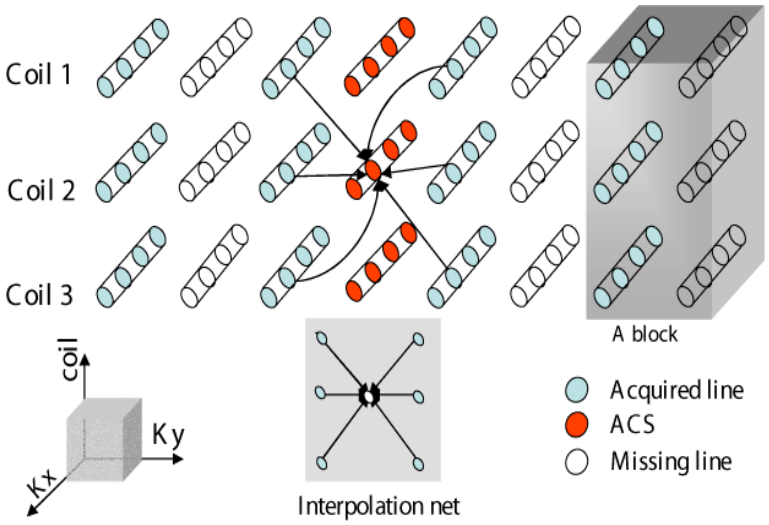

Figure 6.2. *k*-space trajectories and the interpolation net for GRAPPA in a 2-fold accelerated parallel imaging in 2D Cartesian MR imaging. As marked by the grey block, a *k*-space block is composed of one regularly acquired line (cyan circles) and the next AR−1 (the acceleration ratio AR = 2 in this example) consecutive missing lines (white circles) of each coil. The red circles indicate the additional acquired calibration lines (ACL) for estimating the interpolation weights [38].

Briefly, for an acceleration ratio of AR, each *k*-space block is defined as one acquired line plus the next AR−1 skipped lines, as shown in Figure 6.2. The data recovery for 2D GRAPPA is represented by an interpolation net in which the missing point is denoted as the root node, and leaf nodes are the nearest acquired neighboring points. The net structure and weighting factors are the same for each data point in the *i*-th missing line of each block ($1 \le i \le$ AR−1), and therefore only AR−1 nets are required for each component coil. The missing data can then be estimated based on a weighted sum of the

leaf nodes. The signal value at any given point in *k*-space for the *i*-th line in any given block as observed by coil *c* is described as:

$$S_c(k_x,\ k_y + i\cdot\Delta k_y) = \sum_{a=1}^{L}\sum_{b\in N_x}\sum_{h\in N_y} W_{c,i}(a,b,h)\cdot S_a(k_x + h\cdot\Delta k_x,\ k_y + b\cdot \mathrm{AR}\cdot\Delta k_y) \qquad [6.1]$$

where Δk_x and Δk_y represent the sampling intervals, and N_x and N_y are the neighborhood along k_x and k_y axes, respectively. L is the total number of coils in the array, and $W_{c,i}$ refers to the interpolation net weighting coefficients for the *i*-th net of coil *c*. The interpolation weighting coefficients are calculated by acquiring a number of auto-calibration lines (ACL) per image from the central section of the *k*-space.

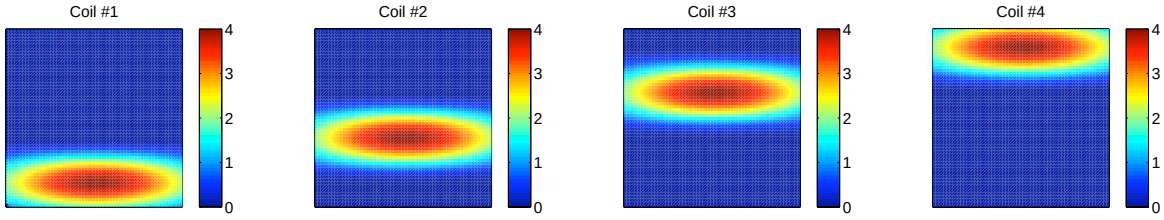

Figure 6.3. Coil sensitivity profiles of the four phased array channels used for simulating accelerated fractional ventilation imaging in a synthetic pig lung.

To assess the effect of GRAPPA image reconstruction of parallel undersampled data on *r* estimation accuracy, a representative 2D 64 × 64 image of the middle slice of a pig lung was used as the reference equilibrium spin density map, $M_S(x,y)$. The corresponding $r(x,y)$ map, derived from the same pig study, was used as the matching *a priori* fractional ventilation map. Using a uniform distribution of α = 5º and P_AO_2 = 140 mbar throughout the 2D slice, a series of synthetic spin density maps were generated corresponding to a multi-slice ventilation imaging experiment using the parameters shown in Table 4.2,

typical to a pig study, with $M_A(0) = 0$ throughout the lung. A Cartesian *k*-space acquisition scheme was then implemented on the constructed spin density maps, according to:

$$S_c(k_x,k_y) = \sum_{x=1}^{N_{PE}}\sum_{y=1}^{N_{PE}} M_A(x,y)\cdot B_c(x,y)\cdot \sin\alpha\cdot\cos^{k_x-1}\alpha\cdot \exp\left[-(k_x-1)\mathrm{TR}/T_{1,O_2}\right]\cdot\exp\left[j2\pi(k_x+k_y)/N_{PE}\right], \quad [6.2]$$

where TR is the scan repetition time and $B_c(x,y)$ represents the sensitivity profile for *c*-th coil. The last term represents the continuous phase encoding function, but in practice phase encoding was performed using a discrete FFT function for computational efficiency. Complex random noise was added to *k*-space signal to obtain the desired SNR value in image space. The spin density at each time point was sampled using a 1 × 4 phased array coil with identical sinusoidal sensitivity profile and uniformly positioned along the vertical axis of the lung, as shown in Figure 6.3. The accelerated (undersampled) acquisitions were performed using ACL = 8–32 and AR = 2–4, as shown in Figure 6.4, over the range of parameters shown in Table 6.1.

Table 6.1. The numerical values of imaging acceleration parameters used for simulation, sensitivity and optimization analysis.

	Parameter	*Description*	*Value*
GRAPPA Analysis	MS	Matrix size	64
	ACL	Number of auto-calibration lines	4–32
	AR	Acceleration (undersampling) ratio	2–5
	C	Number of phased array coils	4
	N	Ventilation image	6
	n	Number of flip angle images	4

Images from individual coils were separately reconstructed using the standard GRAPPA algorithm by solving Equation [6.1] for the weighting coefficients using the auto-

calibration lines, as shown in Figure 6.5. Magnitude images from the four channels were then summed to obtain a single image for the corresponding time point, as shown in Figure 6.6. The resulting series of images was then fit to the fractional ventilation model to yield maps of α and r in a similar fashion to real experimental data. Results were evaluated in two different ways: (*i*) the root mean square (RMS) difference between the estimated and reference r maps $\hat{r} = \|\Delta r\|_2 = \|r - r_{\text{ref}}\|_2$, where $\| \cdot \|_2$ denotes a 2-norm applied to all the valid voxels in the difference map; (*ii*) the correlation coefficient R for the voxel-by-voxel linear regression analysis between the estimated and reference r maps.

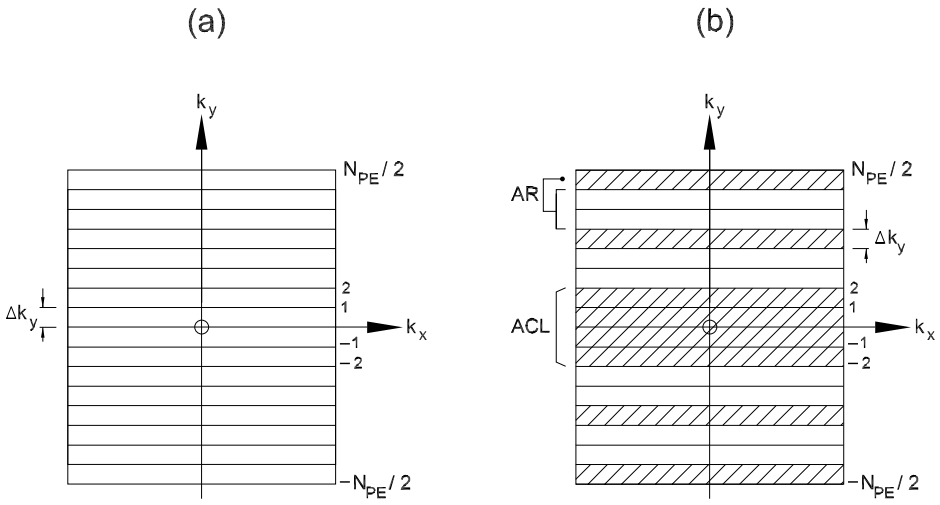

Figure 6.4. (a) Fully sampled (standard) *k*-space scan, versus **(b)** undersampled (accelerated) *k*-space scan using GRAPPA scheme.

The variation of RMS error in the computed 64 × 64 r maps is plotted in Figure 6.7 as a function of α, and for the range of acceleration parameters: ACL = 8–32 and AR = 2–4 using the 4-channel GRAPPA reconstruction. Each pair of ACL and AR parameters specifies a scan scheme consisting of N_{PE} = ACL + (64−ACL)/AR pulses, corresponding to an *effective* acceleration factor of 64/N_{PE}. A given acceleration factor however can be achieved using more than one combination of the (ACL,AR) pair, as demonstrated in

Figure 6.8, for this particular example. For comparison only the pair of parameters leading to the lowest error level was considered corresponding to any given N_{PE} value.

RMS *r* error was normalized with respect to the minimum error (i.e. the optimal undersampling condition) observed in the entire process, according to: $\|\Delta r\|_2 / \|\Delta r\|_{2,\min}$. Similar to the point object (Figure 4.11), the variation of $\|\Delta r\|_2$ versus α was fit to a second order function in order to assist in estimating the global minimum error associated to each undersampling scheme (ACL, AR). A similar assessment was performed on the voxel-by-voxel correlation coefficient, R, between the estimated and *a priori r* maps. Figure 6.7 shows that $\|\Delta r\|_2 / \|\Delta r\|_{2,\min}$ and R both reach a local minimum and maximum, as a function of α, respectively. In both cases the error bars represent the standard deviation of the error quantity over ~50 iterations. Based on the RMS error, the *r* estimation accuracy improves by increasing acceleration, compared to the baseline measurement (N_{PE} = 64 fully sampled). The error, however, reaches a global minimum around $N_{PE} \approx 31$, beyond which the trend reverses, as shown in Figure 6.9, and increases with further undersampling. The nominal optimal scan parameters for this representative case are: ACL = 24 and AR = 5, corresponding to an effective acceleration factor of ~2×. A similar behavior is observed in the correlation coefficient of the *r* maps, where a global maximum is reached around an effective acceleration factor of ~2×.

(a)

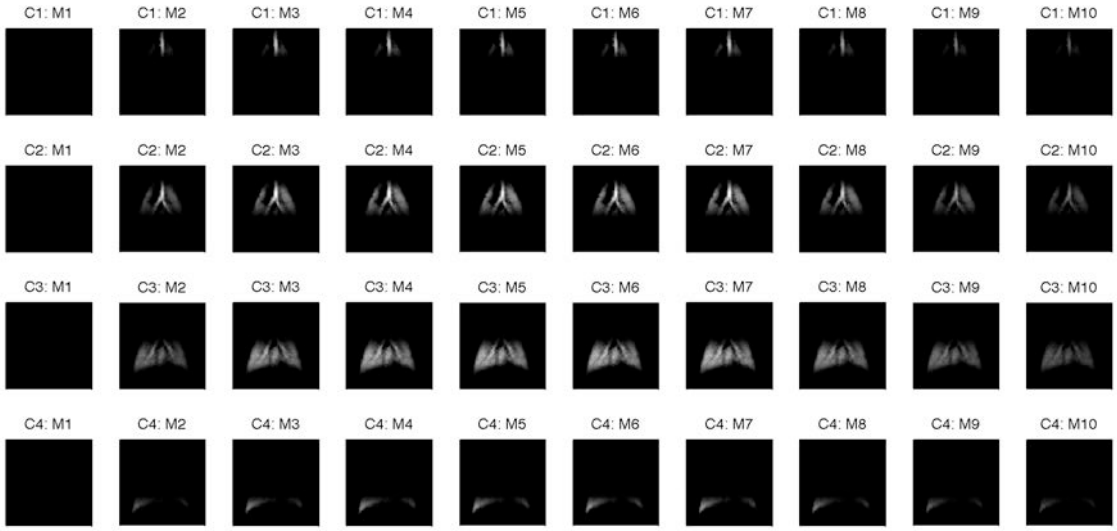

(b)

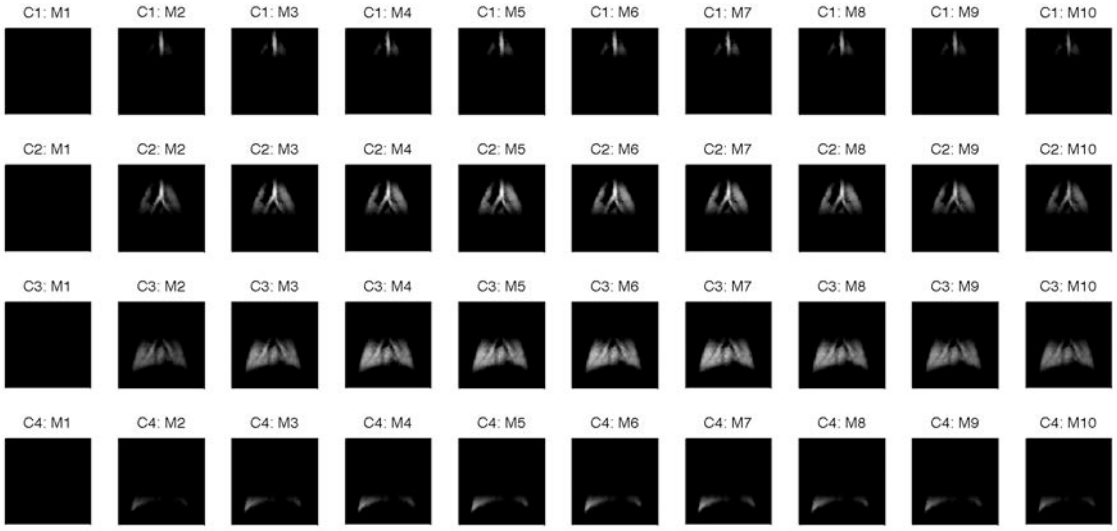

Figure 6.5. Individual images from each of the four channels used to create the signal evolution in the synthetic pig lung over the course of the simulated fractional ventilation imaging experiments: **(a)** fully sampled (standard) acquisition and reconstruction; **(b)** undersampled (accelerated) acquisition and GRAPPA reconstruction. The color scale is arbitrary and normalized across all images.

As pointed out earlier, any given pair of ACL and AR acceleration parameters correspond to N_{PE} = ACL + (64–ACL)/AR radio-frequency pulses, which in turn corresponds to an effective acceleration factor of 64/N_{PE}. In theory there exists more than one combination of (ACL, AR) parameters to achieve the desired acceleration ratio. In practice the largest ACL associated to a given N_{PE} will most likely minimize the estimation error by providing a good balance between image reconstruction quality and acquisition speed, as demonstrated in Figure 6.9.

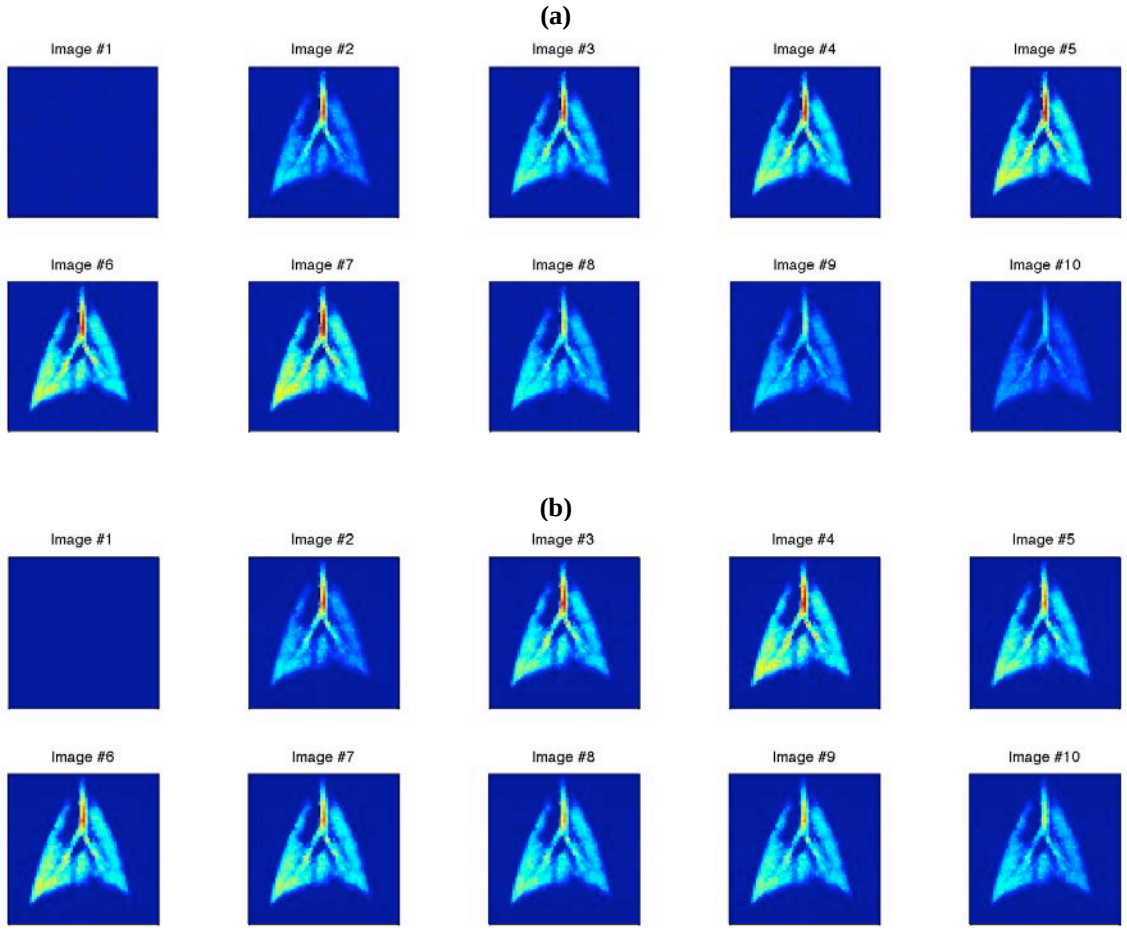

Figure 6.6. Combined images of signal intensity evolution in the synthetic pig lung over the course of the simulated fractional ventilation imaging experiments: **(a)** fully sampled (standard) acquisition and reconstruction; **(b)** undersampled (accelerated) acquisition and GRAPPA reconstruction. The color scale is arbitrary and normalized across all images.

The normalized RMS error ($\|\Delta r\|_2 / \|\Delta r\|_{2,\min}$), not only reflects the effect of number of RF pulses and noise on *r* accuracy, but also incorporates the inaccuracy introduced by image reconstruction artifacts as a result of excessive undersampling. Note that the minimum error point for each (ACL, AR) pair, as shown in Figure 6.7, also represents the optimal α (denoted as α_{opt}) for that given condition. The minimum error value indicates the limit beyond which the diminished effect of RF pulses is outweighed by information loss in image reconstruction. The error declines monotonically (R = 0.84) with acceleration towards the global minimum (ACL = 24 and AR = 5, corresponding to ~2× acceleration) and then increases almost linearly (R = 0.94) with further undersampling. The correlation coefficient between the estimated and *a priori r* maps behaves in a similar fashion and reaches a global maximum under the aforementioned conditions. The dependency of correlation coefficient on acceleration factor was approximated by a bi-exponential function, as shown in Figure 6.9. It should be emphasized that this analysis only pertains to this representative case. In general optimality conditions will be a function of several experimental details, including number of parallel coils, imaging resolution, and the achievable SNR.

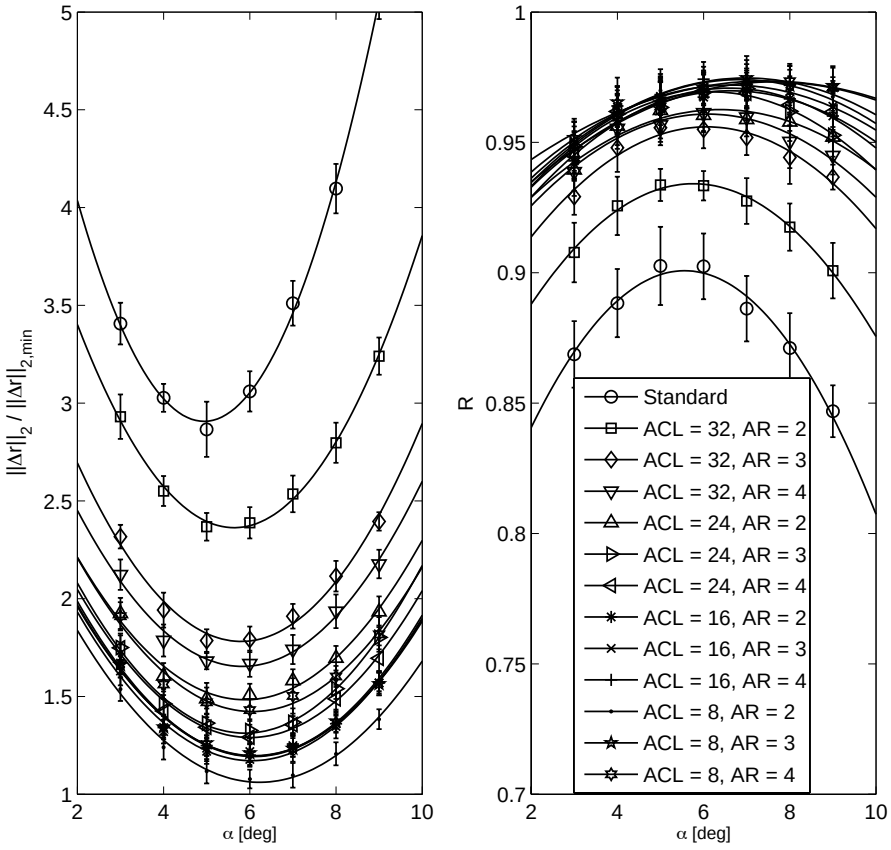

Figure 6.7. Accuracy of *r* estimation in a 64×64 2D synthetic images of pig lungs reconstructed with GRAPPA acceleration scheme using 4-channel parallel imaging, over the range of ACL = 16–32, and AR = 2–4. The RMS error of the estimated *r* map is normalized by the minimum error observed in the process. Error bars represent the standard deviation of RMS error over 100 iterations. The RMS error reflects not only the effect of RF pulses, but also the artifacts introduced by undersampled image reconstruction. **(b)** Variation of correlation coefficient between the estimated and the *a priori r* maps.

6.7. Measurement of fractional ventilation in pigs

Flip angle (α) maps were measured in the middle slice of five healthy pig lungs using both standard and accelerated techniques in separately from the ventilation sequence (i.e. *external* α measurement). Maps of standard and accelerated α maps in each animal were then correlated on a pixel-by-pixel basis. The smoothed α maps show a better spatial correlation (R = 0.62–0.96) between the two acquisition schemes, compared to the original maps (R = 0.26–0.83). α measurements in pig #4, shown in Figure 6.10, were done with the largest number of images in one breath-hold (n_{ext} = 20) subsequently

resulting in the highest correlation coefficient (R = 0.96) compared to other animals. Measurements of fractional ventilation were then performed using the multi-slice r–α imaging technique in all animals over three coronal slices. The *internal* flip angle maps were measured using n_{int} = 5 images during the tail end breath-hold of the ventilation sequence (with the exception of pig #1, n_{int} = 2).

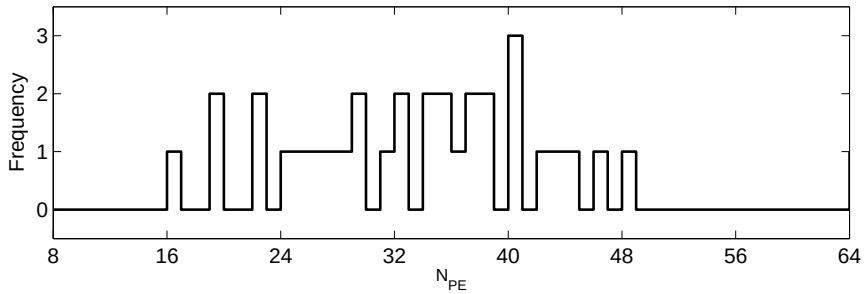

Figure 6.8. Multiplicity of number of RF pulses, N_{PE}, for the range of GRAPP acceleration parameters listed in Table 6.1.

A summary of r measurement results in the pigs are shown in Table 6.2 for each of the ventral, middle and dorsal slices. Middle slice r maps for the five healthy pig lungs are shown in Figure 6.11. Both standard and accelerated r maps are shown along with the corresponding voxel-by-voxel correlation graphs. The two measurements correlated (R = 0.83–0.89) in agreement with the synthetic pig lung GRAPPA simulation results shown in Figure 7. Pig #5 was an exception (R = 0.69), primarily due to the much lower than average SNR in the accelerated r measurement caused by a technical problem with the second batch of HP ^{3}He gas. Additionally, an unplanned animal care event made it necessary to reposition this pig inside the MRI scanner between the two measurements, which further contributed to misregistration of the two r maps. Ventilation maps for the ventral and dorsal slices in the pig lungs are shown for comparison in Figures 6.12 and 6.13 respectively.

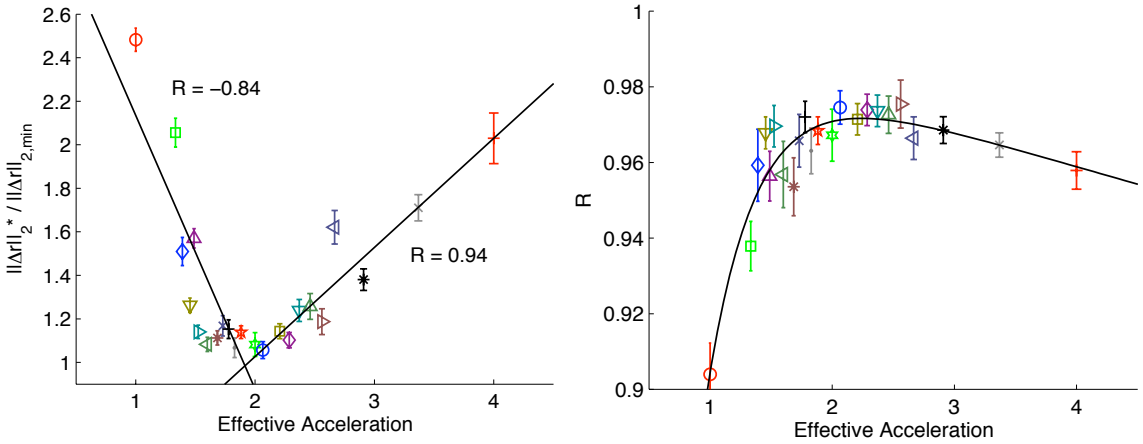

Figure 6.9. Variation of RMS error and correlation coefficient between the calculated and *a priori r* maps as a function of effective acceleration ratio. Each data point corresponds to the minimum error achieved with the corresponding optimal α.

The qualitative distribution pattern of r is identical between each pair of measurements across the five pigs. No statistically significant difference between the group statistics was observed: $r_{standard}$ = 0.27±0.09, 0.35±0.06, 0.40±0.04 versus $r_{accelerated}$ = 0.23±0.05, 0.34±0.03, 0.39±0.05 corresponding to ventral, middle and dorsal slices respectively (excluding conductive airways by masking $r > 0.9$ voxels). Slice-specific r measurements in some of the animals, even though well correlated, were statistically different between the two techniques, as indicated by p-values in Table 6.2. The largest difference was observed in pig #3 ($p < 10^{-4}$) showing a significantly larger r value measured by the standard technique. Gravitational dependence of ventilation (a positive ventral–dorsal gradient) distribution was universally present in all measurements.

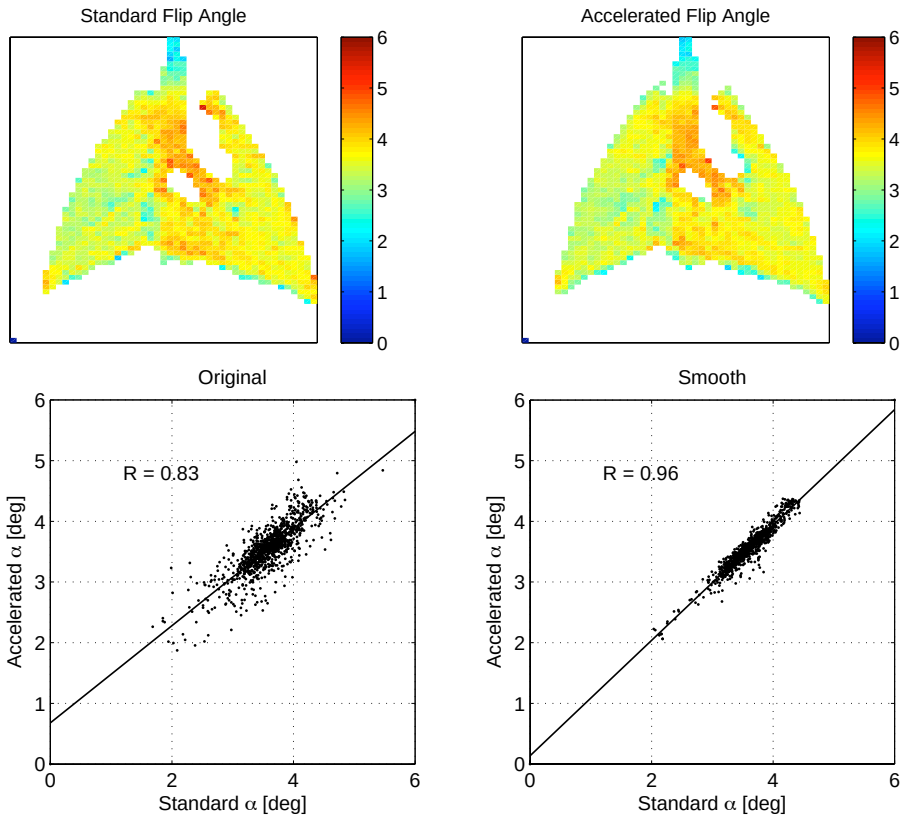

Figure 6.10. Comparison of internal flip angle measurements performed at the tail end of the serial ventilation sequence using the standard and accelerated acquisition schemes in a representative pig lung.

Multi-slice measurement of fractional ventilation was successfully implemented in five healthy pig lungs. Measurements were performed using both standard and accelerated methods for comparison, as shown in Figures 6.11–6.13. In order to retain fairness in comparison of results, acquisition parameters were kept almost entirely unchanged between the two measurements, except for the acceleration coefficient (2×) and the breath-hold length (1.0 versus 1.5 sec). As shown in Figure 6.10, the effective α was around 3.7 ± 0.3º throughout the lungs. This flip angle was selected rather conservatively prior to complete investigation of optimality conditions in presence of accelerated undersampling. It is therefore expected that the achievable SNR, and subsequently the

measurement accuracy, would benefit substantially by increasing the α value to the vicinity of ~5º and ~6º in the standard and accelerated acquisitions, respectively.

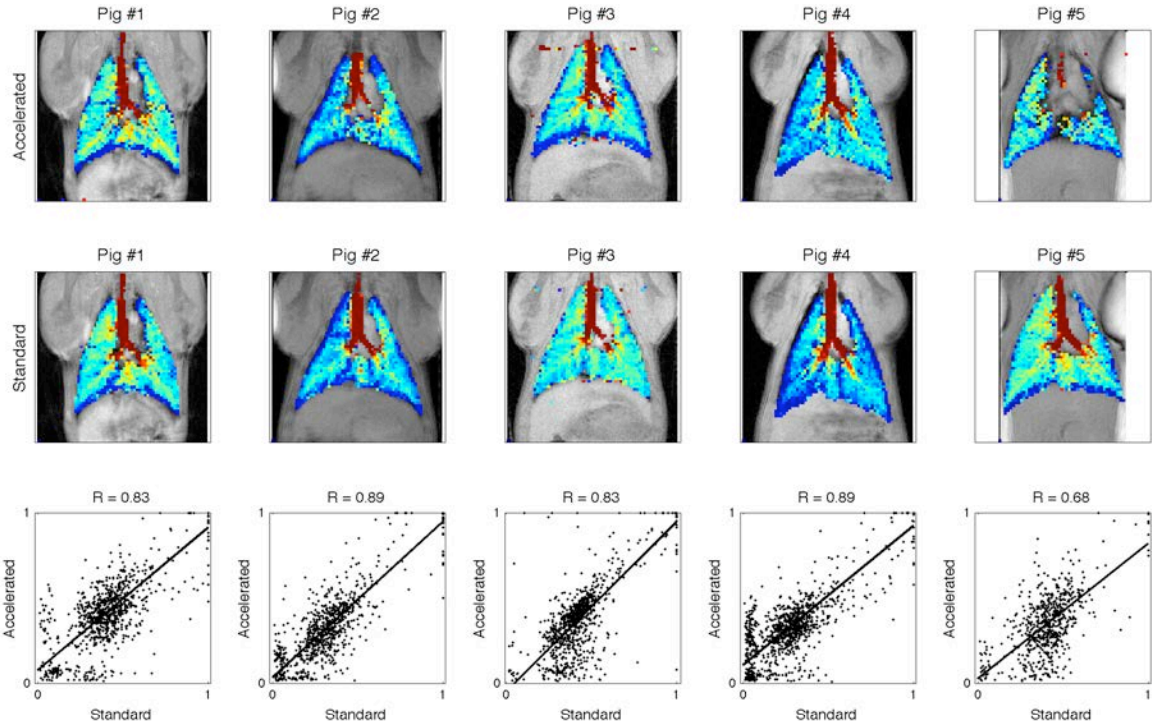

Figure 6.11. *Middle* slice fractional ventilation maps measured in lungs of five healthy Yorkshire pigs. Results are shown for both standard and accelerated measurement techniques along with the linear regression analysis.

It is difficult to interpret the correlation coefficient of standard and accelerated *r* measurements in the pigs. This is partly because the ground truth *in vivo* fractional ventilation values were not directly available in this study. The less than unity R values between the two measurements however point to the difference in derived *r* values throughout the lung. This difference is most likely and largely due to two primary factors: (*i*) different contribution of noise level in *r* estimation as a function of actual SNR value in the acquired images; and (*ii*) the difference in measurement uncertainty associated with the specific undersampling scheme in use. Given the simulation results in the synthetic

pig lung (Figure 6.9), it is expected that the accelerated measurements to more accurate under similar relative SNR conditions (e.g. in pig #1 and #4). However, the slice-specific differences in ventilation distribution appear to be largely concentrated near the diaphragm and edges of the lung, as shown in Figures 6.11–6.13. This is likely due to motion artifacts and tapering of SNR profile. Gravitational dependence of ventilation distribution from ventral to dorsal position was evident in all pigs, a phenomenon established by earlier HP gas MR studies in mechanically ventilation animals [39].

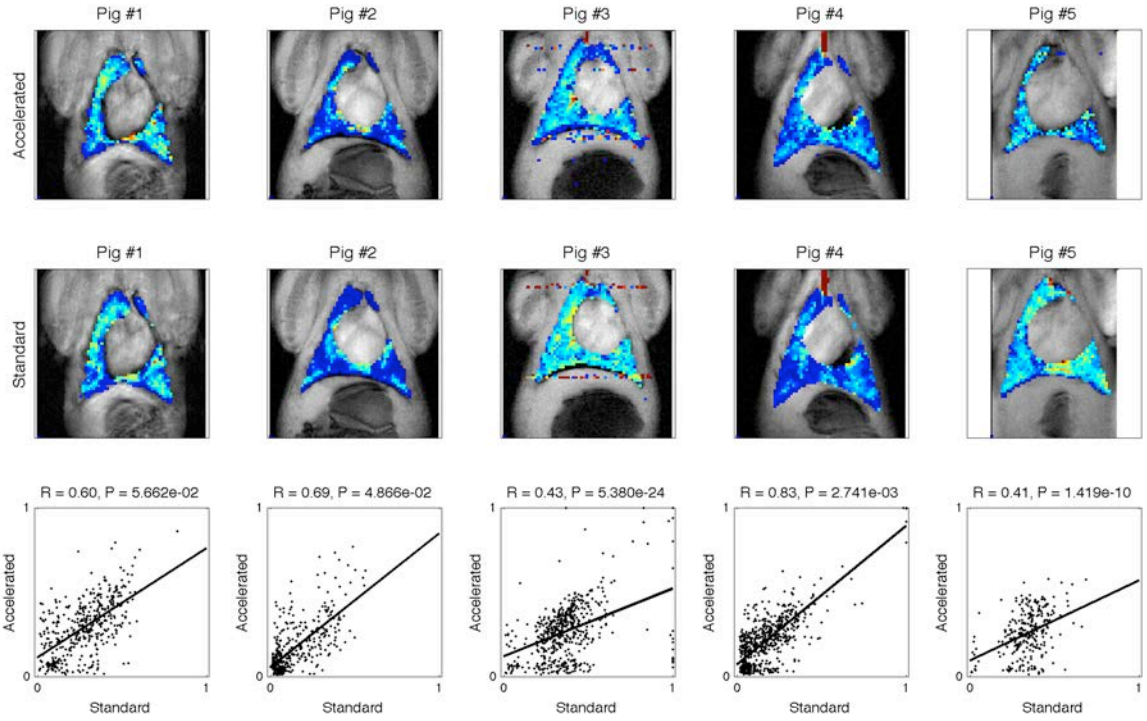

Figure 6.12. Fractional ventilation maps of the *ventral* slice in lungs of five healthy Yorkshire pigs. Results are shown for both standard and accelerated measurement techniques along with the linear regression analysis.

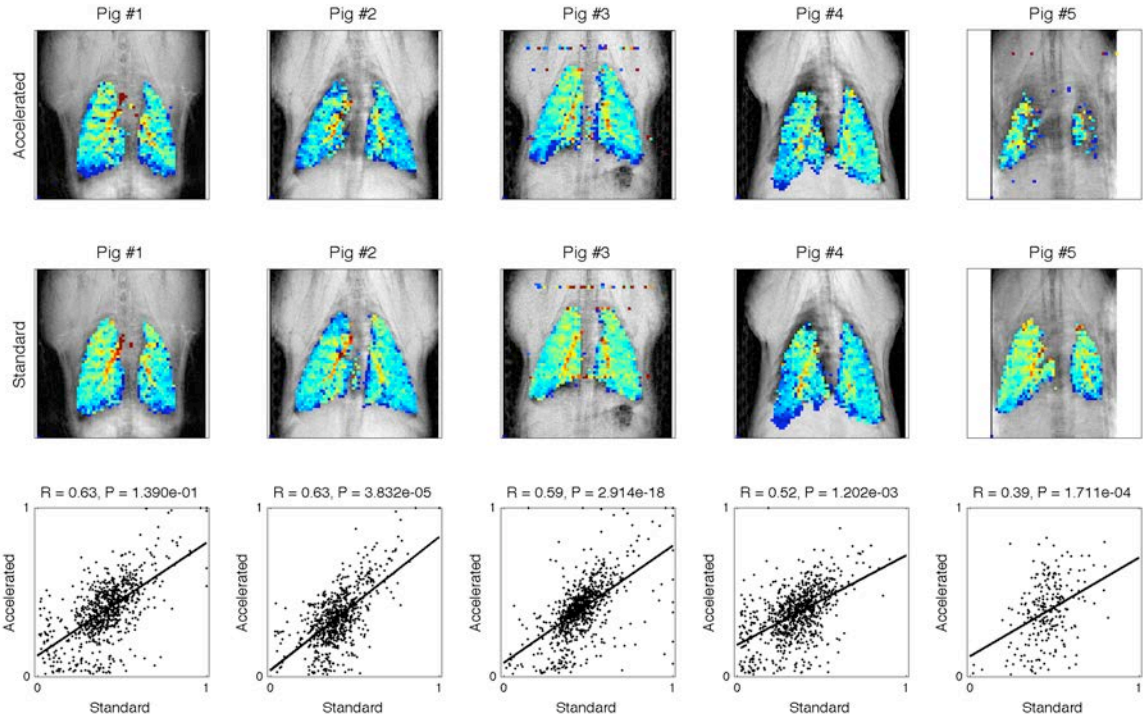

Figure 6.13. Fractional ventilation maps of the *dorsal* slice in lungs of five healthy Yorkshire pigs. Results are shown for both standard and accelerated measurement techniques along with the linear regression analysis.

Apart from the difference in signal dynamics and image reconstruction, the observed discrepancy between standard and accelerated r measurements also stems from the difference in breathing pattern, namely the breath-hold time. A longer acquisition time results in a longer breath-hold time, which, in turn, affects the mixing of inspiratory and residual gas compartments. This effect also results in capturing the images at a different time point in the respiratory cycle. Both effects can change the apparent fractional ventilation value measured from signal buildup in the airways and are linked to regional respiratory gas arrival and mixing time constants. Nevertheless, it is expected that the accelerated r measurements are more physiologically plausible due to their resemblance to normal breathing pattern as well as their reduced sensitivity to imperfect decoupling of ventilatory signal buildup from α estimates (Figure 6.7).

Table 6.2. (a) Ventilatory parameters used for image acquisition fractional ventilation and flip angle measurement studies in pigs, along with the p-value and correlation coefficient of r and α in the middle slices of each animal; **(b,c)** Mean and standard deviation of r measured in all three slices of the pig lungs along with the corresponding peak SNR values (all $r > 0.9$ values masked).

Table 6.2(a)

Pig No.	Weight [kg]	Respiratory Rate [breaths/min]	V_T [mL]	n_{ext}	n_{int}	P-value	R (r)	Original R(α)	Smooth R(α)
1	20.5	14	150	5	2	0.7887	0.83	0.32	0.68
2	25.0	16	200	10	5	0.7036	0.89	0.55	0.87
3	22.0	16	200	10	5	0.0001	0.83	0.70	0.90
4	23.0	16	200	20	5	0.0011	0.89	0.83	0.96
5	26.0	18	200	10	5	0.0000	0.68	0.26	0.62

Table 6.2(b)

Pig No.	r, Standard Acquisition			
	Peak SNR	Ventral Slice	Middle Slice	Dorsal Slice
1	45	0.27 ± 0.15	0.38 ± 0.16	0.40 ± 0.15
2	42	0.15 ± 0.13	0.29 ± 0.16	0.38 ± 0.14
3	54	0.35 ± 0.14	0.40 ± 0.12	0.45 ± 0.13
4	57	0.17 ± 0.13	0.26 ± 0.17	0.34 ± 0.15
5	47	0.32 ± 0.15	0.39 ± 0.18	0.43 ± 0.15
		0.27 ± 0.09	**0.35 ± 0.06**	**0.40 ± 0.04**

Table 6.2(c)

Pig No.	r, Accelerated Acquisition			
	Peak SNR	Ventral Slice	Middle Slice	Dorsal Slice
1	41	0.29 ± 0.16	0.38 ± 0.18	0.38 ± 0.16
2	25	0.17 ± 0.15	0.30 ± 0.17	0.35 ± 0.15
3	82	0.25 ± 0.16	0.35 ± 0.17	0.38 ± 0.16
4	45	0.21 ± 0.13	0.31 ± 0.15	0.37 ± 0.15
5	12	0.26 ± 0.13	0.34 ± 0.16	0.38 ± 0.18
		0.23 ± 0.05	**0.34 ± 0.03**	**0.39 ± 0.05**

6.8. Preliminary implementation in human subjects

In order to perform measurements of fractional ventilation in humans using the serial acquisition technique, a passive gas mixing and delivery device was prototyped for simultaneous administration of HP $^3He/N_2$ and O_2 gases to subjects (described in the Appendix). Measurements were made on one healthy human volunteer (30-year old male). All experiments were conducted under a protocol approved by the Institutional Review Board at the University of Pennsylvania, and with informed subject consent. The subject's vital signs (saturation of peripheral oxygen (SpO_2), heart rate, blood pressure and respiratory rate) were continuously monitored throughout the imaging session. Prior to performing the HP ^{3}He MRI study, a ^{1}H MRI scan was performed using an identical ventilation protocol with the HP gas mixture substituted by air.

Human imaging was performed using the same hardware and pulse sequence as the one used in the pig studies with the following differences: six ^{3}He coronal images (NS = 6) were acquired at a planar resolution of 6.25 × 6.25 mm^2 at FOV = 40 × 30 cm^2, ST = 20 mm, slice spacing = 4 mm, α = 3~4°, MS = 64 × 48 pixels, TR = 3.57 ms (for N_{PE} = 24), and TE = 3.3 ms. Only accelerated imaging was performed in the human subject using ACL = 16 and AR = 4, resulting in an effective acceleration factor of 2.

Ventilation images were also acquired in a similar fashion to those in pigs, using the multi-slice serial ventilation sequence (Figure 6.1) during an approximately 1.5-sec end-inspiratory breath-hold following each HP ^{3}He breath (N = 6), including a 500-msec pre-acquisition delay before each image acquisition. A sample consisting of approximately

4L of ^{3}He:N_2:O_2 ≈ 2:2:1 was prepared by mixing 1.6 L of ^{3}He, 1.5~1.7 mL of N_2 in one bag, and 800 mL of O_2 in a different bag and placed inside the bore of the magnet in the vicinity of the subject. Both bags were connected to the gas delivery system. Prior to inhalation of the HP gas mixture, the subject was instructed to breathe normally from room air through the gas delivery device over three breath cycles (I:E ~ 3:4) at a uniform rate of approximately 8–9 BPM. At this point the gas source was switched to the HP gas mixture and the subject was coached to inhale and exhale the mixture of HP ^{3}He, N_2, and O_2 at V_T = 600 mL which was monitored real-time with a computer-controlled MRI-compatible pneumotachometer prototyped as part of the gas delivery system.

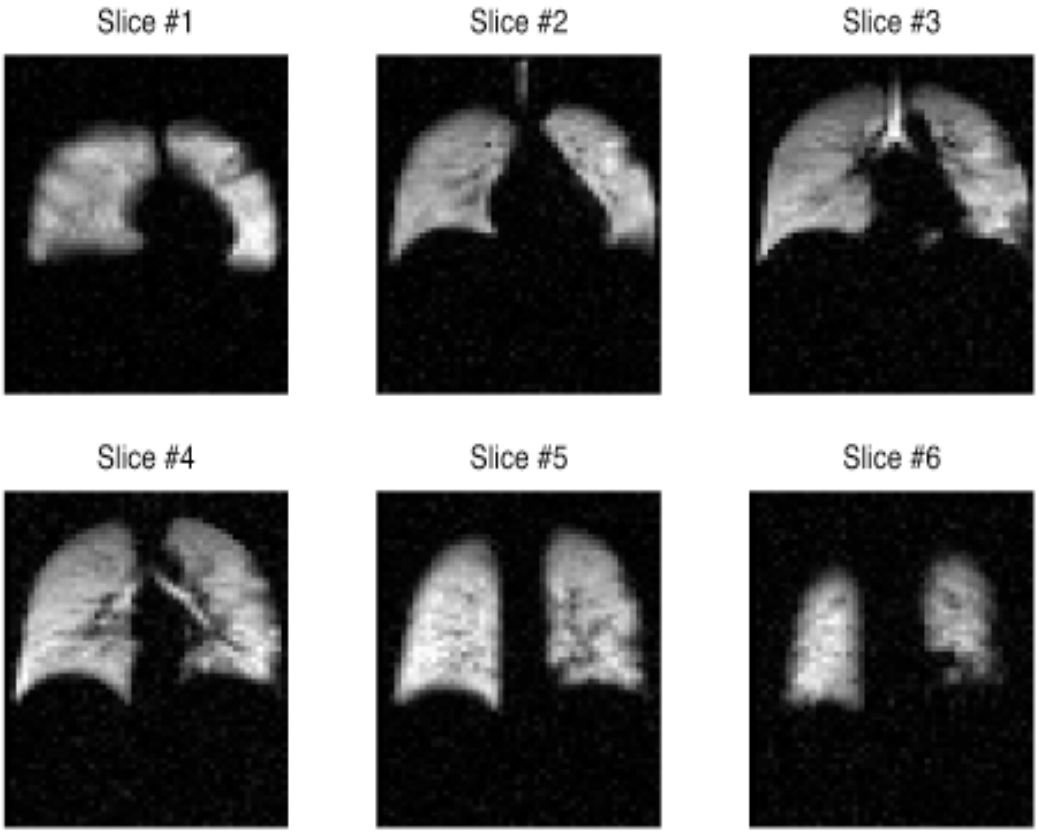

Figure 6.14. HP ^{3}He spin density images corresponding to the six coronal slices from the last breath of the serial fractional ventilation imaging sequence acquired in a healthy human subject.

Due to a synchronization problem between the subject and the coach, only 5 successful sequential images were acquired without the tail-end breath-hold, which was necessary to acquire the flip angle map. Therefore an average value of $\alpha = 3.5°$ was used for analysis over all the slices. The entire fractional ventilation measurement protocol required approximately 1.5 min to complete.

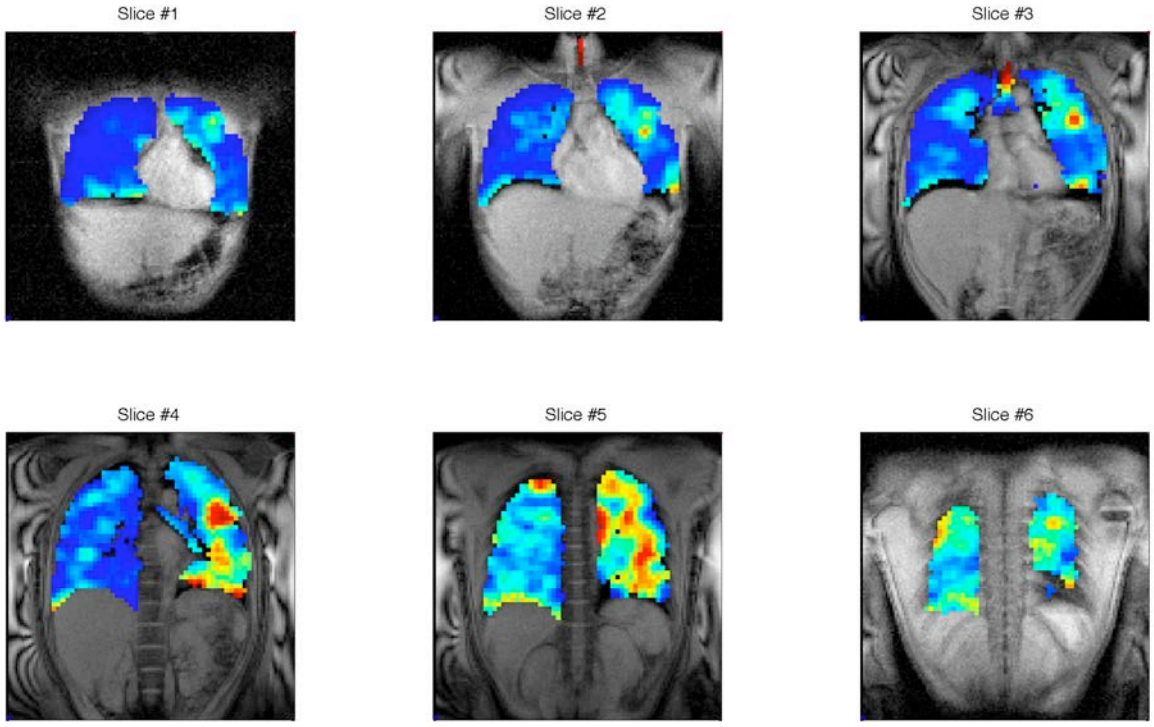

Figure 6.15. Coronal fractional ventilation maps in a healthy human subject acquired with the serial fractional ventilation imaging sequence, overlaid on the corresponding ^{1}H images of the thorax.

Representative spin density ^{3}He images acquired in the human subject are shown in Figure 6.14, corresponding to the last image (N = 5) in the fractional ventilation sequence. The peak SNR value in the shown images varied over 37–42 as a function of slice position. Images from the five breaths at each slice position matched fairly well (except for N = 6 which was excluded from the analysis), even though the imaging was performed under real-time coaching inside the scanner. The resulting maps of fractional

ventilation are shown in Figure 6.15. The overall gravitational dependency of ventilation is evident from the images. Certain areas of highly elevated *r* value can be seen especially in the upper left region. The reason for this observation is not immediately clear from the available measurements. A likely explanation could be related to using a fixed α value throughout the entire lung. As was discussed in Chapter 3, misassumption in α value leads to systematic errors in *r* estimation. Further experiments in healthy human subjects would be necessary to confirm these preliminary findings through simultaneous measurement of both α and *r* parameters (similar to pig studies) to assess the repeatability of measurements and to establish a robust ventilation imaging protocol before moving on to evaluate the method in subjects with pulmonary disease.

CHAPTER 7: Conclusion and Future Work

The presented results of whole lung fractional ventilation imaging in pigs and preliminary results in the human subject strongly support the feasibility and utility of the proposed serial fractional ventilation imaging technique in voluntarily breathing human subjects. This experimental setup served as a stepping-stone towards optimizing the methodology for routine implementation and technique optimization in human subjects and eventually those at risk of obstructive lung diseases. This work also provided a platform to address the technical challenges associated with long breathing time scales and to optimize acquisition parameters in large species with very similar pulmonary physiology to human beings. A major unresolved factor in streamlined translation of this technique to humans is repeatable and accurate real-time mixing and delivery of HP gas and oxygen to voluntarily breathing subjects. This objective will most likely still require some level of supervision to assure timely acquisition of images during the short breath-holds in each respiratory cycle. However, providing a combination of audio-visual feedback to the subject can very likely improve the synchronization necessary to accomplish the task. The major advantage is that, so long as the amount of inhaled gas per breath is monitored either through real-time gas volume measurement (e.g. using a pneumotachometer in the current design) or by simple monitoring of peak inspiration pressure, the breathing pattern can be autonomously controlled by the subject himself, the assistant in the room, or even automatic detection of respiratory waveforms.

The primary factor determining the number of images acquirable in one session is the HP gas production capacity (2 L of ^{3}He per session in our facilities). This volume can be a limiting factor if measurements need to be repeated (either by design or due to a measurement failure). The available amount of HP gas is typically diluted with ultra-high-purity N_2 to achieve larger quantities of imaging gas, provided that the polarization level is adequate to meet the SNR requirements (Figure 4.7). Almost all HP ^{3}He-based MRI techniques are, in principal, translatable, or have been proven to be comparable, to HP ^{129}Xe as means of overcoming the limited supply of the former isotope. With the advent of high capacity and continuous ^{129}Xe hyperpolarizing technology [40, 41], the quantity of polarized gas available for use may no longer be a limiting factor in a single imaging session. The anesthetic properties of xenon, however, remain a challenge for implementation in humans. Human xenon inhalation is limited by anesthetic considerations to < 35% alveolar concentration [42]. Therefore, depending on the available polarization, the concentration of the inhaled gas and the number of breaths should be optimally selected to limit the alveolar concentration of this gas while still providing a reasonable measurement of accuracy. However, due to the relatively short time span of these studies, the period of the breath-holds and likelihood of substantial uptake are smaller than anesthetic applications [43].

Respiratory gas diffusion can potentially affect the measurement accuracy in different ways. As shown in Figure 6.10, the majority of voxels enclosed by the trachea and major bronchi exhibit an elevated α value compared to lung parenchyma. This observation is

most likely a function of the relatively higher (i.e. nearly free) diffusion coefficient of gas particles in these regions. The more rapid dephasing and subsequent diffusion-induced signal decay during the breath-hold can be erroneously interpreted as a higher α value. Inter-slice diffusion effects can also affect flip angle measurement accuracy during the tail end breath-hold. While a given slice is pulsed repeatedly for flip angle estimation, it is possible that spins from neighboring slices could diffuse into the slice of interest and contaminate the RF-induced signal attenuation. Even though the suggested inter-slice gap in the multi-slice 2D acquisition provides some protection against this mechanism, and imaging acceleration minimizes these effects both through shortening of the scan time and diminishing the effect of α, utilization of 3D acquisition schemes can largely address this problem from a more fundamental standpoint.

Bibliography

1. Simon, B.A., *Regional ventilation and lung mechanics using X-Ray CT.* Acad Radiol, 2005. **12**(11): p. 1414-22.
2. Hlastala, M.P., *Multiple inert gas elimination technique.* J. Appl. Physiol., 1984. **56**: p. 1-7.
3. Colegrove, F.D., L.D. Schearer, and G.K. Walters, *Polarization of 3He Gas by Optical Pumping.* Phys. Rev., 1963. **132**(6): p. 2561--2572.
4. Happer, W., *Optical Pumping.* Rev. Mod. Phys., 1972. **44**(2): p. 169-249.
5. Raftery, D., et al., *High-field NMR of adsorbed xenon polarized by laser pumping.* Phys Rev Lett, 1991. **66**(5): p. 584-587.
6. Albert, M.S., et al., *Biological magnetic resonance imaging using laser-polarized ^{129}Xe.* Nature, 1994. **370**: p. 199-201.
7. Saam, B., W. Happer, and H. Middleton, *Nuclear relaxation of ^{3}He in the presence of O_2.* Phys. Rev. A, 1995. **52**(1): p. 862-865.
8. Yablonskiy, D.A., et al., *Quantitative in vivo assessment of lung microstructure at the alveolar level with hyperpolarized ^{3}He diffusion MRI.* Proc. Natl. Acad. Sci. U. S. A., 2002. **99**: p. 3111-3116.
9. Swanson, S.D., et al., *Distribution and dynamics of laser-polarized (129)Xe magnetization in vivo.* Magn Reson Med, 1999. **42**(6): p. 1137-45.
10. Mugler, J.P., 3rd, et al., *Simultaneous magnetic resonance imaging of ventilation distribution and gas uptake in the human lung using hyperpolarized xenon-129.* Proc Natl Acad Sci U S A, 2010. **107**(50): p. 21707-12.

11. Bloch, F., W.W. Hansen, and M. Packard, *Nuclear Induction.* Physical Review, 1946. **69**(3-4): p. 127.

12. Jackson, J.A. and W.H. Langham, *Whole-body NMR spectrometer.* Rev Sci Instrum, 1968. **39**(4): p. 510-3.

13. Damadian, R., *Tumor detection by nuclear magnetic resonance.* Science, 1971. **171**(976): p. 1151-3.

14. Hahn, E.L., *Spin Echoes.* Phys. Rev., 1950. **80**(4): p. 580-594.

15. Carr, H.Y. and E.M. Purcell, *Effects of Diffusion on Free Precession in Nuclear Magnetic Resonance Experiments.* Phys. Rev., 1954. **94**: p. 630-638.

16. Lauterbur, P.C., *Image formation by induced local interactions. Examples employing nuclear magnetic resonance. 1973.* Clin Orthop Relat Res, 1989(244): p. 3-6.

17. Lauterbur, P.C., *Magnetic resonance zeugmatography.* Pure Appl Chem, 1974. **40**(1-2): p. 149-157.

18. Kumar, A., D. Welti, and R.R. Ernst, *NMR Fourier zeugmatography.* Journal of Magnetic Resonance (1969), 1975. **18**(1): p. 69-83.

19. Damadian, R., M. Goldsmith, and L. Minkoff, *NMR in cancer: XVI. FONAR image of the live human body.* Physiol Chem Phys, 1977. **9**(1): p. 97-100, 108.

20. Kastler, A., *Quelques suggestions concernant la production optique et la détection optique d'une inégalité de population des niveaux de quantification spatiale des atomes. Application a l'éxperience de Stern et Gerlach et a la résonance magnétique.* J. Physique Rad., 1950. **11**: p. 255-265.

21. Walker, T.G. and W. Happer, *Spin-Exchange Optical Pumping of Noble-Gas Nuclei.* Rev. Mod. Phys., 1997. **69**(2): p. 629-642.

22. Mugler, J.P., et al., *Nuclear Magnetic Resonance using Hyperpolarized Noble Gases.* J. Magn. Reson. Anal., 1998. **In press**.

23. Deninger, A.J., et al., *Quantitative measurement of regional lung ventilation using ^{3}He MRI.* Magn. Reson. Med., 2002. **48**(2): p. 223-232.

24. Månsson, S., *Hyperpolarized Nuclei for NMR Imaging and Spectroscopy*, in *Department of Experimental Research & Department of Electrical Measurements*. 2002, Malmö University Hospital & Lund Institute of Technology: Malmo, Sweden. p. 178.

25. Moller, H.E., et al., *Measurements of hyperpolarized gas properties in the lung. Part III: ^{3}He T_1.* Magn Reson Med, 2001. **45**(3): p. 421-430.

26. Valind, S.O., C.G. Rhodes, and B. Jonson, *Quantification of regional ventilation in humans using a short-lived radiotracer--theoretical evaluation of the steady-state model.* J Nucl Med, 1987. **28**(7): p. 1144-54.

27. Gama de Abreu, M., et al., *Performance of the partial CO2 rebreathing technique under different hemodynamic and ventilation/perfusion matching conditions.* Crit Care Med, 2003. **31**(2): p. 543-51.

28. Benallal, H., et al., *Modeling of end-tidal and arterial PCO2 gradient: comparison with experimental data.* Med Sci Sports Exerc, 2002. **34**(4): p. 622-9.

29. Gudbjartsson, H. and S. Patz, *The Rician distribution of noisy MRI data.* Magn. Reson. Med., 1995. **34**: p. 910-914.

30. Emami, K., et al., *Improved Technique for Measurement of Regional Fractional Ventilation by Hyperpolarized 3He MRI.* Magn Reson Med, 2010. **63**(1): p. 13.

31. Fischer, M.C., et al., *Single-acquisition sequence for the measurement of oxygen partial pressure by hyperpolarized gas MRI.* Magn. Reson. Med., 2004. **52**(4): p. 766-773.

32. Yu, J., et al., *Simultaneous measurement of pulmonary partial pressure oxygen and apparent diffusion coefficient by hyperpolarized 3He MRI.* Magn Reson Med, 2009. **In Press**.

33. Henkelman, R.M., *Measurement of signal intensities in the presence of noise in MR images.* Med. Phys., 1985. **12**(2): p. 232-233.

34. Bashir, A., et al., *Calibration of RF transmitter voltages for hyperpolarized gas MRI.* Magn Reson Med, 2009. **61**(1): p. 239-43.

35. Holmes, J.H., et al., *Imaging of lung ventilation and respiratory dynamics in a single ventilation cycle using hyperpolarized He-3 MRI.* J Magn Reson Imaging, 2007. **26**(3): p. 630-6.

36. Holmes, J.H., et al., *3D hyperpolarized He-3 MRI of ventilation using a multi-echo projection acquisition.* Magn Reson Med, 2008. **59**(5): p. 1062-71.

37. Griswold, M.A., et al., *Generalized autocalibrating partially parallel acquisitions (GRAPPA).* Magn Reson Med, 2002. **47**(6): p. 1202-10.

38. Wang, Z., J. Wang, and J.A. Detre, *Improved data reconstruction method for GRAPPA.* Magn Reson Med, 2005. **54**(3): p. 738-42.

39. Mansson, S., et al., *3He MRI-based assessment of posture-dependent regional ventilation gradients in rats.* J Appl Physiol, 2005. **98**(6): p. 2259-67.

40. Hersman, F.W., et al., *Large production system for hyperpolarized 129Xe for human lung imaging studies.* Acad Radiol, 2008. **15**(6): p. 683-92.

41. Driehuys, B., J. Pollaro, and G.P. Cofer, *In vivo MRI using real-time production of hyperpolarized 129Xe.* Magn Reson Med, 2008. **60**(1): p. 14-20.

42. Muradian, I., et al., *Human regional pulmonary gas exchange with xenon polarization transfer (XTC),* in *15th Annual Scientific Meeting of ISMRM*. 2007: Berlin. p. 454.

43. Abdeen, N., et al., *Measurement of xenon diffusing capacity in the rat lung by hyperpolarized 129Xe MRI and dynamic spectroscopy in a single breath-hold.* Magn Reson Med, 2006. **56**(2): p. 255-64.

APPENDIX: Mechanical Ventilator and Gas Delivery Devices

A high precision MRI-compatible programmable respiratory gas mixing and delivery device, referred to as the *mechanical ventilator*, was designed and prototyped in our laboratory and was utilized to perform all the described animal imaging studies described in this dissertation. This ventilator is capable of real-time mixing of up to three different types of gases (e.g. ^3He, O_2, N_2 and air) at different ratios, as shown schematically in Figure A.1.

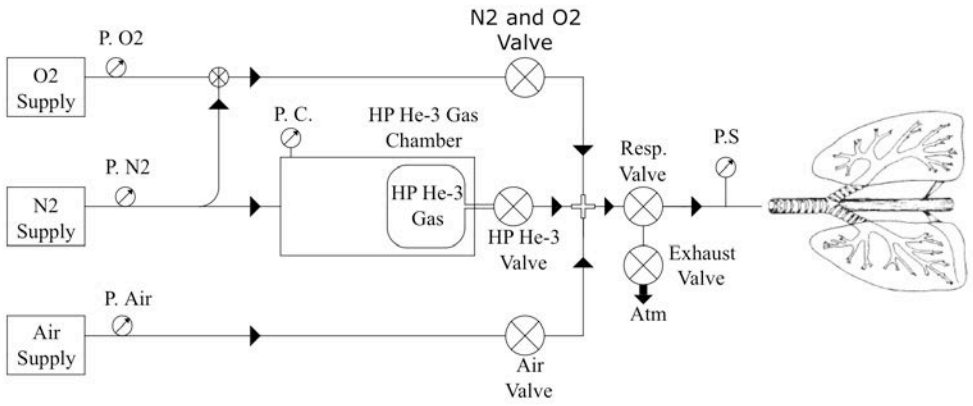

Figure A.1. Schematic diagram of the programmable gas mixing and delivery device, *mechanical ventilator*, used for HP gas MRI of intubated animals.

The ventilator gas-handling unit is composed entirely of pneumatic and nonmagnetic delivery valves, placed in the proximity of the RF imaging coil as close as possible to the animal inside the bore of the MRI scanner in order to minimize the dead spaces. A

different valve setup – suitable for the desired flow rate – is used for each range of species, as shown in Figures A.2 and A.3 for rats and pigs.

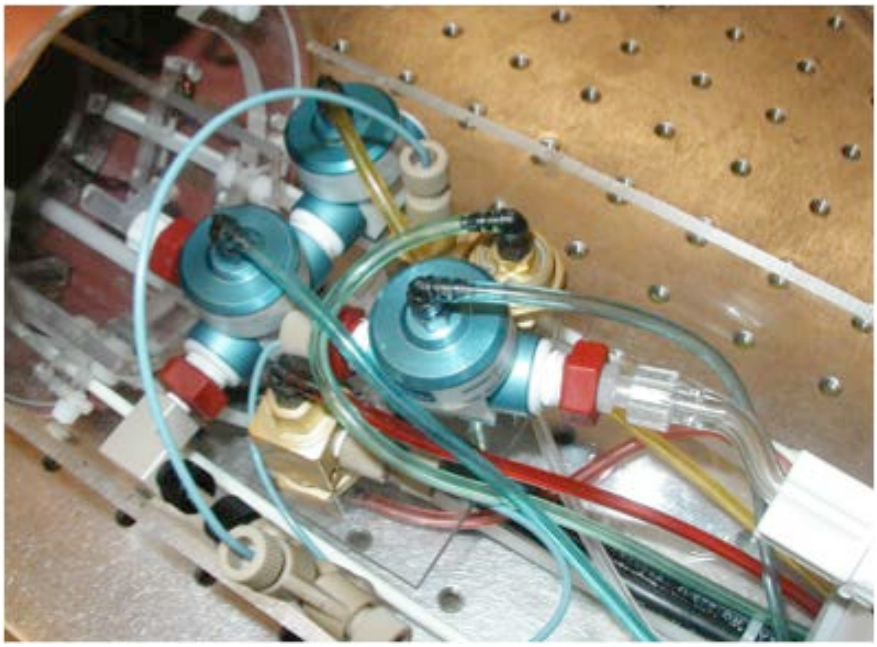

Figure A.2. Ventilator pneumatic valve setup for rats mounted in the proximity of the imaging RF coil inside the bore of the MRI scanner.

For the rat setup $V_D \approx 0.5$ mL (excluding the endotracheal tube), and $V_S \approx 3.5$ mL (between the ^{3}He chamber and the respirator valve). The same quantities for the pig valve setup are approximately 15 mL and 15 mL respectively. Placement of the HP ^{3}He chamber inside the magnet bore near the RF imaging coil results in prolonged polarization relaxation times (45~60 min), as shown in Figure A.4 for the rat setup.

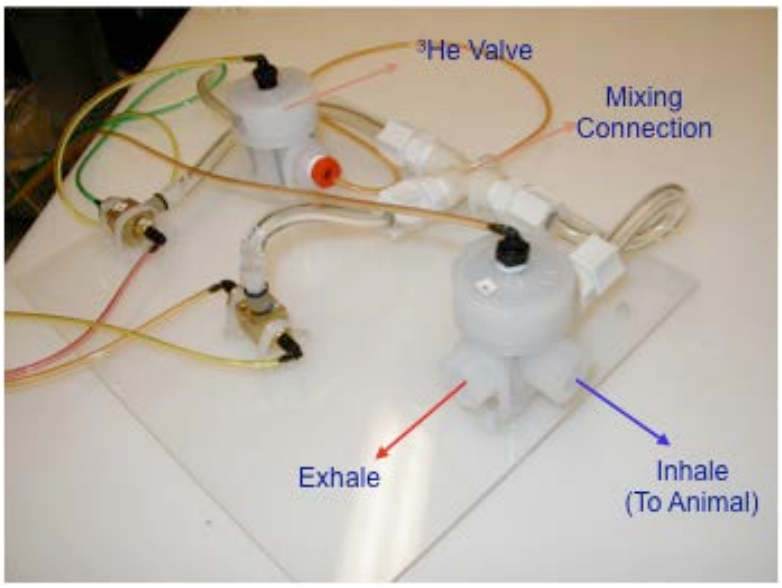

Figure A.3. Ventilator pneumatic valve setup for pigs mounted on a board placed in the proximity of the imaging RF coil inside the bore of the MRI scanner.

HP gas chambers were scaled up for use with pigs, as shown in Figure A.5. Due to their size it was not possible to place the large chambers inside the magnet bore, and were therefore placed on a stool near the MRI scanner.

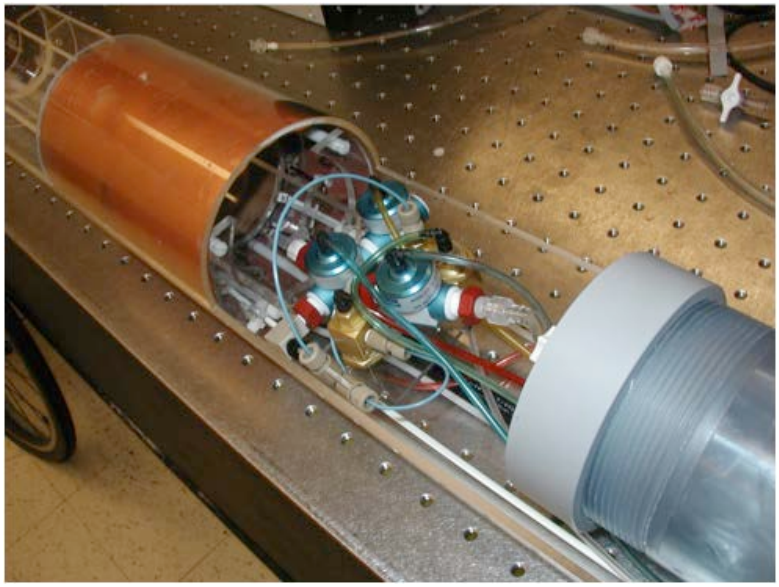

Figure A.4. Hyperpolarized gas chamber placed on the RF coil platform near the respiratory valves for the rat imaging setup. The entire assembly slides inside the magnet bore.

Figure A.5. Hyperpolarized gas chambers scaled up by a two orders of magnitude to accommodate the ventilatory volumes necessary for imaging pigs.

The rest of the ventilator components including the controller, computer interface and other pneumatic and electronic components were mounted in rack and placed away from the scanner magnetic field near the MRI operating console, as shown in Figure A.6.

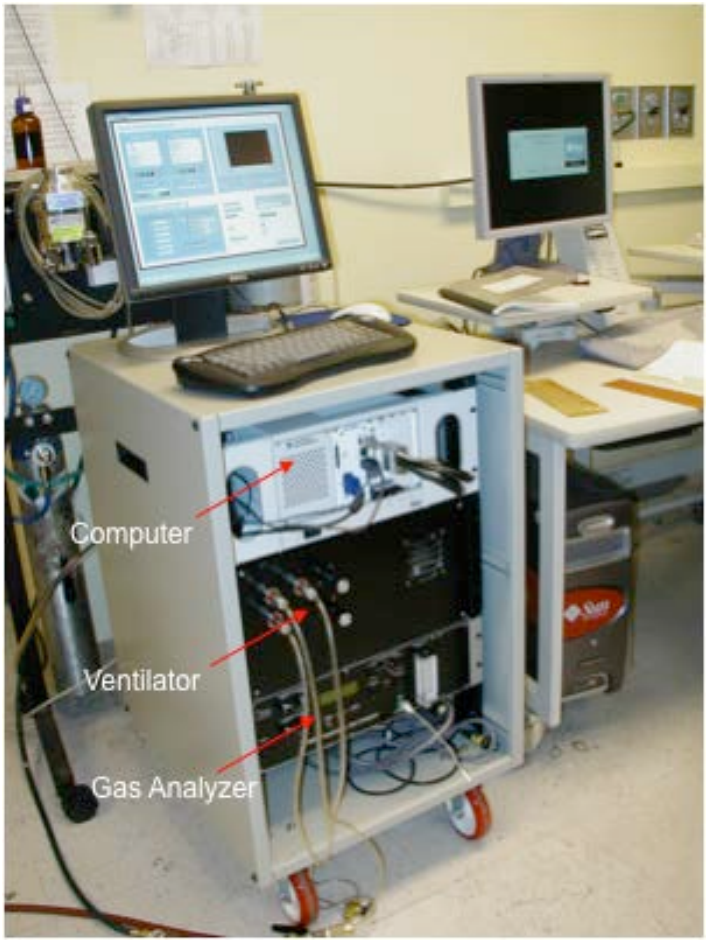

Figure A.6. Control unit, computer interface and other non-MRI-compatible components of the ventilator system placed away from the strong magnetic field, adjacent to the MRI operating console.

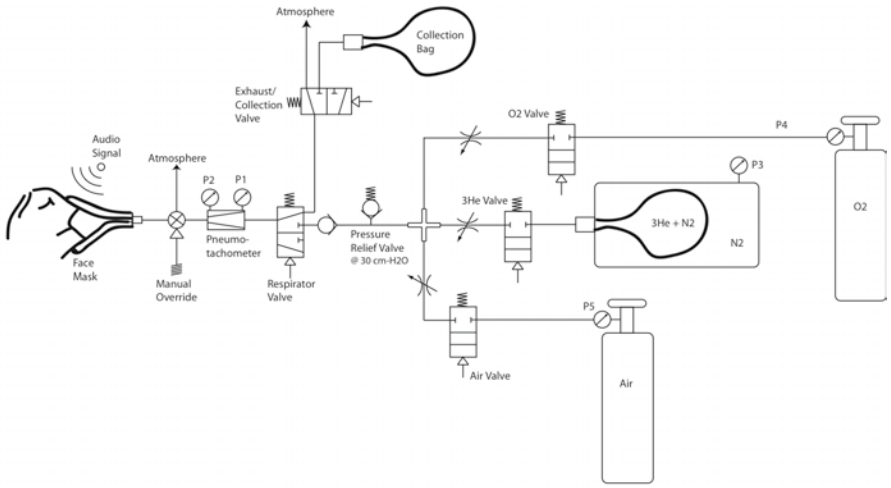

Figure A.7. Schematic diagram of the MRI-compatible passive gas mixing and delivery device for ventilation imaging in human subjects under voluntary breathing.

Based on the similar concept as the animal ventilator, a passive gas mixing and delivery device was prototyped for use in imaging human subjects, as shown schematically in Figure A.7. This design relies in real-time measurement of respiratory flow, which was made possible through a custom-made MRI-compatible pneumotachometer. The pneumotachometer is based on differential pressure measurement across a calibrated orifice and can deliver real-time flow rate of the inhaled mixture of ^{3}He and O2 gases, as shown in Figure A.8.

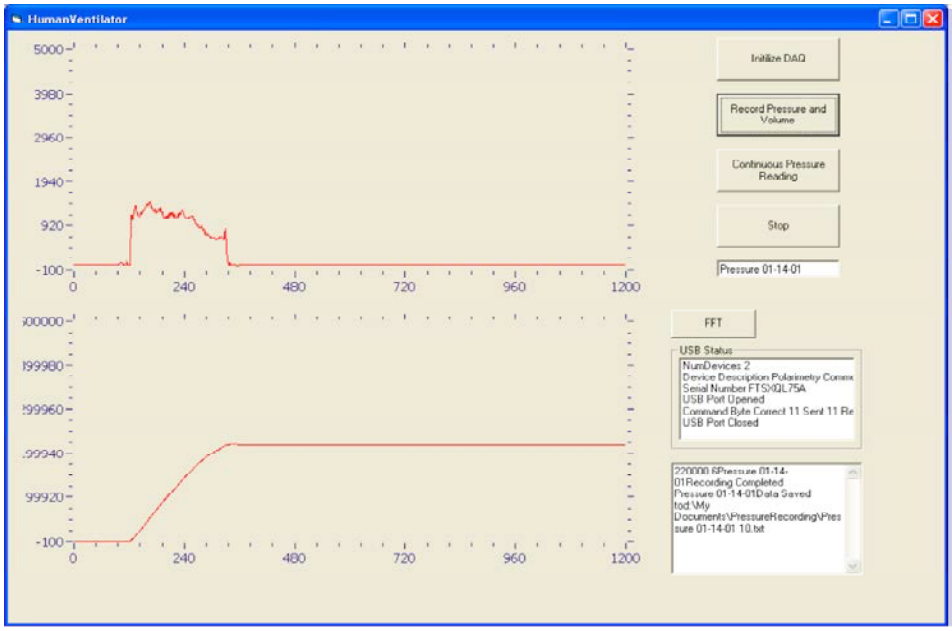

Figure A.8. Representative read-out of real-time inspiratory flow rate and volume acquired with the MRI-compatible pneumotachometer.

The device consists entirely of off-the-shelf plastic respiratory and pneumatic components and can be used to administer a mixture of hyperbolized gases to voluntarily breathing humans. The subject gets receive the queue for inhalation and exhalation and breath-hold times from a coach who is present in the MRI scanner room during the

imaging study. The coach uses the real-time flow read-out to guide the subject during the ventilation imaging trial.

Figure A.9. Prototype MRI-compatible passive gas mixing and delivery device for ventilation imaging in human subjects under voluntary breathing.